

1 **Relative roles of plume and coastal forcing on exchange**
2 **flow variability of a glacial fjord**

3 **Robert Sanchez¹, Fiammetta Straneo¹, Kenneth Hughes², Philip Barbour²,**
4 **Emily Shroyer^{2,3}**

5 ¹Scripps Institution of Oceanography, UC San Diego, San Diego, CA, USA

6 ²College of Earth, Ocean, and Atmospheric Sciences, Oregon State University, Corvallis, OR, USA

7 ³Office of Naval Research

8 **Key Points:**

- 9
- 10 • We present a set of realistically forced, multi-year numerical simulations of Ser-
11 milik Fjord in Greenland.
 - 12 • The shelf-driven circulation is tied to along-shelf wind stress and drives a rever-
13 sal in the exchange flow as winds intensify in September.
 - 14 • The plume-driven circulation is more effective at renewal with a flushing time 1/3
that of the shelf-driven circulation near the fjord head.

Abstract

Glacial fjord circulation determines the import of oceanic heat to the Greenland Ice Sheet and the export of ice sheet meltwater to the ocean. However, limited observations and the presence of both glacial and coastal forcing - such as coastal-trapped waves - make uncovering the physical mechanisms controlling fjord-shelf exchange difficult. Here we use multi-year, high-resolution, realistically forced numerical simulations of Sermilik Fjord in southeast Greenland to evaluate the exchange flow. We compare models, with and without a plume, to differentiate between the exchange flow driven by shelf variability and that driven by subglacial discharge. We use the Total Exchange Flow framework to quantify the exchange volume fluxes. We find that a decline in offshore wind stress from January through July drives a seasonal reversal in the exchange flow increasing the presence of warm Atlantic Water at depth, that the exchange flux in the summer doubles with the inclusion of glacial plumes, and that the plume-driven circulation is more effective at renewal with a flushing time $1/3$ that of the shelf-driven circulation near the fjord head.

Plain Language Summary

Glacial fjords connect the Greenland Ice Sheet and the ocean, and the circulation within fjords plays a crucial role in the exchange of heat and freshwater between the two. Glacial fjord circulation is driven, in part, by ice sheet surface melt which enters the fjord at the sea bed after falling through cracks in the ice. The meltwater's buoyancy causes it to rise as a plume, growing in volume through mixing with ocean water, before leaving the fjord closer to the surface. Fjord circulation is also influenced by the passing of storms close to the coast which can trigger pressure disturbances that propagate into the fjord as waves with periods of several days. We conducted two simulations of Sermilik Fjord in southeast Greenland to isolate and study the effects of coastal winds and plumes on fjord circulation. Our simulations reveal that as winds along the east coast of Greenland weaken, more warm water of subtropical origin can enter the fjord. We also find that in the summer the strength of the fjord circulation doubles in a model run with plumes versus a run without. These results increase our understanding of how fjord circulation responds to competing and time-varying external forcing.

1 Introduction

Glacial fjords connect the Greenland Ice Sheet (GrIS) with the continental shelf, and fjord dynamics are responsible for the import of oceanic heat to the GrIS and the export of ice sheet meltwater to the ocean. The fjord exchange of heat and salt at the fjord mouth, along with vertical mixing within the fjord, modifies water properties including ocean heat content and stratification, and ultimately sets the boundary conditions for ice-ocean interactions (Straneo & Cenedese, 2015; Holland et al., 2008; Straneo et al., 2011; Shroyer et al., 2017; Mortensen et al., 2018; Hager et al., 2022). Understanding fjord-shelf exchange is therefore crucial to predicting the impact of the ocean on marine-terminating glaciers and the consequences of exported freshwater on regional circulation and ecosystems (Hopwood et al., 2020; Straneo & Heimbach, 2013; Rysgaard et al., 2003).

Numerous drivers influence glacial fjord exchange on hourly to seasonal timescales. At the fjord mouth, circulation can be influenced by tides (Mortensen et al., 2011), external water mass variability (Schaffer et al., 2020), continental shelf wind variability (Jackson et al., 2014) and coastal-trapped waves (Gelderloos et al., 2021). Within the fjord, circulation is modified by mixing (Hager et al., 2022), internal waves (Inall et al., 2015), surface heat fluxes (Mortensen et al., 2011), local winds (Moffat, 2014), and iceberg melt (Davison et al., 2020). At the glacial boundary, or fjord head, additional forcing comes from surface runoff (Stuart-Lee et al., 2021), subglacial discharge (Carroll et al., 2015),

65 and submarine melting of the terminus (Zhao, Stewart, & McWilliams, 2022). However,
 66 untangling the individual role of these drivers is challenging because many of the effects
 67 are cumulative and difficult to isolate with limited observations (Straneo et al., 2019).
 68 In this study, we will focus on the relative roles of plume forcing and shelf forcing (e.g.,
 69 winds, coastal-trapped waves) on fjord circulation, as these are the two dominant forc-
 70 ing mechanisms of fjords in southeast Greenland (Jackson et al., 2014; Jackson & Stra-
 71 neo, 2016; Fraser & Inall, 2018; Gelderloos et al., 2022).

72 Glacial fjords undergo substantial seasonal variability in both shelf and glacial forc-
 73 ing that complicates diagnosing drivers of fjord circulation (Mortensen et al., 2014; Jack-
 74 son & Straneo, 2016; Hager et al., 2022). Glacial forcing from submarine melting and
 75 ice sheet meltwater runoff is strongest in summer, but shelf-forcing seasonality is depen-
 76 dent on factors such as sea ice, boundary currents and wind forcing which can vary re-
 77 gionally (Carroll et al., 2018; Gelderloos et al., 2017; Gladish, Holland, & Lee, 2014). Ob-
 78 servations are biased towards the summer and away from ice-congested areas, limiting
 79 comparisons between glacial-driven circulation and shelf-driven circulation. Consequently,
 80 we lack a deep understanding of the relative role of the shelf-driven circulation vs. plume-
 81 driven circulation in setting fjord properties seasonally and how these circulation modes
 82 vary along fjord.

83 Models of glacial fjords have been a useful tool in isolating different forcing mech-
 84 anisms and overcoming data limitations. Very high-resolution (< 10 m) models have brought
 85 insight into the dynamics of subglacial discharge plumes (e.g., Xu et al., 2012; Sciascia
 86 et al., 2013; Kimura et al., 2014; Carroll et al., 2015; Ezhova et al., 2017) and led to plume
 87 representation into larger fjord models (T. Cowton et al., 2015; Jenkins, 2011). Fjord-
 88 scale models have allowed for an assessment of the impact of along-fjord winds, along-
 89 shelf winds and shelf forcing on fjord dynamics (Sundfjord et al., 2017; Jackson et al.,
 90 2018; Fraser & Inall, 2018), of iceberg melt on water mass transformation (Davison et
 91 al., 2020; Kajanto et al., 2023), of sea ice retreat on fjord circulation (Shroyer et al., 2017),
 92 and of fjord geometry, including ice mélange, on fjord renewal (Gladish, Holland, Rosing-
 93 Asvid, et al., 2014; Carroll et al., 2017; Zhao et al., 2021; Hughes, 2022). While these
 94 models have significantly improved our understanding of glacial fjord processes, they are
 95 usually run on idealized bathymetry or with idealized forcing limiting any comparison
 96 with observations. Realistic models, evaluated against observations, are needed to iden-
 97 tify the time-integrated response of fjords to seasonally-varying forcing and to generate
 98 the complex circulation patterns seen in observations.

99 We use a high-resolution, realistic model of Sermilik Fjord, in southeast Greenland,
 100 forced by a wind-reanalysis product and boundary conditions from a larger pan-Arctic
 101 state estimate, to differentiate between the shelf-driven and subglacial discharge-driven
 102 exchange flow. Comparison with observations shows that the model reproduces the rel-
 103 evant dynamics over multiple years and through seasonal transitions. We split the re-
 104 sults into three sections focused on the seasonality of the shelf-driven circulation (Sec-
 105 tion 4), the plume-driven circulation (Section 5) and a comparison between the two in
 106 the context of the exchange flow (Section 6). We find the seasonality of the along-shelf
 107 winds drives reversals in the circulation, the exchange flow is primarily plume-driven dur-
 108 ing the summer, and the plume-driven circulation is more effective at renewal than the
 109 shelf-driven circulation. Understanding the response of fjord-shelf exchange to simulta-
 110 neous external and internal forcing is a critical step towards improved representation of
 111 ice-ocean interactions in climate models.

112 2 Background on Sermilik Fjord System

113 Sermilik Fjord (SF) is part of a large glacial fjord system in southeast Greenland
 114 (Fig. 1, inset map). The fjord varies in width from 5 – 10 km, is 550 – 900 m deep, and
 115 is about 80 km long before branching into three fjords connecting to Helheim, Fenris and

116 Midgaard glacier from west to east (Fig. 1). Midgaard Glacier has experienced the great-
 117 est cumulative loss of the three glaciers over the past 40 years (138 ± 5 Gt, Mouginot
 118 et al., 2019). However, Helheim Glacier is currently one of the largest outlet glaciers in
 119 Greenland (35 Gt/yr, Mankoff et al., 2020; Enderlin et al., 2014) and saw a rapid accel-
 120 eration and thinning in the 2000s (Howat et al., 2005; Luckman et al., 2006). Increased
 121 submarine melting due to relatively warm water at depth and circulation enhanced by
 122 ice sheet runoff has been proposed as a likely trigger for retreat (Straneo et al., 2011; Hol-
 123 land et al., 2008; Wood et al., 2018, 2021; Khazendar et al., 2019; Slater & Straneo, 2022;
 124 Jackson et al., 2022).

125 The water masses present in the fjord determine the heat available for melting. SF
 126 has a deep sill (500 m) that is far from the mouth allowing significant water column ex-
 127 change with the shelf (Straneo et al., 2010; Jackson et al., 2014). As a result, the wa-
 128 ter masses in the fjord broadly match those found on the adjacent shelf and are steered
 129 into SF through Sermilik Trough, a deep trough that cuts across the eastern part of shelf
 130 before running parallel to the coastline (Fig 1; Straneo et al., 2011; Harden et al., 2014;
 131 Snow et al., 2021). During the winter, SF is dominated by two water masses: cold and
 132 fresh Polar Water (PW) of Arctic origin and a deep, relatively warm and salty water of
 133 Atlantic origin (AW) (Sup. Fig. 1). During the summer, a third water mass, Warm Po-
 134 lar Water (WPW), is formed on the shelf from surface warming of PW and intrudes into
 135 fjords. Mixing across the shelf and trough determine the relative volumes of these wa-
 136 ter masses within the fjord (Snow et al., 2021; Harden et al., 2014).

137 In addition to shelf water masses, two types of meltwater are released into the fjord
 138 and affect fjord circulation and water properties. Submarine meltwater forms locally when
 139 icebergs and glaciers melt in the ocean, and subglacial discharge forms through surface
 140 melting of the ice sheet and enters the fjord at depth. Subglacial discharge generates a
 141 turbulent buoyant plume which drives an overturning circulation, upwells warm and salty
 142 AW into shallower depths and enhances submarine melting (Carroll et al., 2015; Beard
 143 et al., 2018; Jackson et al., 2022; Slater et al., 2022; Slater & Straneo, 2022). The up-
 144 welled AW is many times the volume of the original subglacial discharge flux and can
 145 displace PW that was previously near the head of the fjord (Mankoff et al., 2016; Beard
 146 et al., 2018). Therefore, both glacial and shelf processes influence the amount of AW (and
 147 heat) within the fjord.

148 Observations have shown that the circulation in SF is strongly influenced by shelf
 149 forcing (Straneo et al., 2010; Jackson et al., 2014; Snow et al., 2021). Shelf winds pri-
 150 marily flow southwestward and parallel to the coast resulting in downwelling conditions
 151 that generate large pycnocline displacements. These displacements create a density gra-
 152 dient within the fjord initiating baroclinic circulation with shallow inflow and deep out-
 153 flow (Klinck et al., 1981; Aure et al., 1996; Jackson et al., 2014). As the pycnocline re-
 154 laxes, the circulation reverses. Many of these events are correlated with observable pulses
 155 within Sermilik Fjord and are associated with 3–7 day periods, 40 cm/s speed and large
 156 heat and salt fluxes (Straneo et al., 2010; Jackson et al., 2014). The fjord heat content
 157 is dominated by pycnocline fluctuations which change the relative abundance of AW and
 158 PW and can obscure the influence of glacial forcing (Jackson & Straneo, 2016; Sanchez
 159 et al., 2021). These fluctuations have been linked with coastal-trapped waves (Fraser &
 160 Inall, 2018; Jackson et al., 2018).

161 As described above, subglacial discharge can initiate plumes at the heads of glacial
 162 fjords. Plumes drive an overturning circulation which enhances background melting (Slater
 163 et al., 2018; Jackson et al., 2020; Zhao, Stewart, & McWilliams, 2022; Zhao, Stewart,
 164 McWilliams, Fenty, & Rignot, 2022). The outflowing plume volume flux is primarily com-
 165 posed of ambient water entrained within the plume as it rises (Mankoff et al., 2016), and
 166 the plume is a significant source of water mass transformation. The outflowing plumes
 167 can interact with nearby bathymetry and drive recirculation in the fjord (Slater et al.,
 168 2018; Zhao, Stewart, & McWilliams, 2022). Thus, the influence of the plume-driven cir-

169 culation on fjord-shelf exchange is a function of both subglacial discharge flux and fjord
170 geometry.

171 Previous simulations of Sermilik Fjord (or idealized versions) have focused on coastal-
172 trapped waves (Jackson et al., 2018; Gelderloos et al., 2022), subglacial discharge plumes
173 (Sciascia et al., 2013), the impact of icebergs (Davison et al., 2020) and standing eddies
174 (Zhao, Stewart, McWilliams, Fenty, & Rignot, 2022). However none of these studies in-
175 volved the use of a full 3-dimensional model with realistic bathymetry and time-varying
176 realistic forcing. Most of the previous models were run to steady-state and examined the
177 fjord response to the input of glacial meltwater. Therefore, they could not capture sea-
178 sonal transitions and the time-integrated response of fjord properties to external forc-
179 ing.

180 **3 Model Setup and Forcing**

181 We ran nearly three-year simulations (2015 – 2017) of a regional model of Sermi-
182 lik Fjord and its adjacent shelf (Fig. 1) using the hydrostatic-configuration of the MIT-
183 gcm (Marshall et al., 1997; Adcroft et al., 2004). The model domain is 360 by 640 cells
184 with an isotropic horizontal resolution of 280 m by 280 m. The model was configured
185 with 32 vertical levels varying from 10-m resolution in the upper 200 m to 100-m res-
186 olution at 950 m depth. Model bathymetry is based on BedMachine v3 (Morlighem et
187 al., 2017). The maximum depth within SF was 920 m (Fig. 1). Advection of temper-
188 ature and salinity uses a third-order flux limiter scheme. The standard time step for the
189 model was 60 s but reduced occasionally for model stability. Output snapshots are saved
190 every three hours.

191 The model was configured with a nonlinear equation of state following Jackett and
192 McDougall (1995). Mixing is parameterized using the KPP vertical mixing scheme (Large
193 et al., 1994) with a background viscosity of $10^{-4} \text{ m}^2 \text{ s}^{-1}$ and diffusivity for temperature
194 and salinity of $10^{-5} \text{ m}^2 \text{ s}^{-1}$ in the vertical. In the horizontal, the set-up used a non-dimensional
195 harmonic viscosity of 0.01, which equates to approximately $3 \text{ m}^2 \text{ s}^{-1}$ for the isotropic
196 configuration, modified by a non-dimensional Smagorinsky scheme with coefficient 3 fol-
197 lowing Griffies and Hallberg (2000). A quadratic drag with coefficient 2×10^{-3} was ap-
198 plied at the bottom.

199 Simulation initialization and boundary forcing is taken from the Arctic Subpolar
200 Gyre State Estimate “ASTE” (Nguyen et al., 2021). Initial temperature, salinity and
201 velocity fields were generated from a spin-up simulation of three months in which the
202 boundary forcing was held steady and no surface forcing was applied. On each of the three
203 boundaries on the shelf, there are sponge regions that are 20 grid cells wide in which T ,
204 S , U , and V are relaxed to the ASTE values with time scales of 3 hours on the outer edges
205 and 30 hours on the inner edges. Boundary fields are updated daily and linearly inter-
206 polated onto each model time step. A constant offset in temperature (-1.5°C) and salin-
207 ity (-0.3) was applied to the ASTE fields to tune to available mooring and profile records
208 near the mouth of Sermilik fjord (Fig. 2).

209 Model surface forcing was taken from ERA5 (Hersbach et al., 2020). Surface fluxes
210 were generated within MITgcm external forcing module using 10-m winds, humidity, air
211 temperature, and downward shortwave and longwave radiative fields. Surface forcing fields
212 were updated hourly with a linear interpolation to simulation time steps. While ERA5
213 realistically simulates shelf forcing, the fjord is largely unresolved. No sea ice was included
214 in the model.

215 For a brief description of the wind forcing, we plot the wind stress on the shelf at
216 the southern edge of the coastal transect (Fig. 1). The along-shelf wind stress (oriented
217 such that northeasterly wind is negative) is almost always downwelling favorable (Fig.
218 3). Individual wind events can be intense reaching magnitudes as high as 0.8 N/m^2 . A

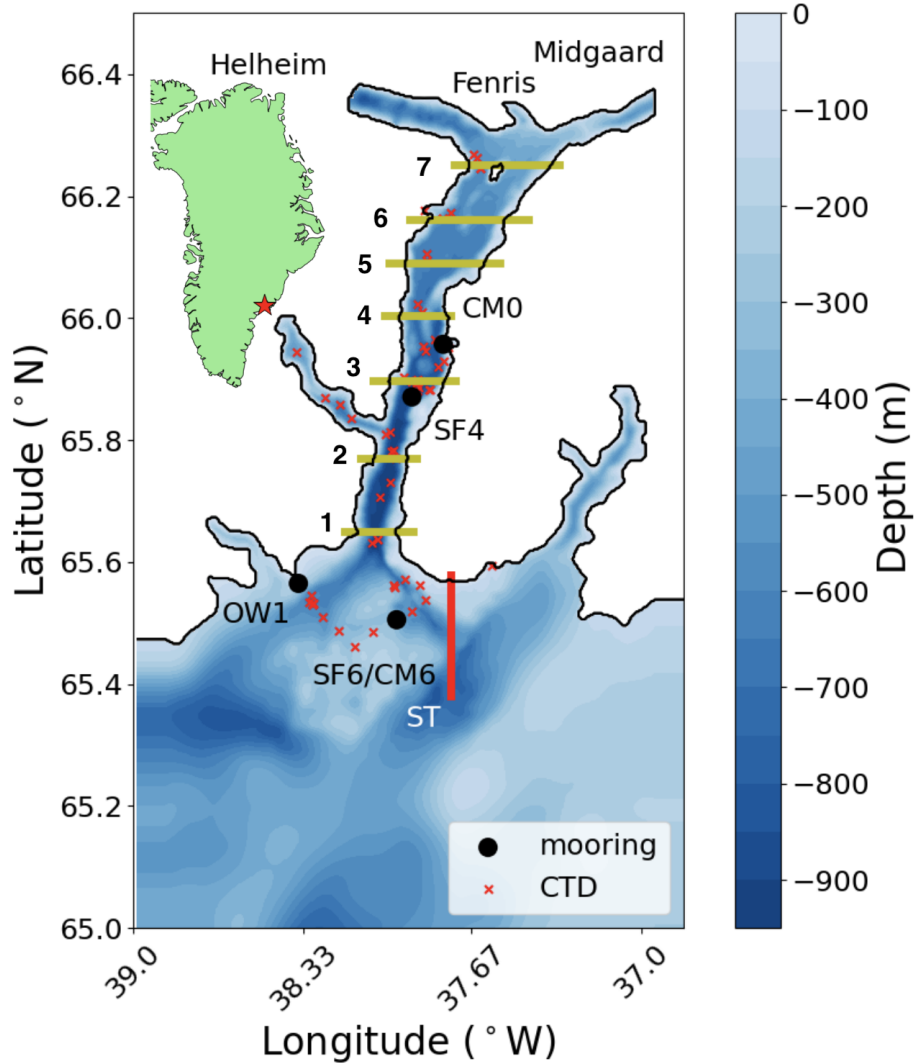


Figure 1. Model domain and bathymetry. In yellow are the gates used for the calculation of TEF fluxes in Sermilik Fjord. The red line is the coastal section used for the shelf seasonality analysis. The locations of observations used in the model comparison are given in black circles (moorings) and red crosses (CTD). The glacier names are given at the top. Sermilik Trough (ST) is shown in white text. The inset map shows the location of Sermilik Fjord in the context of Greenland.

low-pass wind stress representative of seasonal wind patterns, τ_p is calculated using a 90 day, 6th order Butterworth filter. τ_p shows the winds are strongest from November to May and weakest from June to August (Fig. 3a).

We compare two three-year simulations in this manuscript. The first is configured as described above without representation of the glacial runoff and melt. This run is referred to as the ‘No Glacier’ (NG) run. The second is referred to as the ‘With Glacier’ (WG) run. Within the WG run, subglacial discharge plumes and glaciers were added to the three glaciers at the north end of SF (those named in Fig. 1). This cold, fresh water originates as surface melt of the glacier, and peaks in summer. It makes its way through

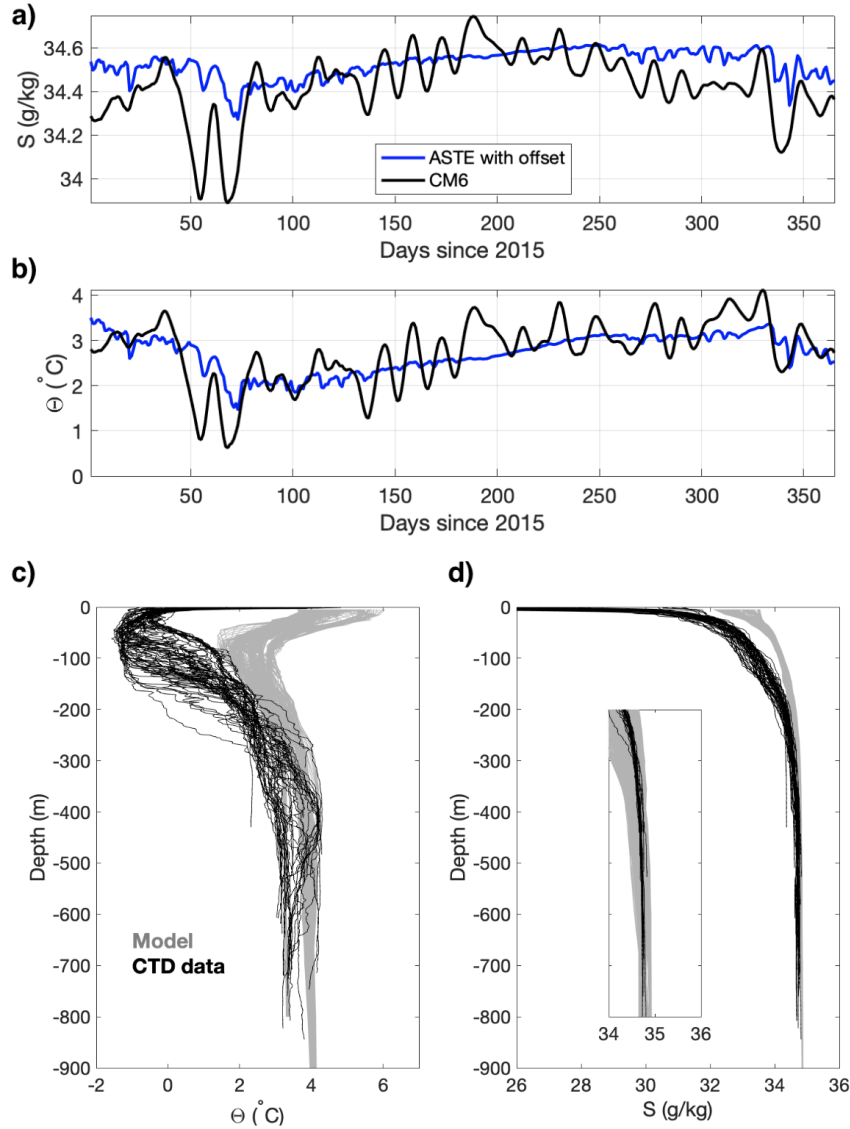


Figure 2. a-b) Comparison of ASTE boundary conditions with shelf mooring located at CM6 (Fig. 1).c-d) comparison of model output from Sermilik Fjord over the months of July and August 2015 against CTD profiles taken in August 2015. The inset in panel d is a zoom on the region between 34 and 36 g/kg. The y-axis is shared with the larger figure.

228 to the base of the ice sheet and enters the ocean at depth at the grounding line to be-
 229 come a buoyant, turbulent plume. Within the WG run, plume dynamics are parameter-
 230 ized following T. Cowton et al. (2015). Discharge values come from regional climate sim-
 231 ulations compiled by Slater et al. (2020). A constant discharge is used for each month.
 232 Subglacial discharge is applied to all months and varies interannually (Fig. 3). Peak dis-
 233 charge in the summer at each glacier is $300\text{--}600\text{ m}^3\text{ s}^{-1}$. Discharge in the winter is $2\text{--}5\text{ m}^3\text{ s}^{-1}$.
 234 Although this run includes a melting iceface, the input from the glacier is negligible and
 235 the main difference between NG and WG are the effects of the subglacial discharge plume.
 236 Therefore, we will refer to circulation initiated by glacial forcing as the “plume-driven”

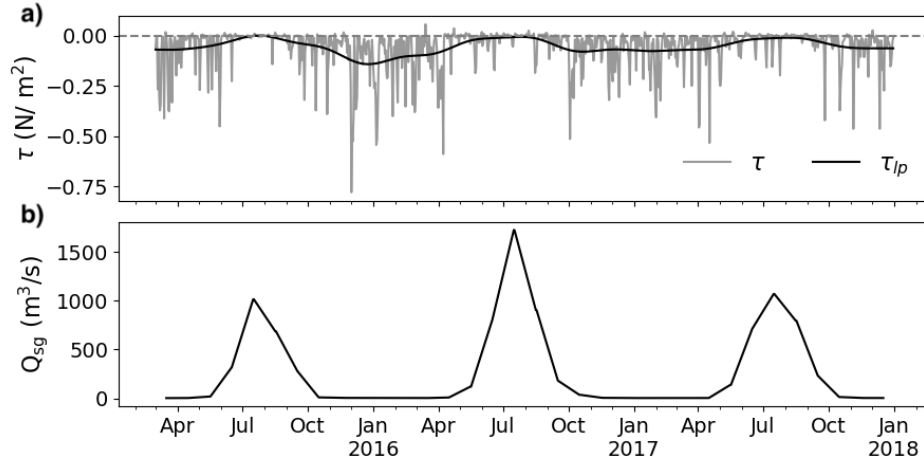


Figure 3. a) Along-shelf wind stress peaks in winter. The daily along-shelf wind stress is in gray and τ_p is in black. Negative is towards the southwest. b) The total subglacial discharge (Q_{sg}) flux in the WG run.

237 circulation. The NG and WG simulations were identical apart from the addition of glacial
238 plumes.

239 A full comparison of the model output against observational data is given in Ap-
240 pendix A, but is briefly described here. Both visually (Fig. 2 and Fig. A1) and quan-
241 titatively, the model does a reasonable job of recreating the temperature and salinity vari-
242 ability seen in the observations. The mooring data on the shelf is significantly correlated
243 ($r = 0.75$) in salinity and temperature ($r = 0.51$) over 30-day timescales. Additionally,
244 both the salinity and temperature were significantly correlated on higher-frequency timescales
245 (< 30 days) giving confidence that higher shelf-forcing is reasonably represented (Table
246 A1). The volume transport in the model does not deviate substantially from the esti-
247 mates of the transport from the observations, although it does underestimate the sum-
248 mer transport (Sup. Fig. 1). However, we recognize that the model cannot reproduce
249 the shallower properties such as PW salinity and stratification because it is missing fresh-
250 water sources such as icebergs, sea ice and surface runoff (Fig. 2). Other models (Davison
251 et al., 2020; Kajanto et al., 2023) and observations (Moon et al., 2018) suggest the fresh-
252 water flux from icebergs can increase the strength of circulation and significantly mod-
253 ify (cool and freshen) shallow fjord properties increasing stratification. Recently, Kajanto
254 et al. (2023) showed, for a similar large fjord in west Greenland, that without icebergs
255 the model could not reproduce the observed properties. Therefore, our results are focused
256 on shelf-forcing and plume transport, both of which appear reasonably well represented,
257 and we leave iceberg forcing to be implemented in a future study.

258 4 Total Exchange Flow Method

259 The transport of heat, salt, nutrients and other tracers out of the fjord is set by
260 the exchange flow. In traditional estuaries, the exchange flow describes the sub-tidal mean
261 circulation, typically with inflowing salty water at depth and outflowing fresher water
262 near the surface (MacCready & Geyer, 2010). A key characteristic of the classic exchange
263 flow is that the circulation, set up by river input and mixing, drives a volume flux out
264 of the estuary many times greater than the initial freshwater volume flux. Applying the
265 exchange flow concept to deep glacial fjords, we let wind-driven variability (1–10 days)
266 play the role of tides (high-frequency oceanic variability) and glacial freshwater to play

the role of river input (buoyancy) in setting up a low-frequency exchange flow (Jackson & Straneo, 2016). Using the exchange flow framework, we can analyze the role of shelf and glacial forcing in setting fjord properties.

We use the Total Exchange Flow (TEF) method (MacCready, 2011; MacCready et al., 2018; Burchard et al., 2018; Lorenz et al., 2019) to evaluate bulk properties of the model exchange flow, such as incoming/outgoing volume flux $Q_{\text{in}}, Q_{\text{out}}$, incoming/outgoing Salinity $S_{\text{in}}, S_{\text{out}}$, and incoming/outgoing Temperature $\Theta_{\text{in}}, \Theta_{\text{out}}$. TEF allows a calculation of exchange flow properties consistent with the Knudsen relation in salinity space (Burchard et al., 2018). Typically, TEF averages are calculated in salinity coordinates rather than spatial coordinates allowing both tidal and sub-tidal fluxes to contribute to the exchange flow. For SF, temperature gradients are non-negligible to the overall pressure gradient and partially compensate salinity, therefore, we use density coordinates rather than salinity coordinates to evaluate the changes in volume (mass) transport (Lorenz et al., 2020). While density coordinates are used for volume transport, when considering salt or heat budgets, salinity and temperature coordinates are necessary (Lorenz et al., 2020). Therefore for salt and heat fluxes, we use salinity and temperature coordinates respectively.

The TEF transport (Q_i^b) of a tracer b in coordinates i is (Lorenz et al., 2020)

$$Q_i^b = \left\langle \int_{A(i)} bu dA \right\rangle, \quad (1)$$

where $A(i)$ is the area of a cross section with coordinates greater than i , u is the velocity normal to the cross section defined to be positive inwards, and $\langle \rangle$ denotes temporal averaging. For example if $b = 1$, and $i = \sigma$, then Eq. 1 calculates the net volume transport with $Q_\sigma(0) = -Q_{\text{BT}}$, the total barotropic flux, and $Q_\sigma(\sigma_{\text{max}}) = 0$. We sort the data into 1000 discrete bins and use a 30-day rolling mean in place of a Godin (tidal) filter, to average over the wind variability (Jackson & Straneo, 2016). The derivative of Eq. 1 gives a tracer flux

$$q_i^b(i) = -\frac{\partial Q_i^b(i)}{\partial i}, \quad (2)$$

as a function of coordinate choice. To get the total incoming (outgoing) tracer flux we then integrate Eq. 2 over the portions that are inflowing (outflowing). We use the dividing salinities method (Lorenz et al., 2019) which identifies the extremum in Q_i^b as the dividing coordinate class i_{div} to define inflowing and outflowing regions. The bulk tracer values are $b_{\text{in}} = Q_{\text{in}}^b/Q_{\text{in}}$ and $b_{\text{out}} = Q_{\text{out}}^b/Q_{\text{out}}$ where b can be salinity S , Potential Temperature Θ or Potential Density anomaly σ . Note that Q_{in} calculated in σ space is not the same as Q_{in} calculated in S or Θ space, and the appropriate volume flux choice depends on the tracer budget being considered. Additional details for calculating TEF from a numerical model are given in Lorenz et al. (2019). All TEF output is calculated here using the pyTEF library (Lorenz et al., 2020). We calculate TEF values on 7 transects along SF fjord (Fig. 1). For the time series of TEF transport, we show the transport at the 3rd line (SF Line 3).

5 Shelf-Forced Circulation

5.1 Contribution of CTWs to Shelf-driven Circulation

Both Fraser et al. (2018) and Jackson et al. (2018) have identified coastal-trapped waves (CTWs) as the primary mechanism through which the wind-driven forcing is communicated to southeast glacial fjords, and CTWs have been observed in other dynamically-wide Arctic Fjords (Inall et al., 2015). We evaluate the contribution of CTWs to the shelf-driven circulation by comparing the model output with an analytical model of CTWs. While the theory is described here alongside the background on CTWs, the analysis is carried out in Section 7.3. For our analysis, we use the Kelvin-wave model from Jackson

313 et al. (2018) who showed that Kelvin waves were a good representation of coastal-trapped
 314 waves in Greenland’s fjords due to their steep sides. The Kelvin-wave model uses a two-
 315 layer approximation with the volume flux in the top layer given by

$$Q_{\text{ctw}} = 2cR_d(1 - e^{-W/R_d}) \sin\left(\frac{\omega}{c}(L + W/2 - y)\right)\eta(t), \quad (3)$$

316 where η is the amplitude of the pycnocline fluctuation at the mouth, y is the distance
 317 from the mouth, ω is the forcing frequency, c is the baroclinic wave speed, L is the fjord
 318 length, W is the fjord width and R_d is the deformation radius $R_d = c/f$ where f is the
 319 Coriolis frequency. For our application, $c = \sqrt{g'h'}$ where g' is the reduced gravity be-
 320 tween the upper layer h_1 and the bottom layer h_2 , and $h' = h_1 * h_2 / (h_1 + h_2)$ is the
 321 effective height. The layer heights were calculated by solving for the depth of the zero
 322 crossing of the first horizontal normal mode at the fjord mouth (Hughes et al., 2018).
 323 On average, $c = 0.68$ m/s, but it varies between 0.5 and 0.9 m/s from winter to sum-
 324 mer respectively. This speed is lower than observations (Jackson et al., 2014, $c = 1.1$
 325 m/s). This difference is most likely attributable to weak model stratification compared
 326 to observations. We define pycnocline fluctuations as

$$\eta_M = \frac{\Delta\sigma}{\bar{\sigma}_z}, \quad (4)$$

327 where σ is the potential density anomaly at the mouth of the fjord and $\bar{\sigma}_z$ is a 30-day
 328 rolling mean of the section-averaged vertical density gradient at the mouth.

329 Since the fjord experiences broadband forcing rather than a single forcing period,
 330 we Fourier transform η to a function of frequency $\hat{\eta}(\omega)$ and use Eq. 3 to solve for $\hat{Q}_{\text{ctw}}(\omega)$,
 331 and then inverse Fourier transform to get $Q_{\text{ctw}}(t)$. However, a challenge arises because
 332 c is a function of t and is inside of the sine term which is a function of ω . Therefore, we
 333 instead calculate a 2D matrix of $\hat{Q}(c, \omega)_{\text{ctw}}$ using constant values of $c = [0.4, 0.5, \dots, 1.1]$
 334 m/s. We then inverse Fourier \hat{Q} and use a timeseries of $c(t)$ to interpolate across $Q(c, t)_{\text{ctw}}$
 335 and recover a 1D time series. The calculated CTW volume flux is about 66% the mag-
 336 nitude of the high-frequency (< 15 days) incoming volume flux (Sup. Fig. 9) suggest-
 337 ing the CTW theory is slightly underestimating CTW flux or additional high-frequency
 338 variability is present.

339 We apply a 30-day rolling mean to average over synoptic variability. The result-
 340 ing flux is the net volume flux in the top layer. If we treat the fjord as two layers, then
 341 we can assume this flux is balanced by an opposite flux in the other layer. Therefore,
 342 the incoming flux will switch between the top and bottom layers as the pycnocline fluc-
 343 tuates, and so the total incoming flux can be written as $Q_{\text{sh}}^* = |Q_{\text{ctw}}|$, where the star
 344 indicates this is an analytical model and the subscript sh represents shelf forcing.

345 5.2 Model Shelf Circulation and Variability

346 On its ocean boundary, SF is externally forced by the circulation and variability
 347 on the continental shelf. The shelf outside SF is characterized by the confluence of PW
 348 carried in from the coastal current (East Greenland Coastal Current, EGCC) and AW
 349 transported along Sermilik Trough (ST, Fig. 4). Closer to the surface, the EGCC can
 350 be seen as a westward flowing current carrying relatively cold water (Fig. 4a). The gra-
 351 dient between these two water masses is relatively diffuse indicating lateral mixing over
 352 the shelf and trough. At greater depths, relatively warm AW is steered into the fjord along
 353 ST, although there are recirculation cells within the trough system (Fig. 4b). The across-
 354 shelf isopycnal gradient (discussed later this section) sinks towards the coast resulting
 355 in lighter, cooler water closer to the fjord at a fixed depth.

356 The shelf properties upstream (east) of SF (Fig. 1, red line) vary in response to
 357 both wind forcing and external water mass variability. Two month averages of temper-
 358 ature in the NG run are highest in the fall (Sep. – Oct.) and coolest in the spring (Mar.

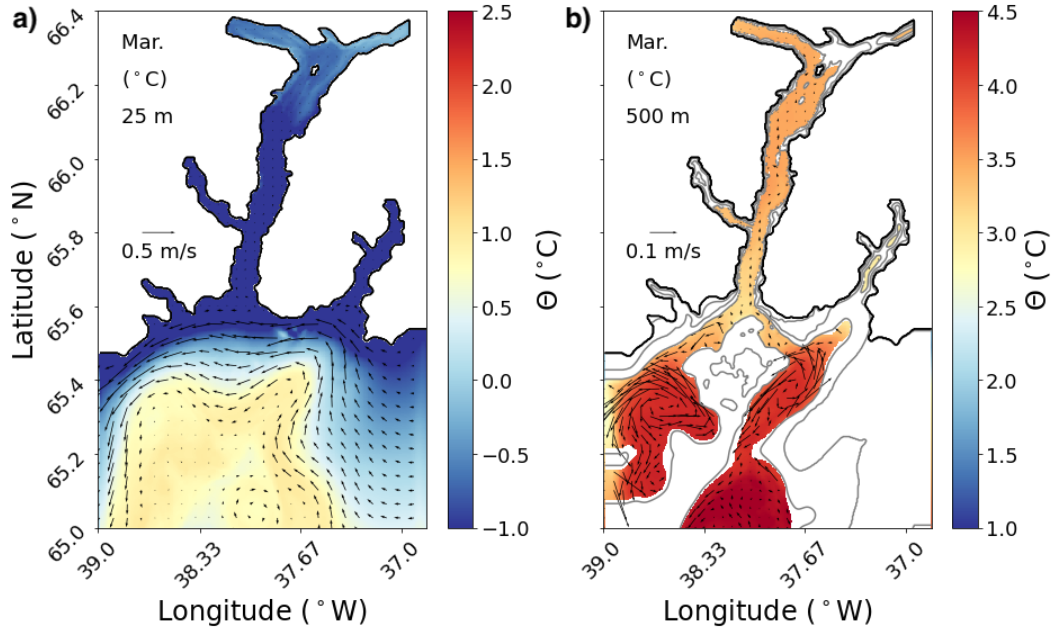


Figure 4. Plan view of temperature (color) and velocity (vectors) showing the coastal current at 25 m and the inflowing AW at 500 m in Sermilik Trough. Each figure is produced from the monthly average (March 2017) of temperature and velocity from the NG run at (a) 25 m depth and (b) 500 m depth. The depth contours are 100, 250 and 450 m. Note the different colorbars and velocity scales between the two panels.

359 – Apr., Fig. 5). In September, when the waters on the shelf are warmest, the AW ex-
 360 tends all through the water column and onto the shelf (Fig. 5e). During the rest of the
 361 year, a cold PW cap is present close to the coast, however its lateral extent appears vari-
 362 able and dependent on the steepness of the isopycnal slope. The density gradients across
 363 the shelf are strongly correlated with the daily along-shelf wind stress ($r = 0.78$, $p <$
 364 10^{-3}). Therefore, the isopycnals are compact and relatively flat in the summer months
 365 when the winds are weaker. The isopycnals start to steepen in the fall and early winter
 366 in response to downwelling-favorable winds. When the isopycnals are steepest, the
 367 ratio of cold PW to warm AW is highest. Additionally, the coastal current is strongest
 368 in the fall and winter when isopycnals are steepest (Fig. 6), consistent with geostrophy.
 369 The upstream transect shows little difference in properties between the NG and WG run
 370 (not shown), and therefore, we assume the forcing associated with isopycnal displace-
 371 ment on the shelf is active and equivalent in both runs.

372 We also examined the coastal current downstream (west) of the fjord. The NG and
 373 WG runs diverge and a relatively fresh wedge can be observed close to the coast in the
 374 WG run July through September (Sup. Fig. 3). However, in these downstream sections
 375 we do not observe substantial differences in temperature or current velocity (Sup. Fig.
 376 3 and 4).

377 5.3 Fjord Circulation and Properties (No Glacier)

378 In the NG run, the circulation in the fjord responds to shelf forcing driven in large
 379 part by local, along-shelf, winds. To examine the circulation, we focus on a cross-section
 380 at SF Line 3 as this location is closest to the mooring SF4 and is representative of cir-
 381 culation away from mixing processes at the head and the mouth of the fjord. We find

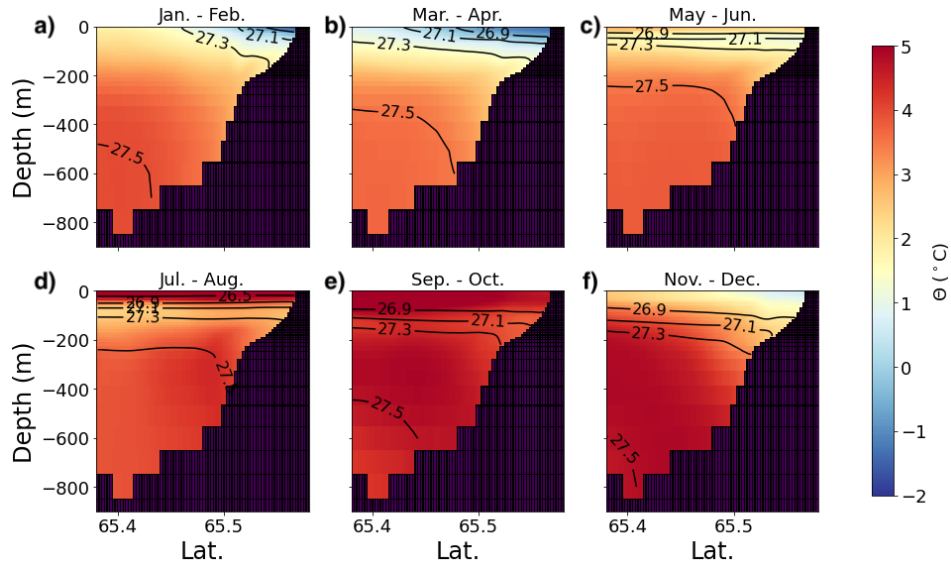


Figure 5. Isopycnals separating surface and trough waters are flat in the summer months and steep in the winter months. Each panel shows two month averages of coastal section temperature (No Glacier run, see Fig. 1 for location). View is facing west and is perpendicular to coastal current. Contours are isopycnals of potential density anomaly (26.5, 26.9, 27.1, 27.3, 27.5).

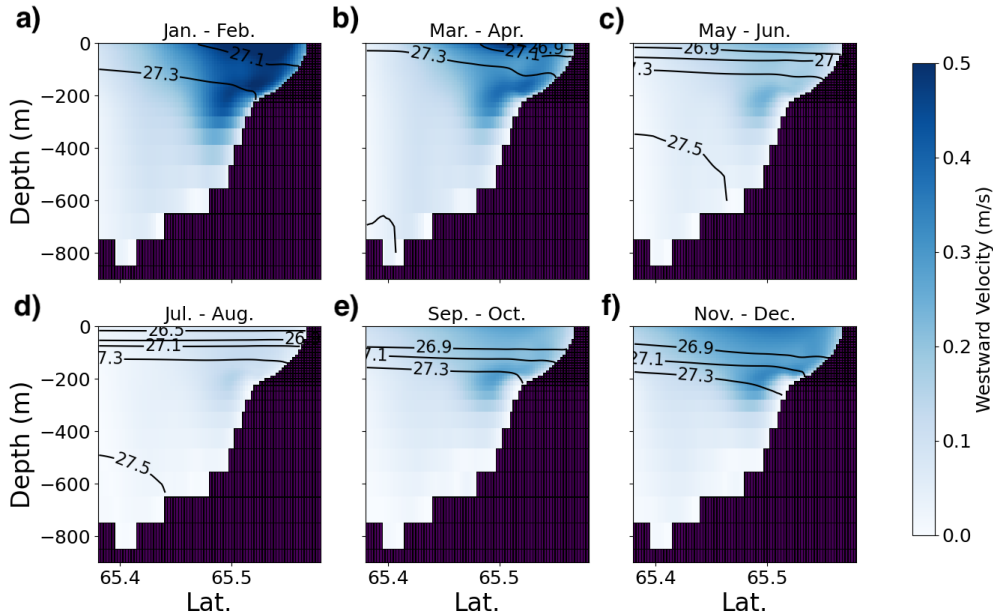


Figure 6. The coastal current is strongest in winter and weaker in summer. Each panel shows two month averages of westward velocity ($-U$) (No Glacier runs). View is facing west and is perpendicular to coastal current. Contours are isopycnals of potential density anomaly (26.5, 26.9, 27.1, 27.3, 27.5).

382 that the circulation at the SF Line 3 varies seasonally, exhibits signs of being rotationally-
 383 influenced and is characterized by reversals with depth (Fig. 7a-c). The strongest av-

384 erage flow is observed in spring with inflow at depth and outflow around 100 m. By Oc-
 385 tober, the circulation at depth has reversed. The time-varying aspects of this circula-
 386 tion will be examined in greater detail in Section 7.

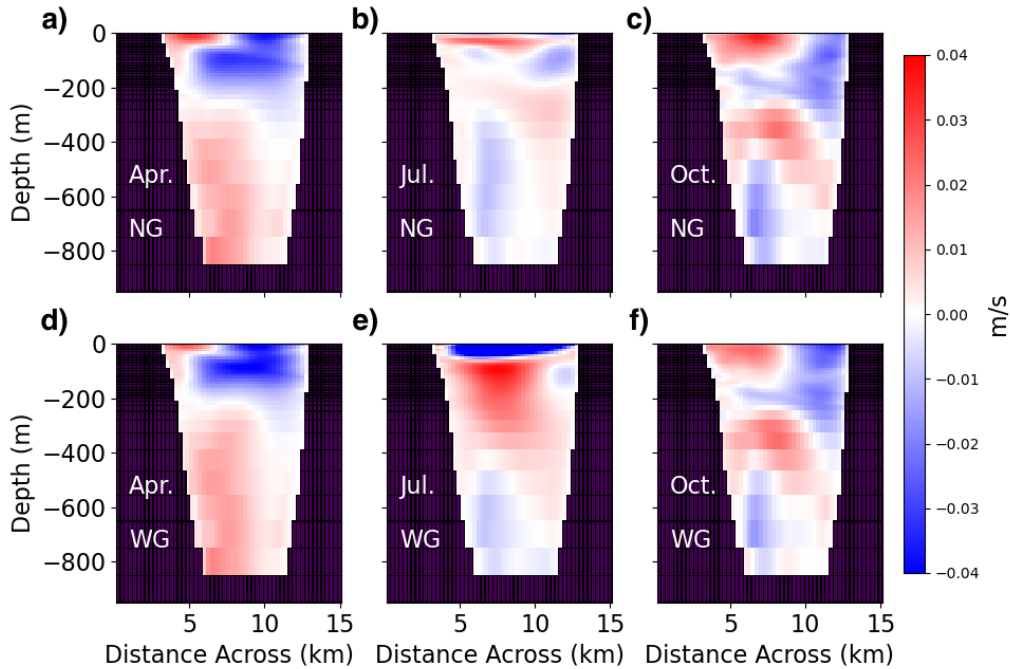


Figure 7. (a–c) monthly averages of velocity at the mouth of the fjord in April, July and October for the NG run. d–f) in April, July and October for the WG run. Positive velocities are flowing into the fjord.

387 Compared to the shelf section, variability of temperature and density along fjord
 388 is weak (Fig. 8a–c). Isopycnals lie flat within the fjord and only have a notable slope in
 389 the upper 100 m and approaching topography. The fjord shoals from 900 m at the mouth
 390 to 500 m near the branching point (70 km) and increases in depth again as it approaches
 391 Helheim glacier (90 km). The isopycnal 27.45 kg/m^3 associated with deep, relatively warm
 392 water can be seen to reach its shallowest depth (and maximum thickness) during July,
 393 but the warmest waters are present in October.

394 A width-averaged overturning streamfunction demonstrates the changes in fjord
 395 circulation between April and October. The overturning circulation is positive in April
 396 with inflow at depth and outflow near the surface (Fig. 9a). In July, the circulation is
 397 sluggish and slightly negative (Fig. 9b). By October, the circulation appears three-layered
 398 with a fully reversed circulation at depth and a shallower cell in the upper 250 m (Fig.
 399 9c).

400 In the the absence of glacial forcing (NG run), the mid-fjord properties (red, Fig.
 401 10) mirror the shelf variability (black, Fig. 10) in temperature and salinity (TS) space.
 402 WPW is found seasonally near the surface ($\Theta \approx 8 \text{ }^\circ\text{C}$), PW ($\sigma \approx 27.0 \text{ kg/m}^3$) is found
 403 at the temperature minimum, and AW is the saltiest and densest water ($\sigma \approx 27.5 \text{ kg/m}^3$).
 404 We see that in the winter months (Jan. – Apr.) the fjord model properties lie in between
 405 PW and AW, and the fjord can be described as a two-layer system (Fig. 10). As the sur-
 406 face warms, a distinctive “U” shape forms from the three water masses present: WPW,

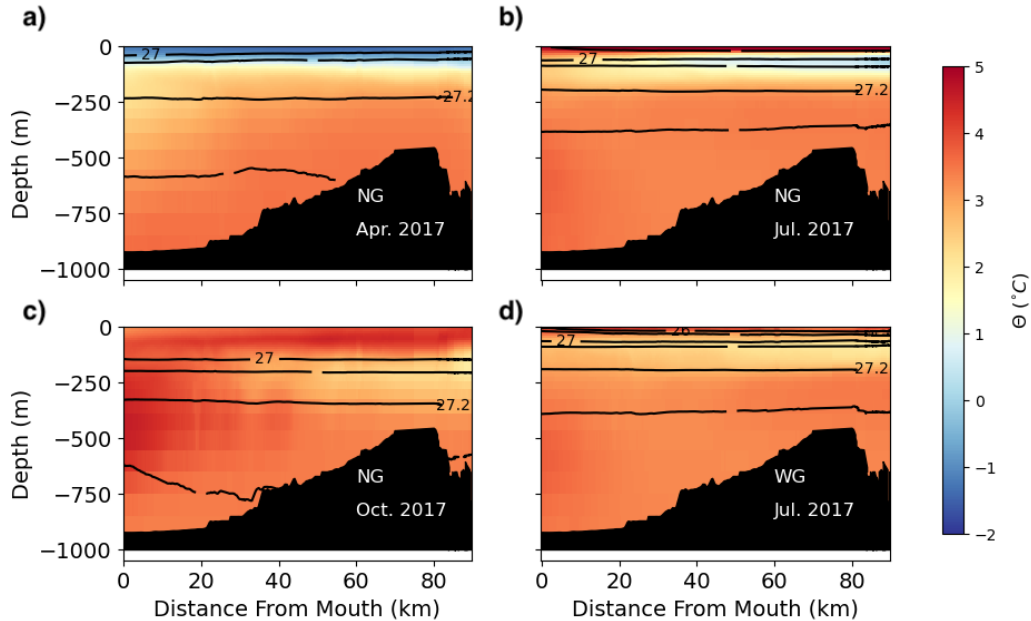


Figure 8. Along-fjord gradients are relatively weak, but properties change seasonally. Width-averaged monthly temperature in April (a) and July (b) and October (c) for the NG run and July (d) for the WG run. The contours are isopycnals of potential density anomaly (26, 27, 27.15, 27.35, 27.45 kg/ m³).

407 PW and AW. As the surface cools, the system starts adjusting back towards a two-layer
 408 system.

409 To summarize the results of this section: across-shelf isopycnal gradients are steep-
 410 est in winter when the winds are strongest, fjord circulation is influenced by rotation but
 411 still exhibits vertical shear, and streamfunctions demonstrate significant seasonal vari-
 412 ability including reversals in mean fjord circulation.

413 6 Plume-Driven Circulation

414 The other model runs includes glacial forcing (WG) with the glacial forcing domi-
 415 nated by the subglacial discharge plume. The inclusion of subglacial discharge plumes
 416 alters the fjord circulation and temperature, especially in summer. At SF Line 3, there
 417 is substantial difference between the WG and NG runs in July, with a much stronger out-
 418 flow near the surface and less recirculation in the middle part of the fjord in the WG run
 419 (Fig. 7d–f). The non-summer months (Apr. and Oct.) show little difference in veloci-
 420 ty magnitude and structure between the two model runs. Taken as a whole, the fjord
 421 cross-sections demonstrate that the spatial structure of the circulation is complex and
 422 highly variable. In this study, we are primarily interested in overturning (vertical shear)
 423 and therefore will be analyzing width-integrated exchange flows.

424 The July temperature distribution in the fjord is similar in WG and NG except in
 425 upper 100 m where it is 2°C warmer than in the NG run (Fig. 8d). This difference can
 426 be attributed to subglacial discharge entraining ambient AW and bringing it up to shal-
 427 lower depths via the plume. The overturning steamfunction in the WG run shows the

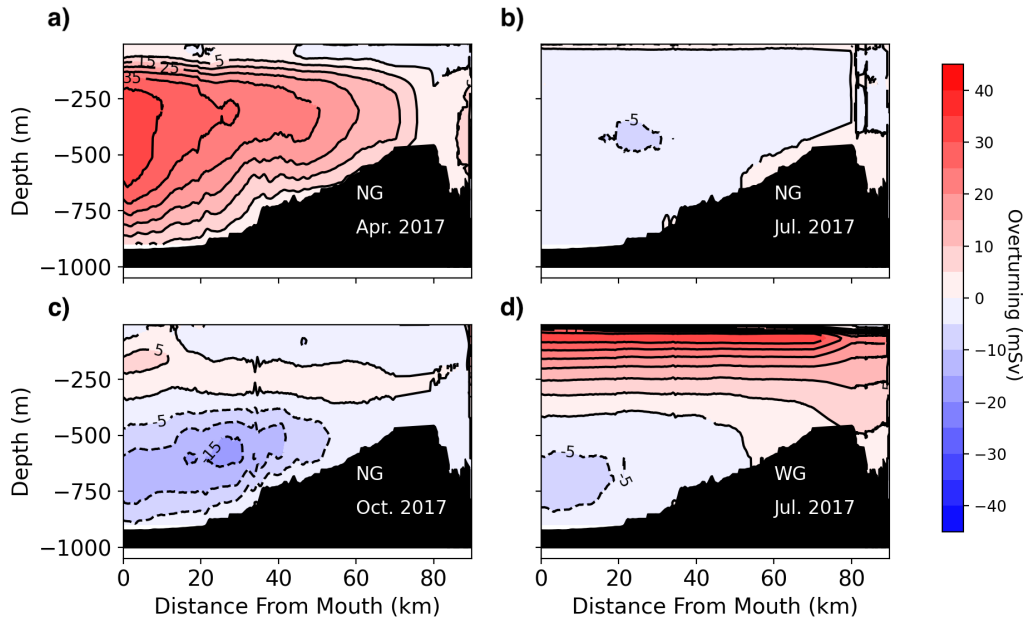


Figure 9. The streamfunction reverses between April and October in the NG run. Width and monthly-averaged overturning streamfunction over April, July and October (NG), and July (WG) in 2015. Counter-clockwise flow is a positive streamfunction.

428 plume drives strong outflow near the surface (Fig. 9d). Below 400 m, the July WG stream-
 429 function is negative similar to the July NG run.

430 The TS properties in the WG run reveal the influence of the plume on fjord water
 431 properties. The WG run (blue, Fig. 10) starts diverging substantially from the NG
 432 run in June due to large amounts of subglacial discharge. This divergence follows the
 433 subglacial discharge-mixing line, and the end result is a cooler and fresher surface wa-
 434 ter mass and the "erasing" of the clear PW signal (temperature minimum). The WG
 435 run properties converge back to those of the NG run in October, and therefore we can
 436 state that the time period of subglacial discharge influence is June – September. We tested
 437 for freshwater storage by calculating the lag between subglacial discharge input and peak
 438 freshwater export (Sanchez et al., 2023). We did not observe significant freshwater stor-
 439 age with the peak export averaging a two-week delay over the three years which we at-
 440 tribute to the transit time of water (0.1 m/s) across the fjord.

441 The summer and winter CTD observations are also included in the TS plots for con-
 442 text. They show that the model surface waters are biased warm during the summer, likely
 443 due to a lack of iceberg melt.

444 7 Exchange Flow Analysis

445 7.1 Depth Coordinates Exchange-flow Structure

446 Prior to using TEF, we evaluate the temporal variability of the exchange flow in
 447 traditional depth coordinates. The volume transport at SF Line 3 for the NG run is shown
 448 in Figure 11a. With three years of data, a picture emerges of seasonal volume transport
 449 in the fjord with a reversing circulation below 200 m (Fig. 11a). The volume transport
 450 is filtered with a 30-day rolling mean to remove the first-order synoptic variability as-

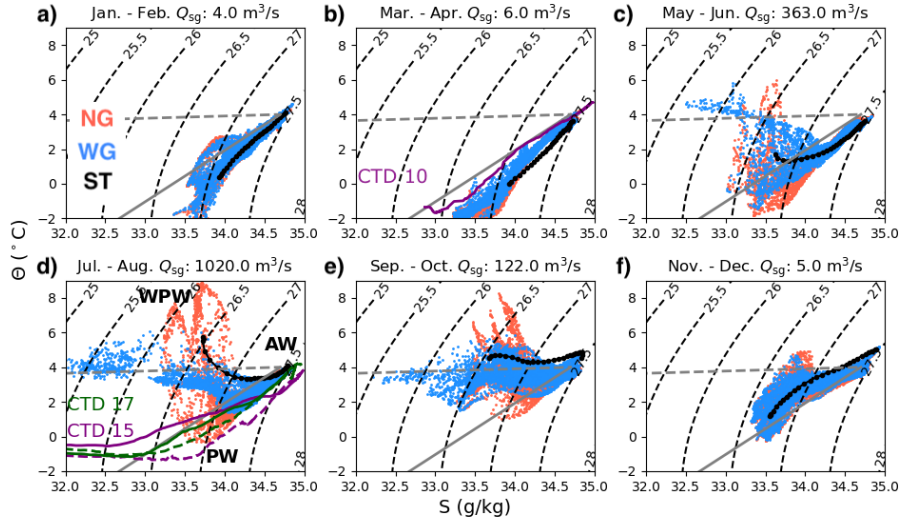


Figure 10. Each panel shows the TS properties over a 2-month period with the spread coming from time (daily) and depth. The blue dots are from the WG run and the red dots are from the NG run. The black line is the TS properties in Sermilik Trough (ST) in the NG run. The gray solid line is the melt-mixing line and the gray dashed line is a subglacial discharge mixing line. The contours are potential density anomaly. Q_{sg} is the two-month average subglacial discharge. The average TS from all CTD profiles collected in Aug. 2015 (33), Jul. 2017 (31), and Mar. 2010 (4) are in purple. Dashed and solid lines separate shelf and fjord profiles, respectively. The water mass locations are labeled in panel d.

451 sociated with the winds. The volume transport is roughly in two layers below 200 m (Fig.
 452 11). The circulation is inflowing at depth in the spring and reverses to outflowing dur-
 453 ing the summer. This circulation is interrupted, especially in the upper 200 m, by the
 454 cumulative effects of wind events that are not completely filtered out. The seasonal cycle
 455 dominates over interannual variability.

456 The isolated plume-driven transport (the WG run with the NG run subtracted)
 457 shows a strong seasonal cycle with an increase in outflow during the summer and a com-
 458 pensating inflow between 200 and 500 m (Fig. 11b). The primary outflow depth appears
 459 to rise and fall each summer consistent with a neutral buoyancy depth that is based on
 460 the magnitude of subglacial discharge.

461 Applying TEF to SF line 3 enables us to calculate the seasonal volume transport
 462 of the fjord in density space (Fig. 12) and allows direct connection with water mass vari-
 463 ability. The composite TEF analysis shows that the NG transport is generally concen-
 464 trated in the most dense layers. During the first half of the year, the deep flow is posi-
 465 tive with inflow at depth and outflow at lighter densities. As seen in depth space (Fig.
 466 11), the flow reverses in the second half of the year. Upon closer inspection, the inflow-
 467 ing density from January to June can be seen to be getting progressively denser filling
 468 the fjord with a greater concentration of AW. When the exchange reverses, the outflow-
 469 ing deep water can be seen getting progressively lighter. The WG circulation stands out
 470 in the summer and it overtakes the background NG circulation (Fig. 12). The inclusion
 471 of the plume alters the total circulation enough to prevent the deep reversal from occur-
 472 ring until later in the fall. The TEF composite profiles also highlight the multi-layered
 473 exchange occurring in SF (Fig. 11 and 12). In the winter months, there are multiple zero

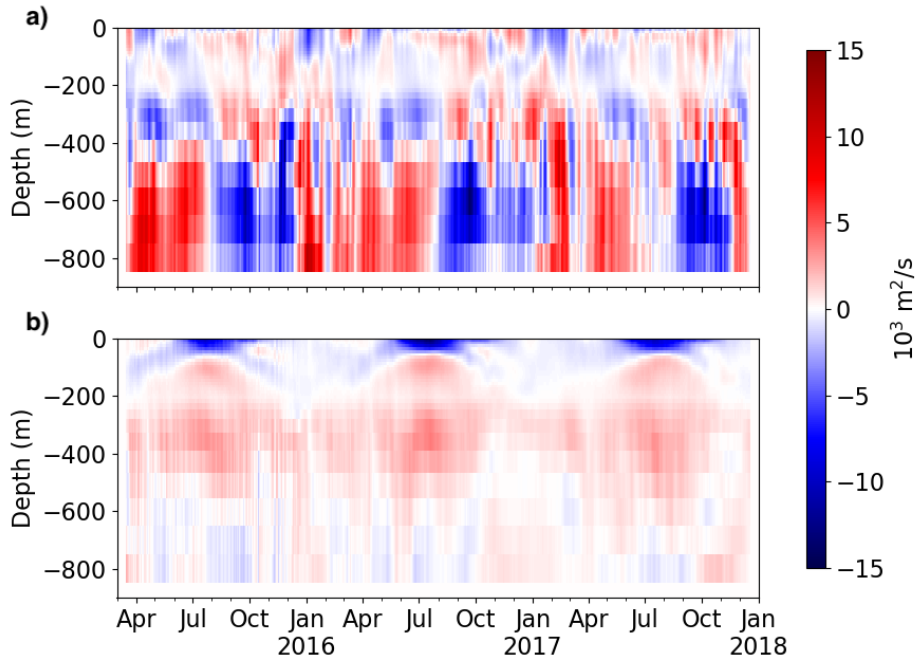


Figure 11. a) 30-day rolling mean volume transport in the NG run at SF line 3 as a function of depth and time. Positive transport is into the fjord. b) The difference between the volume transport in the WG run and the NG run at SF line 3.

474 crossings separating the outflowing and inflowing cores at 27 kg/m^3 and 27.3 kg/m^3 re-
 475 spective. The multiple inflows raise questions as to the physical meaning of TEF terms
 476 such as S_{in} or S_{out} . With this caution in mind, our analysis of TEF bulk values will as-
 477 sume they are representative of a larger 2-dimensional overturning circulation.

478 7.2 Exchange Flow Connections with Wind Stress

479 The exchange flow reversal exports AW (Fig. 10 and 12) and is therefore an im-
 480 portant lever in reducing the heat available to melt. We propose that the seasonality of
 481 the winds is responsible for the reversal by flattening isopycnals across the shelf during
 482 the spring. The mean state of the winds along the shelf is consistently downwelling fa-
 483 vorable, such that a relaxation towards no winds acts effectively as upwelling. The chang-
 484 ing slope of isopycnals in Sermilik Trough are qualitatively consistent with this picture
 485 (Fig. 5).

486 The relationship between low-frequency wind forcing and the exchange reversal is
 487 tested by comparing the time derivative of low-pass along-shelf wind stress (τ_{lp}) and the
 488 sign of TEF exchange (Fig. 13). Both of these variables are related to the change in pyc-
 489 noclone depth, if the exchange sign is negative then the fjord is getting lighter (pycno-
 490 clone deepening). The exchange flow direction is represented through a 15-day low-pass
 491 Butterworth filter of $\Delta\sigma = \sigma_{\text{in}} - \sigma_{\text{out}}$ from the NG run at SF Line 3. The goal of this
 492 filter is to reduce synoptic forcing since we are interested in the change in exchange flow
 493 direction on longer timescales. When $\Delta\sigma > 0$, the exchange flow is positive with in-
 494 flow at depth. The derivative of the seasonal wind stress is significantly correlated with
 495 $\Delta\sigma$ ($r = 0.59$, $p < 10^{-3}$) suggesting that wind variability is consistent with the sign

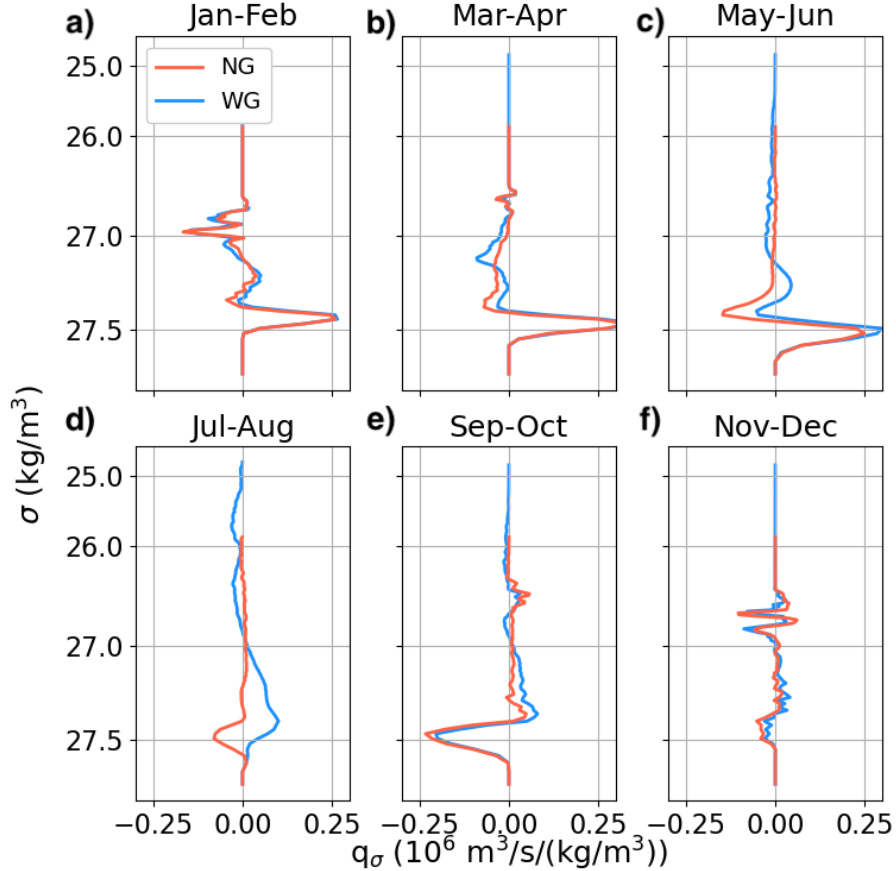


Figure 12. The AW inflow ($\sigma \sim 27.4 \text{ kg / m}^3$) becomes progressively denser until July and then reverses becoming progressively lighter. Each panel is a three-year average over the two months evaluated at SF Line 3. The x-axis is volume flux per density class. The y-axis is potential density anomaly σ . Note the y-axis is nonlinear so that greater resolution can be given to the deepest densities. Red is from the NG run, and blue is from the WG run. 50 density bins were used for this figure instead of 1000 for clarity.

496 of the exchange flow. The seasonal variability of wind stress therefore likely plays an im-
 497 portant role in setting the amount of AW in SF with relaxing winds leading to a greater
 498 concentration of AW.

7.3 Variability of TEF Bulk Properties

500 We quantify the TEF exchange volume flux as

$$Q_e = \frac{Q_{\text{in}} - Q_{\text{out}}}{2}, \quad (5)$$

501 where Q_{in} is the TEF inflowing volume flux (calculated in density space) and Q_{out} is the
 502 outflowing flux with $Q_e \geq 0$ (MacCready et al., 2018). In the NG run, the cycle of the
 503 exchange flux is consistent with the seasonal cycle of wind forcing with the greatest flux
 504 occurring during the winter months (max 60 mSv) and weak exchange during the sum-
 505 mer (max 10 mSv) (Fig. 14a). The exchange flux in the WG run diverges from the NG

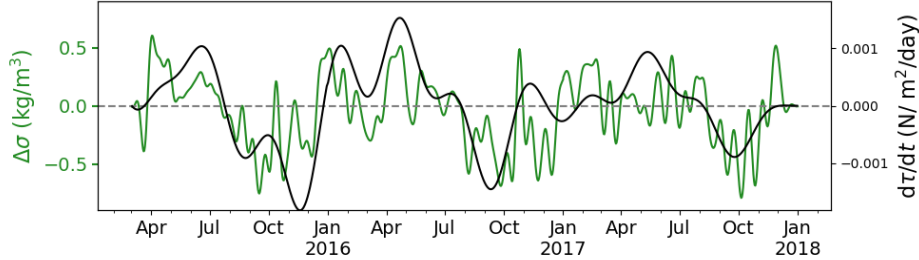


Figure 13. Flow reversals are correlated with changing wind stress. In green (left axis) is the difference between the TEF calculated $\sigma_{in}, \sigma_{out}$ at SF line 3 smoothed with a 15-day low-pass filter. Positive indicates inflow at depth. The data come from the NG run. The right axis (black) is the derivative of the (90-day low pass) along-shelf wind stress

506 run during the summer with peak exchange around 40 mSv. Since the plume forcing is
 507 strongest in the summer when the shelf-driven circulation is weakest, the exchange ex-
 508 ceeds 30 mSv for the majority of the year. In the WG run, the exchange minimum is found
 509 in the non-summer months and varies from year to year depending on wind strength.
 510 In 2015 and 2016 the minimum occurs in November after the plume has shut off and dur-
 511 ing a relatively weak period of winds, but in 2017 the minimum occurs in March.

512 To isolate the plume forcing against the background shelf forcing, we separate the
 513 exchange flux into the plume-driven exchange (WG-NG) and shelf-driven exchange (NG).
 514 The plume-driven exchange flux peaks in July and the timing coincides with the input
 515 of subglacial discharge (Fig. 3b)

516 We compare the shelf-driven exchange (NG) with CTW theory (Eq. 3, Section 5.1).
 517 Forcing other than CTW exists in the NG run, but we use the CTW theory as a first-
 518 order approximation of the exchange flow. The exchange flux predicted by variation in
 519 pycnocline depth is correlated with the NG exchange flux ($r = 0.48$, $p < 10^{-3}$, Fig.
 520 14c). However this is because both fluxes peak in winter. Individual peaks in the CTW
 521 theory do not necessarily align with peaks in the NG flux. The theory suggests minimal
 522 impact of CTWs in summer when there is still an exchange on the order of 20 mSV. Clearly,
 523 additional factors are influencing the exchange in the NG run, but the comparison in-
 524 dicates that CTW dynamics can be a significant contributor to the background exchange
 525 flow.

526 Subglacial discharge drives a large salt exchange and export of freshwater onto the
 527 shelf (Fig. 14d). The salt exchange is defined as $Q_e \Delta S$ where $\Delta S = S_{in} - S_{out}$, with
 528 Q_e calculated using salt coordinates. When $\Delta S > 0$, the exchange flow is positive with
 529 inflowing salty water at depth and the export of fresher water above. The plume is the
 530 largest seasonal driver of the salt flux with the WG run salt flux peaking during the sum-
 531 mer (Fig. 14d). In the absence of subglacial discharge forcing, the exchange salt flux is
 532 relatively weak during the summer. The rest of the year the salt flux is variable due to
 533 wind forcing, but is generally negative in the fall and positive during the winter when
 534 the circulation reverses.

535 The heat exchange is defined as $Q_e \Delta \theta \rho c_w$ where $\Delta \theta = \theta_{in} - \theta_{out}$, c_w is the spec-
 536 ific heat capacity of seawater and Q_e is calculated in temperature coordinates. When
 537 $\Delta \theta > 0$, the exchange flow is positive with inflowing warm water at depth and the ex-
 538 port of cooler water above. The heat exchange is dominated by the shelf-driven circula-
 539 tion (Fig. 14e) and therefore fluctuates between positive and negative depending on
 540 wind-strength. The addition of subglacial discharge results in a negative heat exchange

541 in the WG run, that is the fjord is exporting heat, but this flux is small in comparison
 542 to the larger fluctuations in the winter.

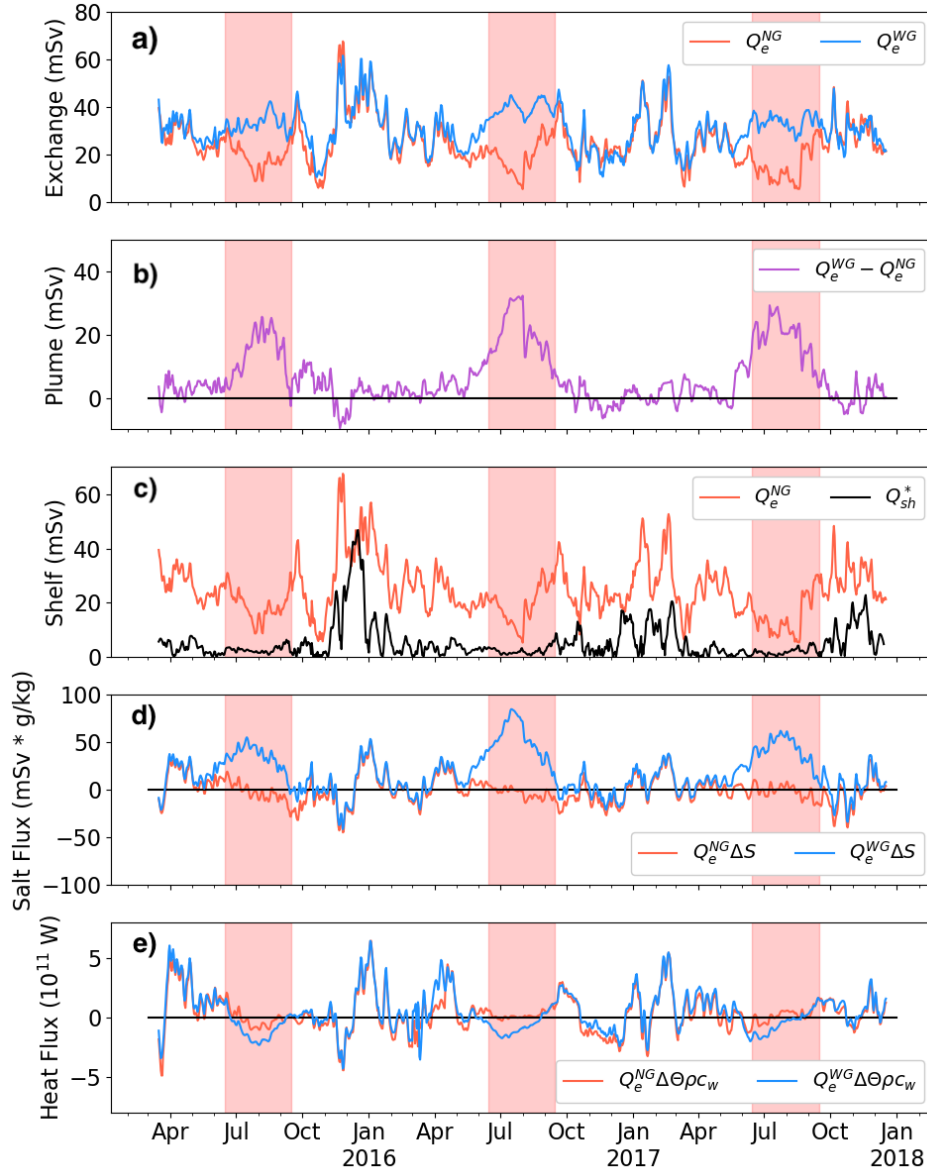


Figure 14. The shelf-driven and plume-driven exchange fluxes have peaks during the winter and summer months, respectively. a) Exchange flux at SF line 3 in the NG and WG run. Units are in mSv ($10^3 \text{ m}^3/\text{s}$). Red shading indicates summer period (Jun. 15 – Sep. 15). b) The difference between the WG and NG runs at SF line 3. c) Exchange flux estimated from coastal-trapped waves (J18) and the NG run. d) Salt Flux from the exchange flow. The black line separates positive (incoming salt) from negative salt flux. e) Heat flux from the exchange flow. Positive Heat flux would make the fjord warmer.

543 In summary, the TEF results and shelf-plume forcing comparison indicate that the
 544 timing of subglacial discharge results in a strong exchange flow when the shelf-driven circulation (Q_e^{NG}) is relatively weak. The peaks in shelf and plume-driven circulation (Q_e^{WG} -
 545

546 Q_e^{NG}) are consistent with the timing of subglacial discharge and CTWs lending confi-
 547 dence to our understanding of the drivers of the exchange flow. The exchange salt flux
 548 in the WG run consistently peaks in the summer, while both the heat and salt flux in
 549 the winter are more variable.

550 7.4 Along-Fjord Variability of Q_e

551 Given the different forcing source locations, we expect the shelf-driven circulation
 552 and plume-driven circulation to produce different along-fjord variability. The shelf-driven
 553 circulation, active in non-summer months, is most intense at the mouth of the fjord and
 554 decays with distance (Fig. 15a). In contrast, the plume-driven circulation in summer (Jun.
 555 – Aug.) decays only slightly as it flows down the fjord. The bulk TEF properties S_{in} and
 556 S_{out} are nearly constant along the length of the fjord (Sup. Fig. 7) suggesting that ver-
 557 tical mixing is weak in the fjord interior.

558 The flushing time V/Q_e is defined as the volume upfjord of a section divided by
 559 the exchange flux and is a scaling for residence time within the fjord. The flushing time
 560 when the shelf-driven circulation dominates (Winter, Spring, Autumn) is always larger
 561 than the flushing time in summer and only decreases to between 100 – 150 days (Fig.
 562 15b). The plume-driven circulation flushing time is similar to winter near the mouth of
 563 the fjord, but drops linearly towards the head resulting in a flushing time of 50 days closer
 564 to Helheim Fjord. The contrasting along-fjord slopes suggests the plume-driven circula-
 565 tion is more effective at renewing the fjord than the shelf-driven circulation. For a long
 566 fjord such as SF, the magnitude of the shelf-driven circulation has been reduced by 66%
 567 70 km upfjord while the plume-driven circulation is most intense near the terminus where
 568 entrainment is high (5 – 10 km). This flushing time is meant to provide a scaling for res-
 569 idence time within the fjord, and we note other residence time scalings such as the fresh-
 570 water fraction method produce different residence times, but a qualitatively consistent
 571 picture.

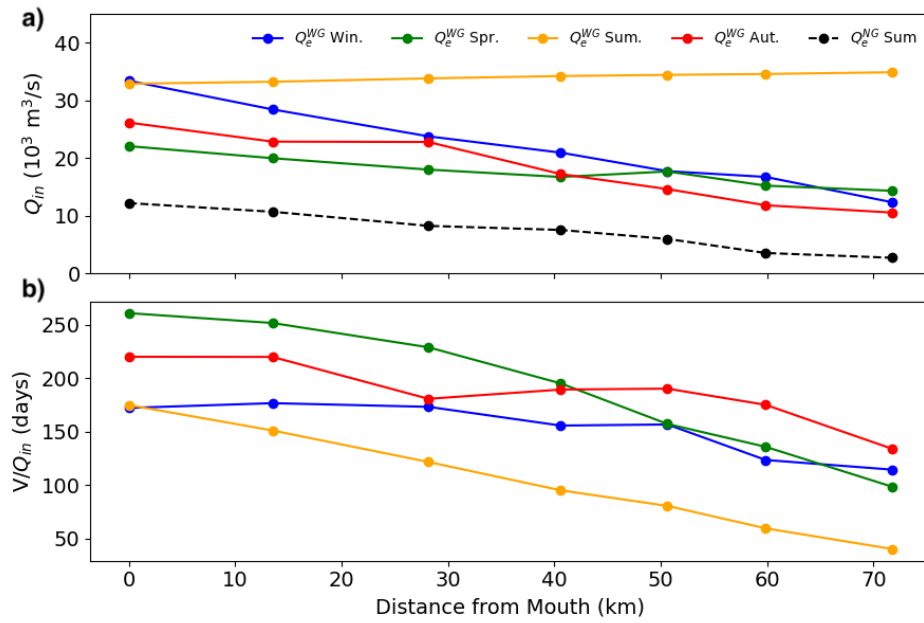


Figure 15. The exchange flux associated with winds decreases from the mouth, while the exchange flux from the plume is constant along the fjord. a) Along-fjord TEF exchange flux in 2016. Seasons are averages. The solid lines are from the WG run and the black dashed line is from the NG run during the summer. b) The fjord volume upstream of the mouth divided by the exchange flux. Win is Winter (Jan. – Feb.), Spr. is Spring (Mar. – May), Sum. is Summer (Jun. – Aug.), Aut. is Autumn (Fall, Sep. — Nov.).

8 Discussion

8.1 Warm-water Seasonality

Identifying the heat content variability of glacial fjords is essential given the sensitivity of submarine melting to warm water. An increase in fjord heat content can be driven by an increase in AW temperature or by an increase in the relative concentration of warm AW to cold PW. We find that the vertically-averaged temperature of the fjord, and thus vertically-averaged thermal forcing, peaks in the fall. The temperature maximum in the fall is a result of both warm water intruding into the fjord near the surface and seasonally-warmed AW advecting into the fjord at depth (Fig. 8c) and is consistent with observations (Sutherland et al., 2013; Harden et al., 2014). However, we find that the greatest ratio of AW to PW, defined roughly from the height of the 27.3 kg/m^3 isopycnal, occurs in July as a result of relaxing isopycnals. Therefore, these two warming mechanisms have different seasonal patterns. A warming of the Irminger Sea would result in a larger temperature anomaly at depth in fall, while a reduction in along-shelf winds would increase the thickness of the AW layer and result in a larger temperature anomaly in spring or summer. Of course, fjord circulation and its seasonality will modify the amount of oceanic heat that ultimately reaches the glacier. For example, while the temperature remains relatively constant along the fjord, volume transport is not. Consequently, the oceanic heat flux decays if it is shelf-driven but remains nearly constant if it is plume-driven (Fig. 15). The impact of external heat on glaciers will depend on iceberg concentration, the mechanism of fjord heat transport, and processes at the ice-ocean interface, which are still poorly understood.

We would also like to point out that the inclusion of substantial submarine melting (e.g. from icebergs) is likely to change the heat flux interpretation during the summer. In the WG run, the exchange heat flux is negative during the summer as a result of upwelled AW and a shallow outflowing plume (Fig. 8d). If the upper-layer was properly cooled, we would observe a positive heat flux. A steady and positive heat flux would be consistent with observations (Jackson & Straneo, 2016). As the streamfunction shows (Fig. 9d), the plume-driven circulation drives transport between 200 and 500 m all the way towards the glacier, and therefore, increased subglacial discharge should lead to increased heat transport and greater melting of both the terminus and icebergs. Inclusion of melting could then lead to a feedback with an increased buoyancy-driven circulation (Kajanto et al., 2023; Zhao, Stewart, & McWilliams, 2022). To explore this question fully, more realistic melting needs to be included in numerical models (Schulz et al., 2022).

8.2 Relationship Between Glacial Stability and Shelf Forcing

Warmer ocean and atmospheric temperatures have been linked to increased glacial retreat in east Greenland (Straneo et al., 2011; T. R. Cowton et al., 2018). In SF, glacial retreat has also been correlated with the negative phase of the North Atlantic Oscillation (NAO) index (Andresen et al., 2012, 2014), the dominant mode of atmospheric climate variability in the North Atlantic related to pressure differences between Portugal and Iceland. A negative NAO index is associated with increased AW content relative to PW, leading to increased heat transport across the shelf (Christoffersen et al., 2011). The positive phase of the NAO index is correlated with glacial stability despite increased low-pressure systems and storms along the east Greenland coast potentially increasing circulation within fjords (Harden et al., 2011; Andresen et al., 2014). Our model is consistent with this correlation, as we find that under reduced winds (and downwelling), shelf isopycnals flatten and the fjord-shelf exchange promotes an increase in AW. This mechanism has recently been observed on shorter timescales (1-10 days) using satellite observations (Snow et al., n.d.). Therefore, our results extend into the fjords the dynamical connection between large-scale wind variability and heat transport across the shelf

(Christoffersen et al., 2011). We find the seasonality and direction of the along-shelf winds play an important role in setting oceanic thermal forcing of the glacier.

8.3 Implications for Fjord Renewal

While the seasonality of the along-shelf winds play an important role in increasing the heat content in SF, we find that the circulation induced from shelf forcing decays away from the mouth and has a reduced affect closer to the fjord head. In contrast, the plume-driven circulation in summer is capable of driving renewal across the whole length of the fjord. Therefore, we would expect fjord properties (e.g. heat, nutrients) close to the terminus to have the quickest renewal rates in summer when subglacial discharge is strongest. Additionally, near-terminus circulation is an important control of glacial melt rates. In large fjord systems such as Sermilik, the shelf-forced circulation decays limiting the direct effects of storms and shelf winds on submarine melting.

8.4 Fjord Mixing

There appears to be weak mixing in the main channel of Sermilik Fjord. TEF bulk properties of Salinity and Temperature (Sup. Fig. 6 and 7) are nearly constant along the fjord. During the winter, even though CTWs can drive a rapid fluctuation, they might contribute only modestly to mixing. Low dissipation would be consistent with modeling studies focusing on CTWs on Greenland’s shelf and fjords (Gelderloos et al., 2021, 2022). During the summer, when the circulation is plume-dominated, the weak mixing indicates that the outgoing flux is primarily set by the subglacial discharge plume parameterization. The addition of icebergs is likely to add additional mixing downfjord and would be consistent with some observations (Mulwijk et al., 2022).

9 Conclusion

Glacial fjords are critical to the climate system by exchanging heat and salt between the ice sheet and open ocean. We analyzed the output from two three-year simulations of a glacial fjord with realistic forcing. One simulation included glacial and shelf forcing (WG) while the other only included shelf forcing (NG), allowing us to identify the relative roles of shelf and plume forcing on shelf-fjord exchange. Using the NG run, we found that the shelf forcing was able to drive significant exchange even in the absence of glacial forcing. Additionally, we found that the sign of the exchange flow is related to the seasonality of the along-shelf wind stress which controls the across-shelf isopycnal gradients. When downwelling winds subside, shelf isopycnals flatten and the fjord fills with warm AW in the summer. In SF, the minimum of the along-shelf wind stress happens to coincide with peak glacial forcing generating two distinct regimes, a shelf-driven circulation in non-summer months with variable heat and salt exchange, and a plume-driven circulation in the summer with a large salt exchange. The plume-driven exchange shows little along-fjord variability and is more effective at renewing tracers than the shelf-driven circulation which peaks at the fjord mouth. Therefore, the direct effect of the shelf-driven circulation on driving melt-rate variability is likely secondary to thermal forcing. Key limitations of this study are a parameterized ice face which produces weak melting outside of the plume and a lack of icebergs which are likely a considerable heat sink in the fjord.

Appendix A Model and Data Comparison

A1 Observational Data

The model runs presented in this paper are some of the first multi-year simulations of a Greenland glacial fjord with realistic atmospheric and oceanic forcing. Evaluation

Table A1. Moored observations and CTDs from 2015 – 2017. Θ is Conservative Temperature, S is absolute salinity, P is pressure, V is velocity.

Label	Instrument	Depth	Deployment Time	Sample Resolution	Variables
CM6	SBE 37 MicroCAT	350 m	August 2013 – August 2016	15 min	Θ, S, P
CM0	SBE 37 MicroCAT	60 m	August 2015 – July 2017	15 min	Θ, S, P
SF4	SBE 37 MicroCAT	400 m	August 2015 – July 2017	15 min	Θ, S, P
SF6	SBE 37 MicroCAT	350 m	August 2015 – July 2017	15 min	Θ, S, P
SF4 ADCP	75 kHz RDI Teledyne Workhorse Long-Ranger ADCP (Upward Facing)	381 – 41 m (10 m bins)	August 2015 – July 2017	30 min	V
OW1 ADCP	75 kHz RDI Teledyne Workhorse Long-Ranger ADCP (Upward Facing)	143 – 18 m (5 m bins)	August 2015 – July 2017	30 min	V
CTD 2015	SBE 25plus MicroCAT	Full Depth	August 2015	1 m	Θ, S, P
CTD 2017	SBE 25plus MicroCAT	Full Depth	July 2017	1 m	Θ, S, P

668 and comparison of the model against observations is limited to a select number of moorings, although these moorings span different regions of the fjord-shelf system (Fig. 1).
669 We compare the model to three moored Conductivity, Temperature and Depth (CTD)
670 instruments (Table A1) from August 2015 to July 2017 located on the shelf at 350 m and
671 in the fjord at 60 m and 400 m (Fig. 1). We also compare the model output to moored
672 Acoustic Doppler Current Profiler (ADCP) velocity data collected in the fjord and on
673 the shelf (Table A1). We compare the model output to 64 ship-based CTD profiles col-
674 lected during summer surveys in 2015 and 2017. Lastly, we also include 4 winter XCTD
675 profiles from March 2010 for additional context.
676

677 We evaluate the model using the Skill Score (SS, Murphy, 1988) defined as

$$\text{SS} = 1 - \frac{\frac{1}{N} \sum_{i=1}^{i=N} (m_i - o_i)^2}{\frac{1}{N} \sum_{i=1}^{i=N} (o_i - \bar{o})^2} = 1 - \frac{\text{MSE}}{\text{STD}_o}, \quad (\text{A1})$$

678 where m_i is a model value, o_i is the observation value, the overbar denotes an average,
679 (R)MSE is the (root) mean square error, STD is the standard deviation and there are
680 N paired model and observation points. The SS provides a metric for comparison across
681 different model parameters, such as temperature and salinity, and is a commonly used
682 tool when evaluating realistically forced models (e.g., Sutherland et al., 2011; Ralston
683 et al., 2010; Liu et al., 2009). It can be shown that $\text{SS} = r^2 - \text{VB} - \text{MB}$, where r is the cor-
684 relation coefficient, VB is the variance bias, and MB is the mean bias (Ralston et al., 2010;
685 Sutherland et al., 2011) and thus the score evaluates the data across multiple dimensions.
686 A $\text{SS} = 1$ indicates perfect agreement between the model and observations, but in gen-
687 eral a SS above 0.2 is considered good.

688 We use r to diagnose the covariance between two variables. The statistical signif-
689 icance of the correlation coefficient is determined using the effective degrees of freedom
690 defined as the e-folding scale of the autocovariance of the observations (Emery & Thom-
691 son, 2001; Lindeman et al., 2020).

A2 Model and Observation Comparison

To lend support that the model results are applicable to the real world Sermilik Fjord, we compare the WG model time series to 3 moored CTD instruments. The moored instruments recorded temperature and salinity on the shelf at 350 m and in the fjord at 60 m and 400 m from August 2015 – July 2017. The model boundary conditions were shifted in temperature and salinity to match the mean shelf mooring (CM6). The model appears to do a reasonable job of recreating the seasonal temperature variability in the shallow part of the fjord ($r = 0.85$), but has a significant warm bias and a resulting weak SS. The warm bias in the model PW during the summer was captured by the CTD profiles (Fig. 10), but the model does a better job of capturing the cooler PW temperature in the winter (Fig. A1c). The model is less capable of recreating surface salinity ($SS < 0$) and misses the large salinity minima which occur in the fall. The deeper moorings, especially the one on the shelf, do a better job of recreating salinity variability and temperature variability capturing both the minima in winter and the maxima in summer. (Table A2, Fig. A1).

We compare the volume transport from the model with the transport calculated from the ADCP (Sup. Fig. 2). Splitting the transport into seasons, the observed transport and standard deviation in the summer months (Jun. – Aug.) is 74 ± 26 mSv (10^3 m³/s) and non-summer months (Oct. – May) is 26 ± 7.7 mSv. The modeled transport is 33 mSv in summer and 36 mSv in the non-summer; both are within 1.6 standard deviations of the observed transport. Although the model transport appears to be underestimating transport in the summer. This underestimate is potentially driven by a lack of iceberg melt which has been shown to increase circulation by at least 10% (Davison et al., 2020).

A3 Summary Statistics

A table of SS, r and MSE are given in Table A2. We don't calculate SS or r scores for the ADCP at SF4 since the observed transport is an estimate and not directly measured. We isolate seasonal from synoptic (1-10 day) forcing by splitting all the data up into two time series: a low-pass time series y_{lp} generated from a 30-day low pass 6th order Butterworth filter and a high-pass time series $y_{hp} = y - y_{lp}$ generated from removal of the low-pass series from the original data. Most of the SS are poor, and we can attribute this largely to differences in the MSE. The highest SS are for the deep salinity (SF4 and SF6) where the model was shifted to reduce the mean bias. The skill scores tend to improve when looking at shorter timescales (< 30 days) indicating the model is doing better at capturing wind-driven variability than the larger scale variability, a bias we attribute to lacking iceberg melt.

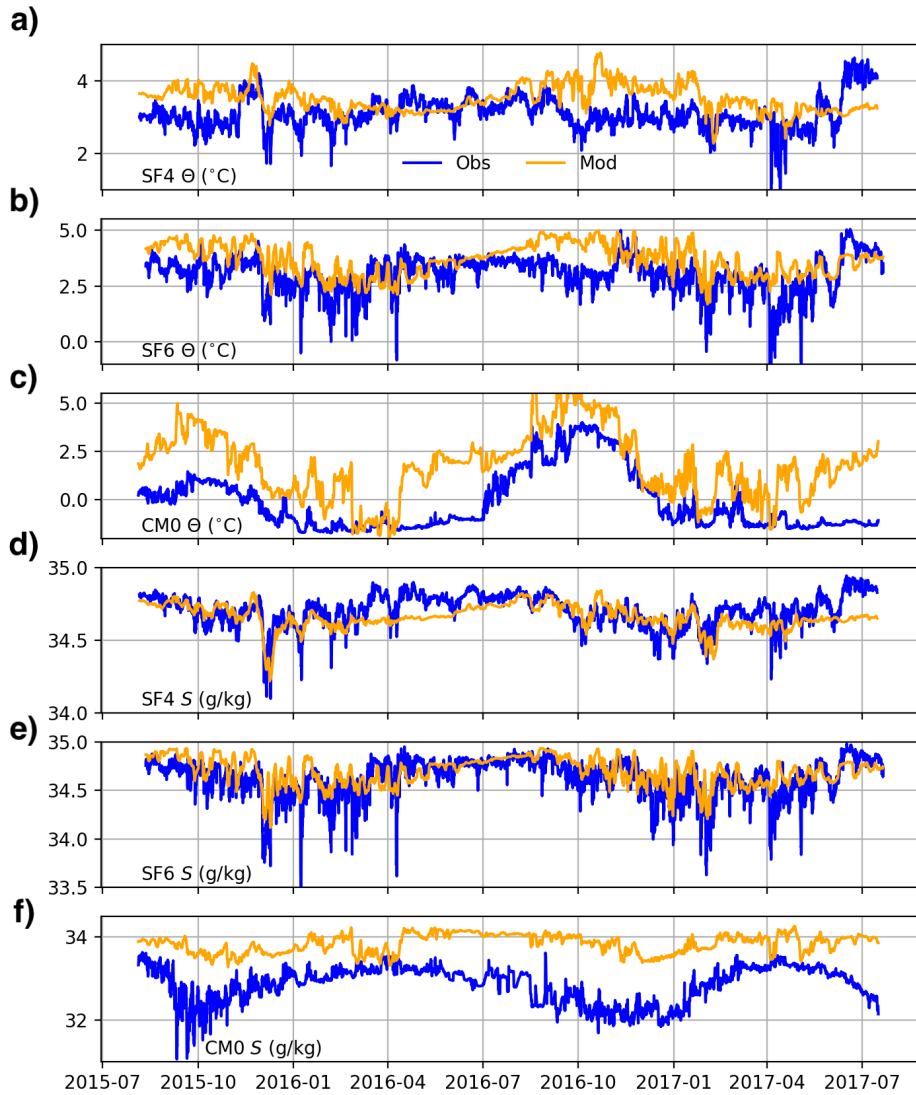


Figure A1. The model output (orange) reproduces shelf observations (blue), but cannot reproduce shallow fjord salinity. a-c) are Conservative Temperature (Θ) at SF4, SF6, and CM0 at 400 m, 350 m, and 60 m respectively. d-f) are Absolute Salinity (S) at SF4, SF6, and CM0.

Table A2. Statistics and skill scores for the mooring temperature, salinity and velocity time series. The first column is the variable and mooring. Columns 2 – 4 are the Skill Score (SS), Mean Square Error (MSE) and correlation coefficient (r) for the low-pass filtered time series, and columns 5 – 7 are statistics for the high-pass filtered time series. Significance is denoted with a star.

Variable	SS _{lp}	MSE _{lp}	r_{lp}	SS _{hp}	MSE _{hp}	r_{hp}
CM0 S	-6.0	1.1	0.42*	-0.13	0.03	0.13
CM0 Θ	-0.95	4.3	0.85*	-2.7	0.26	0.31
SF4 S	0.01	0.01	0.57*	0.12	0.003	0.50*
SF4 Θ	-1.8	0.40	-0.02	-0.33	0.08	0.21
SF6 S	0.33	0.02	0.75*	0.11	0.013	0.48*
SF6 Θ	-0.96	0.83	0.51*	0.05	0.23	0.41*

Open Research Section

We have archived the outputs from the two MITgcm simulations at doi:10.5281/zenodo.8350601. To make file sizes manageable, the outputs have been subset to once per day and the region north of 65.4°N. We are working to make the observational data stored on a public archive and will have this statement revised before publication. We are also working to make code available to reproduce figures from this paper.

Acknowledgments

We acknowledge Margaret Lindeman, Sarah Giddings, and Rebecca Jackson for helpful discussions and suggestions. We thank An Ngyuen for providing ASTE data. RS and FS acknowledge funding from the Heising Simons Foundation.

References

- Adcroft, A., Hill, C., Campin, J.-M., Marshall, J., & Heimbach, P. (2004). Overview of the formulation and numerics of the MIT GCM. In *Proceedings of the ecmwf seminar series on numerical methods, recent developments in numerical methods for atmosphere and ocean modelling* (pp. 139–149).
- Andresen, C. S., Schmidt, S., Seidenkrantz, M.-S., Straneo, F., Grycel, A., Hass, C. H., ... Kuijpers, A. (2014, August). A 100-year record of changes in water renewal rate in Sermilik fjord and its influence on calving of Helheim glacier, southeast Greenland. *Continental Shelf Research*, *85*, 21–29. doi: 10.1016/j.csr.2014.05.017
- Andresen, C. S., Straneo, F., Ribergaard, M. H., Bjørk, A. A., Andersen, T. J., Kuijpers, A., ... Ahlstrøm, A. P. (2012, January). Rapid response of Helheim Glacier in Greenland to climate variability over the past century. *Nature Geoscience*, *5*(1), 37–41. Retrieved 2022-12-19, from <https://www.nature.com/articles/ngeo1349> (Number: 1 Publisher: Nature Publishing Group) doi: 10.1038/ngeo1349
- Aure, J., Molvær, J., & Stigebrandt, A. (1996). Observations of inshore water exchange forced by a fluctuating offshore density field. *Journal of Geophysical Research*, *33*(1), 112–119. doi: 10.1016/S0025-326X(97)00005-2
- Beaird, N., Straneo, F., & Jenkins, W. (2018). Export of Strongly Diluted Greenland Meltwater From a Major Glacial Fjord. *Geophys. Res. Lett.*, *45*, 4163–4170. doi: 10.1029/2018GL077000
- Burchard, H., Bolding, K., Feistel, R., Gräwe, U., Klingbeil, K., MacCready, P., ... van der Lee, E. M. (2018, July). The Knudsen theorem and the Total Exchange Flow analysis framework applied to the Baltic Sea. *Progress in Oceanography*, *165*, 268–286. Retrieved 2022-02-23, from <https://www.sciencedirect.com/science/article/pii/S0079661117303774> doi: 10.1016/j.pocean.2018.04.004
- Carroll, D., Sutherland, D. A., Curry, B., Nash, J. D., Shroyer, E. L., Catania, G. A., ... Steur, L. d. (2018). Subannual and Seasonal Variability of Atlantic-Origin Waters in Two Adjacent West Greenland Fjords. *J. Geophys. Res. Oceans*, *123*, 6670–6687. doi: 10.1029/2018JC014278
- Carroll, D., Sutherland, D. A., Shroyer, E. L., Nash, J. D., Catania, G. A., & Stearns, L. A. (2015). Modeling Turbulent Subglacial Meltwater Plumes: Implications for Fjord-Scale Buoyancy-Driven Circulation. *J. Phys. Oceanogr.*, *45*, 2169–2185. doi: 10.1175/JPO-D-15-0033.1
- Carroll, D., Sutherland, D. A., Shroyer, E. L., Nash, J. D., Catania, G. A., & Stearns, L. A. (2017). Subglacial discharge-driven renewal of tidewater glacier fjords. *J. Geophys. Res. Oceans*, *122*, 6611–6629. doi: 10.1002/2017JC012962
- Christoffersen, P., Mugford, R. I., Heywood, K. J., Joughin, I., Dowdeswell, J. A., Syvitski, J. P. M., ... Benham, T. J. (2011, September). Warming of waters

- 779 in an East Greenland fjord prior to glacier retreat: mechanisms and connec-
 780 tion to large-scale atmospheric conditions. *The Cryosphere*, 5(3), 701–714.
 781 Retrieved 2020-01-30, from <https://www.the-cryosphere.net/5/701/2011/>
 782 doi: <https://doi.org/10.5194/tc-5-701-2011>
- 783 Cowton, T., Slater, D., Sole, A., Goldberg, D., & Nienow, P. (2015). Modeling the
 784 impact of glacial runoff on fjord circulation and submarine melt rate using a
 785 new subgrid-scale parameterization for glacial plumes. , 120(2), 796–812. doi:
 786 10.1002/2014JC010324
- 787 Cowton, T. R., Sole, A. J., Nienow, P. W., Slater, D. A., & Christoffersen, P.
 788 (2018, July). Linear response of east Greenland’s tidewater glaciers to
 789 ocean/atmosphere warming. *Proceedings of the National Academy of Sci-*
 790 *ences*, 115(31), 7907–7912. (Publisher: Proceedings of the National Academy
 791 of Sciences) doi: 10.1073/pnas.1801769115
- 792 Davison, B. J., Cowton, T. R., Cottier, F. R., & Sole, A. J. (2020, Novem-
 793 ber). Iceberg melting substantially modifies oceanic heat flux towards
 794 a major Greenlandic tidewater glacier. *Nat. Commun.*, 11, 5983. doi:
 795 10.1038/s41467-020-19805-7
- 796 Emery, W. J., & Thomson, R. E. (2001). *Data analysis methods in physical oceanog-*
 797 *raphy (revised second edition)* (Revised Second Edition ed.). Amsterdam: Else-
 798 vier Science. doi: <https://doi.org/10.1016/B978-044450756-3/50007-1>
- 799 Enderlin, E. M., Howat, I. M., Jeong, S., Noh, M.-J., Angelen, J. H. v., & Broeke,
 800 M. R. v. d. (2014). An improved mass budget for the Greenland ice sheet.
 801 *Geophys. Res. Lett.*, 41, 866–872. doi: 10.1002/2013GL059010
- 802 Ezhova, E., Cenedese, C., & Brandt, L. (2017, October). Dynamics of a Turbu-
 803 lent Buoyant Plume in a Stratified Fluid: An Idealized Model of Subglacial
 804 Discharge in Greenland Fjords. *J. Phys. Oceanogr.*, 47, 2611–2630. doi:
 805 10.1175/JPO-D-16-0259.1
- 806 Fraser, N. J., & Inall, M. E. (2018). Influence of barrier wind forcing on heat deliv-
 807 ery toward the Greenland ice sheet. *J. Geophys. Res. Oceans*, 123, 2513–2538.
 808 doi: 10.1002/2017JC013464
- 809 Fraser, N. J., Inall, M. E., Magaldi, M. G., Haine, T. W. N., & Jones, S. C. (2018).
 810 Wintertime fjord-shelf interaction and ice sheet melting in southeast greenland.
 811 , 123(12), 9156–9177. doi: 10.1029/2018JC014435
- 812 Gelderloos, R., Haine, T. W. N., & Almansi, M. (2021, March). Coastal Trapped
 813 Waves and Other Subinertial Variability along the Southeast Greenland Coast
 814 in a Realistic Numerical Simulation. *Journal of Physical Oceanography*, 51(3),
 815 861–877. Retrieved 2022-02-28, from [https://journals.ametsoc.org/
 816 view/journals/phoc/51/3/JPO-D-20-0239.1.xml](https://journals.ametsoc.org/view/journals/phoc/51/3/JPO-D-20-0239.1.xml) (Publisher: Ameri-
 817 can Meteorological Society Section: Journal of Physical Oceanography) doi:
 818 10.1175/JPO-D-20-0239.1
- 819 Gelderloos, R., Haine, T. W. N., & Almansi, M. (2022). Subinertial
 820 Variability in Four Southeast Greenland Fjords in Realistic Nu-
 821 merical Simulations. *Journal of Geophysical Research: Oceans*,
 822 127(11), e2022JC018820. Retrieved 2023-01-13, from [https://
 823 onlinelibrary.wiley.com/doi/abs/10.1029/2022JC018820](https://onlinelibrary.wiley.com/doi/abs/10.1029/2022JC018820) (eprint:
 824 <https://onlinelibrary.wiley.com/doi/pdf/10.1029/2022JC018820>) doi:
 825 10.1029/2022JC018820
- 826 Gelderloos, R., Haine, T. W. N., Koszalka, I. M., & Magaldi, M. G. (2017, July).
 827 Seasonal Variability in Warm-Water Inflow toward Kangerdlugssuaq Fjord.
 828 *Journal of Physical Oceanography*, 47(7), 1685–1699. Retrieved 2023-01-
 829 13, from [https://journals.ametsoc.org/view/journals/phoc/47/7/
 830 jpo-d-16-0202.1.xml](https://journals.ametsoc.org/view/journals/phoc/47/7/jpo-d-16-0202.1.xml) (Publisher: American Meteorological Society Sec-
 831 tion: Journal of Physical Oceanography) doi: 10.1175/JPO-D-16-0202.1
- 832 Gladish, C. V., Holland, D. M., & Lee, C. M. (2014). Oceanic boundary condi-
 833 tions for jakobshavn glacier. part II: Provenance and sources of variability

- 834 of disko bay and ilulissat icefjord waters, 1990–2011. , *45*(1), 33–63. doi:
835 10.1175/JPO-D-14-0045.1
- 836 Gladish, C. V., Holland, D. M., Rosing-Asvid, A., Behrens, J. W., & Boje, J. (2014).
837 Oceanic boundary conditions for Jakobshavn Glacier. Part I: Variability and
838 renewal of Ilulissat Icefjord Waters, 2001–14. *J. Phys. Oceanogr.*, *45*, 3–32.
839 doi: 10.1175/JPO-D-14-0044.1
- 840 Griffies, S. M., & Hallberg, R. W. (2000, August). Biharmonic Friction with a
841 Smagorinsky-Like Viscosity for Use in Large-Scale Eddy-Permitting Ocean
842 Models. *Monthly Weather Review*, *128*(8), 2935–2946. Retrieved 2023-
843 08-30, from [https://journals.ametsoc.org/view/journals/mwre/128/
844 8/1520-0493_2000_128_2935_bfwas1.2.0.co_2.xml](https://journals.ametsoc.org/view/journals/mwre/128/8/1520-0493_2000_128_2935_bfwas1.2.0.co_2.xml) (Publisher: Amer-
845 ican Meteorological Society Section: Monthly Weather Review) doi:
846 10.1175/1520-0493(2000)128(2935:BFWASL)2.0.CO;2
- 847 Hager, A. O., Sutherland, D. A., Amundson, J. M., Jackson, R. H., Kienholz, C.,
848 Motyka, R. J., & Nash, J. D. (2022). Subglacial discharge reflux and buoyancy
849 forcing drive seasonality in a silled glacial fjord. *J. Geophys. Res. Oceans*, *127*.
850 doi: 10.1029/2021JC018355
- 851 Harden, B. E., Renfrew, I. A., & Petersen, G. N. (2011). A climatology of winter-
852 time barrier winds off southeast greenland. , *24*(17), 4701–4717. doi: 10.1175/
853 2011JCLI4113.1
- 854 Harden, B. E., Straneo, F., & Sutherland, D. A. (2014). Moored observations of syn-
855 optic and seasonal variability in the East Greenland Coastal Current. *J. Geo-
856 phys. Res. Oceans*, *119*, 8838–8857. doi: 10.1002/2014JC010134
- 857 Hersbach, H., Bell, B., Berrisford, P., Hirahara, S., Horányi, A., Muñoz-Sabater, J.,
858 ... Thépaut, J.-N. (2020). The ERA5 global reanalysis. *Q. J. R. Meteorol.
859 Soc.*, *146*, 1999–2049. doi: 10.1002/qj.3803
- 860 Holland, D. M., Thomas, R. H., de Young, B., Ribergaard, M. H., & Lyberth, B.
861 (2008, October). Acceleration of Jakobshavn Isbræ triggered by warm subsur-
862 face ocean waters. *Nat. Geosci.*, *1*, 659–664. doi: 10.1038/ngeo316
- 863 Hopwood, M. J., Carroll, D., Dunse, T., Hodson, A., Holding, J. M., Iriarte, J. L.,
864 ... Meire, L. (2020, April). Review article: How does glacier discharge affect
865 marine biogeochemistry and primary production in the Arctic? *Cryosphere*,
866 *14*, 1347–1383. doi: 10.5194/tc-14-1347-2020
- 867 Howat, I. M., Joughin, I., Tulaczyk, S., & Gogineni, S. (2005). Rapid re-
868 treat and acceleration of Helheim Glacier, east Greenland. *Geophys-
869 ical Research Letters*, *32*(22). Retrieved 2023-01-13, from [https://
870 onlinelibrary.wiley.com/doi/abs/10.1029/2005GL024737](https://onlinelibrary.wiley.com/doi/abs/10.1029/2005GL024737) (eprint:
871 <https://onlinelibrary.wiley.com/doi/pdf/10.1029/2005GL024737>) doi:
872 10.1029/2005GL024737
- 873 Hughes, K. G. (2022). Pathways, Form Drag, and Turbulence in Sim-
874 ulations of an Ocean Flowing Through an Ice Mélange. *Journal of
875 Geophysical Research: Oceans*, *127*(6), e2021JC018228. (eprint:
876 <https://onlinelibrary.wiley.com/doi/pdf/10.1029/2021JC018228>) doi:
877 10.1029/2021JC018228
- 878 Hughes, K. G., Klymak, J. M., Williams, W. J., & Melling, H. (2018). Tidally Mod-
879 ulated Internal Hydraulic Flow and Energetics in the Central Canadian Arctic
880 Archipelago. *Journal of Geophysical Research: Oceans*, *123*(8), 5210–5229.
881 doi: <https://doi.org/10.1029/2018JC013770>
- 882 Inall, M. E., Nilsen, F., Cottier, F. R., & Daae, R. (2015). Shelf/fjord exchange
883 driven by coastal-trapped waves in the arctic. , *120*(12), 8283–8303. doi:
884 10.1002/2015JC011277
- 885 Jackett, D. R., & McDougall, T. J. (1995). Minimal Adjustment of Hydrographic
886 Profiles to Achieve Static Stability. *Journal of Atmospheric and Oceanic Tech-
887 nology*, *12*(2), 381–389. doi: 10.1175/1520-0426(1995)012<0381:MAOHT>2.0
888 .CO;2

- 889 Jackson, R. H., Lentz, S. J., & Straneo, F. (2018). The Dynamics of Shelf Forcing in
890 Greenlandic Fjords. *J. Phys. Oceanogr.*, *48*, 2799–2827. doi: 10.1175/JPO-D
891 -18-0057.1
- 892 Jackson, R. H., Motyka, R. J., Amundson, J. M., Abib, N., Sutherland, D. A., Nash,
893 J. D., & Kienholz, C. (2022). The relationship between submarine melt and
894 subglacial discharge from observations at a tidewater glacier. *J. Geophys. Res.*
895 *Oceans*, *127*, e2021JC018204. doi: 10.1029/2021JC018204
- 896 Jackson, R. H., Nash, J. D., Kienholz, C., Sutherland, D. A., Amundson, J. M.,
897 ka, R. J., . . . Pettit, E. C. (2020). Meltwater intrusions reveal mechanisms
898 for rapid submarine melt at a tidewater glacier. *Geophys. Res. Lett.*, *47*,
899 e2019GL085335. doi: 10.1029/2019GL085335
- 900 Jackson, R. H., & Straneo, F. (2016). Heat, Salt, and Freshwater Budgets for a
901 Glacial Fjord in Greenland. *J. Phys. Oceanogr.*, *46*, 2735–2768. doi: 10.1175/
902 JPO-D-15-0134.1
- 903 Jackson, R. H., Straneo, F., & Sutherland, D. A. (2014). Externally forced fluctua-
904 tions in ocean temperature at Greenland glaciers in non-summer months. *Nat.*
905 *Geosci.*, *7*, 503–508. doi: 10.1038/ngeo2186
- 906 Jenkins, A. (2011). Convection-Driven Melting near the Grounding Lines of Ice
907 Shelves and Tidewater Glaciers. *J. Phys. Oceanogr.*, *41*, 2279–2294. doi: 10
908 .1175/JPO-D-11-03.1
- 909 Kajanto, K., Straneo, F., & Nisancioglu, K. (2023, January). Impact of icebergs on
910 the seasonal submarine melt of Sermeq Kujalleq. *The Cryosphere*, *17*(1), 371–
911 390. Retrieved 2023-09-15, from [https://tc.copernicus.org/articles/17/
912 371/2023/](https://tc.copernicus.org/articles/17/371/2023/) (Publisher: Copernicus GmbH) doi: 10.5194/tc-17-371-2023
- 913 Khazendar, A., Fenty, I. G., Carroll, D., Gardner, A., Lee, C. M., Fukumori, I., . . .
914 Willis, J. (2019). Interruption of two decades of Jakobshavn Isbrae accelera-
915 tion and thinning as regional ocean cools. *Nat. Geosci.*, *12*, 277–283. doi:
916 10.1038/s41561-019-0329-3
- 917 Kimura, S., Holland, P. R., Jenkins, A., & Piggott, M. (2014, December). The
918 Effect of Meltwater Plumes on the Melting of a Vertical Glacier Face. *Jour-
919 nal of Physical Oceanography*, *44*(12), 3099–3117. Retrieved 2023-01-
920 13, from [https://journals.ametsoc.org/view/journals/phoc/44/12/
921 jpo-d-13-0219.1.xml](https://journals.ametsoc.org/view/journals/phoc/44/12/jpo-d-13-0219.1.xml) (Publisher: American Meteorological Society Section:
922 Journal of Physical Oceanography) doi: 10.1175/JPO-D-13-0219.1
- 923 Klinck, J. M., O’Brien, J. J., & Svendsen, H. (1981, December). A Simple Model
924 of Fjord and Coastal Circulation Interaction. *Journal of Physical Oceanogra-
925 phy*, *11*(12), 1612–1626. (Publisher: American Meteorological Society Section:
926 Journal of Physical Oceanography) doi: 10.1175/1520-0485(1981)011<1612:
927 ASMOFA>2.0.CO;2
- 928 Large, W. G., McWilliams, J. C., & Doney, S. C. (1994). Oceanic vertical mixing:
929 A review and a model with a nonlocal boundary layer parameterization. *Rev.*
930 *Geophys.*, *32*, 363–403. doi: 10.1029/94RG01872
- 931 Lindeman, M. R., Straneo, F., Wilson, N. J., Toole, J. M., Krishfield, R. A., Beard,
932 N. L., . . . Schaffer, J. (2020). Ocean Circulation and Variability Beneath
933 Nioghalvfjærdsbræ (79 North Glacier) Ice Tongue. *J. Geophys. Res. Oceans*,
934 *125*, e2020JC016091. doi: 10.1029/2020JC016091
- 935 Liu, Y., MacCready, P., Hickey, B. M., Dever, E. P., Kosro, P. M., & Ba-
936 nas, N. S. (2009). Evaluation of a coastal ocean circulation model
937 for the Columbia River plume in summer 2004. *Journal of Geophysical*
938 *Research: Oceans*, *114*(C2). Retrieved 2022-11-18, from [https://
939 onlinelibrary.wiley.com/doi/abs/10.1029/2008JC004929](https://onlinelibrary.wiley.com/doi/abs/10.1029/2008JC004929) (eprint:
940 <https://onlinelibrary.wiley.com/doi/pdf/10.1029/2008JC004929>) doi:
941 10.1029/2008JC004929
- 942 Lorenz, M., Klingbeil, K., & Burchard, H. (2020). Numerical Study
943 of the Exchange Flow of the Persian Gulf Using an Extended

- 944 Total Exchange Flow Analysis Framework. *Journal of Geo-*
 945 *physical Research: Oceans*, 125(2), e2019JC015527. (.eprint:
 946 <https://agupubs.onlinelibrary.wiley.com/doi/pdf/10.1029/2019JC015527>)
 947 doi: 10.1029/2019JC015527
- 948 Lorenz, M., Klingbeil, K., MacCready, P., & Burchard, H. (2019, May). Numerical
 949 issues of the Total Exchange Flow (TEF) analysis framework for quantifying
 950 estuarine circulation. *Ocean Science*, 15(3), 601–614. Retrieved 2022-10-18,
 951 from <https://os.copernicus.org/articles/15/601/2019/> (Publisher:
 952 Copernicus GmbH) doi: 10.5194/os-15-601-2019
- 953 Luckman, A., Murray, T., de Lange, R., & Hanna, E. (2006). Rapid
 954 and synchronous ice-dynamic changes in East Greenland. *Geophys-*
 955 *ical Research Letters*, 33(3). Retrieved 2023-01-13, from [https://](https://onlinelibrary.wiley.com/doi/abs/10.1029/2005GL025428)
 956 onlinelibrary.wiley.com/doi/abs/10.1029/2005GL025428 (.eprint:
 957 <https://onlinelibrary.wiley.com/doi/pdf/10.1029/2005GL025428>) doi:
 958 10.1029/2005GL025428
- 959 MacCready, P. (2011, June). Calculating Estuarine Exchange Flow Using Isohaline
 960 Coordinates. *Journal of Physical Oceanography*, 41(6), 1116–1124. Retrieved
 961 2023-01-14, from [https://journals.ametsoc.org/view/journals/phoc/41/](https://journals.ametsoc.org/view/journals/phoc/41/6/2011jpo4517.1.xml)
 962 [6/2011jpo4517.1.xml](https://journals.ametsoc.org/view/journals/phoc/41/6/2011jpo4517.1.xml) (Publisher: American Meteorological Society Section:
 963 Journal of Physical Oceanography) doi: 10.1175/2011JPO4517.1
- 964 MacCready, P., & Geyer, W. R. (2010). Advances in Estuarine Physics. *Annu. Rev.*
 965 *Mar. Sci.*, 2, 35–58. doi: 10.1146/annurev-marine-120308-081015
- 966 MacCready, P., Geyer, W. R., & Burchard, H. (2018, June). Estuarine Ex-
 967 change Flow Is Related to Mixing through the Salinity Variance Budget.
 968 *Journal of Physical Oceanography*, 48(6), 1375–1384. Retrieved 2023-01-
 969 14, from [https://journals.ametsoc.org/view/journals/phoc/48/6/](https://journals.ametsoc.org/view/journals/phoc/48/6/jpo-d-17-0266.1.xml)
 970 [jpo-d-17-0266.1.xml](https://journals.ametsoc.org/view/journals/phoc/48/6/jpo-d-17-0266.1.xml) (Publisher: American Meteorological Society Sec-
 971 tion: Journal of Physical Oceanography) doi: 10.1175/JPO-D-17-0266.1
- 972 Mankoff, K. D., Solgaard, A., Colgan, W., Ahlstrøm, A. P., Khan, S. A., & Fausto,
 973 R. S. (2020, June). Greenland Ice Sheet solid ice discharge from 1986 through
 974 March 2020. *Earth System Science Data*, 12(2), 1367–1383. Retrieved 2023-
 975 01-13, from <https://essd.copernicus.org/articles/12/1367/2020/> (Pub-
 976 lisher: Copernicus GmbH) doi: 10.5194/essd-12-1367-2020
- 977 Mankoff, K. D., Straneo, F., Cenedese, C., Das, S. B., Richards, C. G., & Singh,
 978 H. (2016). Structure and dynamics of a subglacial discharge plume in
 979 a greenlandic fjord. *J. Geophys. Res.: Oceans*, 121, 8670–8688. doi:
 980 10.1002/2016JC011764
- 981 Marshall, J., Adcroft, A., Hill, C., Perelman, L., & Heisey, C. (1997). A finite-
 982 volume, incompressible Navier Stokes model for studies of the ocean on parallel
 983 computers. *J. Geophys. Res.*, 102, 5753–5766. doi: 10.1029/96JC02775
- 984 Moffat, C. (2014). Wind-driven modulation of warm water supply to a proglacial
 985 fjord, jorge montt glacier, patagonia. , 41(11), 3943–3950. doi: 10.1002/
 986 2014GL060071
- 987 Moon, T., Sutherland, D. A., Carroll, D., Felikson, D., Kehrl, L., & Straneo, F.
 988 (2018, January). Subsurface iceberg melt key to Greenland fjord freshwater
 989 budget. *Nat. Geosci.*, 11, 49–54. doi: 10.1038/s41561-017-0018-z
- 990 Morlighem, M., Williams, C. N., Rignot, E., An, L., Arndt, J. E., Bamber, J. L.,
 991 ... Zinglensen, K. B. (2017). BedMachine v3: Complete bed topography
 992 and ocean bathymetry mapping of Greenland from multibeam echo sounding
 993 combined with mass conservation. *Geophys. Res. Lett.*, 44, 11051–11061. doi:
 994 10.1002/2017GL074954
- 995 Mortensen, J., Bendtsen, J., Lennert, K., & Rysgaard, S. (2014). Seasonal variabil-
 996 ity of the circulation system in a west Greenland tidewater outlet glacier fjord,
 997 Godthåbsfjord (64°N). *J. Geophys. Res. Earth Surf.*, 119, 2591–2603. doi:
 998 10.1002/2014JF003267

- 999 Mortensen, J., Lennert, K., Bendtsen, J., & Rysgaard, S. (2011). Heat sources for
1000 glacial melt in a sub-arctic fjord (godthåbsfjord) in contact with the greenland
1001 ice sheet. , *116*. doi: 10.1029/2010JC006528
- 1002 Mortensen, J., Rysgaard, S., Arendt, K. E., Juul-Pedersen, T., Søgaard, D. H.,
1003 Bendtsen, J., & Meire, L. (2018). Local Coastal Water Masses Control Heat
1004 Levels in a West Greenland Tidewater Outlet Glacier Fjord. *J. Geophys. Res.*
1005 *Oceans*, *123*. doi: 10.1029/2018JC014549
- 1006 Mougnot, J., Rignot, E., Bjørk, A. A., van den Broeke, M., Millan, R., Morlighem,
1007 M., ... Wood, M. (2019). Forty-six years of Greenland Ice Sheet mass
1008 balance from 1972 to 2018. *Proc. Natl. Acad. Sci.*, *116*, 9239-44. doi:
1009 <https://doi.org/10.1073/pnas.1904242116>
- 1010 Muilwijk, M., Straneo, F., Slater, D. A., Smedsrud, L. H., Holte, J., Wood, M.,
1011 ... Harden, B. (2022, March). Export of Ice Sheet Meltwater from Uper-
1012 navik Fjord, West Greenland. *J. Phys. Oceanogr.*, *52*, 363–382. doi:
1013 10.1175/JPO-D-21-0084.1
- 1014 Murphy, A. H. (1988, December). Skill Scores Based on the Mean Square Error and
1015 Their Relationships to the Correlation Coefficient. *Monthly Weather Review*,
1016 *116*(12), 2417–2424. Retrieved 2023-09-06, from https://journals.ametsoc.org/view/journals/mwre/116/12/1520-0493_1988_116_2417_ssbotm_2_0_co_2.xml (Publisher: American Meteorological Society Section: Monthly
1017 Weather Review) doi: 10.1175/1520-0493(1988)116(2417:SSBOTM)2.0.CO;2
- 1018
1019
1020 Nguyen, A. T., Pillar, H., Ocaña, V., Bigdeli, A., Smith, T. A., & Heimbach, P.
1021 (2021). The Arctic Subpolar Gyre sTate Estimate: Description and as-
1022 sessment of a data-constrained, dynamically consistent ocean-sea ice esti-
1023 mate for 2002–2017. *J. Adv. Model. Earth Syst.*, *13*, e2020MS002398. doi:
1024 10.1029/2020MS002398
- 1025 Ralston, D. K., Geyer, W. R., & Lerczak, J. A. (2010). Structure, variabil-
1026 ity, and salt flux in a strongly forced salt wedge estuary. *Journal of*
1027 *Geophysical Research: Oceans*, *115*(C6). Retrieved 2023-08-24, from
1028 <https://onlinelibrary.wiley.com/doi/abs/10.1029/2009JC005806>
1029 (eprint: <https://onlinelibrary.wiley.com/doi/pdf/10.1029/2009JC005806>)
1030 doi: 10.1029/2009JC005806
- 1031 Rysgaard, S., Vang, T., Stjernholm, M., Rasmussen, B., Windelin, A., & Ki-
1032 ilsholm, S. (2003, August). Physical Conditions, Carbon Transport,
1033 and Climate Change Impacts in a Northeast Greenland Fjord. *Arctic,*
1034 *Antarctic, and Alpine Research*, *35*(3), 301–312. (Publisher: Taylor &
1035 Francis eprint: [https://www.tandfonline.com/doi/pdf/10.1657/1523-
1036 0430%282003%29035%5B0301%3APCCTAC%5D2.0.CO%3B2](https://www.tandfonline.com/doi/pdf/10.1657/1523-0430%282003%29035%5B0301%3APCCTAC%5D2.0.CO%3B2)) doi:
1037 10.1657/1523-0430(2003)035[0301:PCCTAC]2.0.CO;2
- 1038 Sanchez, R., Slater, D., & Straneo, F. (2023). Delayed Freshwater Export from a
1039 Greenland tidewater glacial fjord. *Journal of Physical Oceanography*, *-1*(aop).
1040 doi: 10.1175/JPO-D-22-0137.1
- 1041 Sanchez, R., Straneo, F., & Andres, M. (2021, September). Using Acoustic
1042 Travel Time to Monitor the Heat Variability of Glacial Fjords. *Journal*
1043 *of Atmospheric and Oceanic Technology*, *38*(9), 1535–1550. Retrieved
1044 2022-02-15, from [https://journals.ametsoc.org/view/journals/atot/
1045 38/9/JTECH-D-20-0176.1.xml](https://journals.ametsoc.org/view/journals/atot/38/9/JTECH-D-20-0176.1.xml) (Publisher: American Meteorological
1046 Society Section: Journal of Atmospheric and Oceanic Technology) doi:
1047 10.1175/JTECH-D-20-0176.1
- 1048 Schaffer, J., Kanzow, T., von Appen, W.-J., von Albedyll, L., Arndt, J. E., &
1049 Roberts, D. H. (2020). Bathymetry constrains ocean heat supply to green-
1050 land's largest glacier tongue. , *13*(3), 227–231. doi: 10.1038/s41561-019-0529
1051 -x
- 1052 Schulz, K., Nguyen, A. T., & Pillar, H. R. (2022). An improved and observationally-
1053 constrained melt rate parameterization for vertical ice fronts of marine

- 1054 terminating glaciers. *Geophys. Res. Lett.*, *49*, e2022GL100654. doi:
 1055 10.1029/2022GL100654
- 1056 Sciascia, R., Straneo, F., Cenedese, C., & Heimbach, P. (2013). Seasonal variability
 1057 of submarine melt rate and circulation in an East Greenland fjord. *J. Geophys.*
 1058 *Res. Oceans*, *118*, 2492-2506. doi: 10.1002/jgrc.20142
- 1059 Shroyer, E. L., Padman, L., Samelson, R. M., Münchow, A., & Stearns, L. A. (2017,
 1060 April). Seasonal control of Petermann Gletscher ice-shelf melt by the ocean's
 1061 response to sea-ice cover in Nares Strait. *Journal of Glaciology*, *63*(238), 324–
 1062 330. (Publisher: Cambridge University Press) doi: 10.1017/jog.2016.140
- 1063 Slater, D. A., Carroll, D., Oliver, H., Hopwood, M. J., Straneo, F., Wood, M., ...
 1064 Morlighem, M. (2022). Characteristic depths, fluxes, and timescales for
 1065 Greenland's tidewater glacier fjords from subglacial discharge-driven up-
 1066 welling during summer. *Geophys. Res. Lett.*, *49*, e2021GL097081. doi:
 1067 10.1029/2021GL097081
- 1068 Slater, D. A., Felikson, D., Straneo, F., Goelzer, H., Little, C. M., Morlighem, M.,
 1069 ... Nowicki, S. (2020). Twenty-first century ocean forcing of the Greenland
 1070 ice sheet for modelling of sea level contribution. *The Cryosphere*, *14*, 985-1008.
 1071 doi: 10.5194/tc-14-985-2020
- 1072 Slater, D. A., & Straneo, F. (2022, October). Submarine melting of glaciers
 1073 in Greenland amplified by atmospheric warming. *Nature Geoscience*, 1–
 1074 6. Retrieved 2022-10-04, from [https://www.nature.com/articles/
 1075 s41561-022-01035-9](https://www.nature.com/articles/s41561-022-01035-9) (Publisher: Nature Publishing Group) doi:
 1076 10.1038/s41561-022-01035-9
- 1077 Slater, D. A., Straneo, F., Das, S. B., Richards, C. G., Wagner, T. J. W., & Nienow,
 1078 P. W. (2018). Localized plumes drive front-wide ocean melting of a green-
 1079 landic tidewater glacier. *Geophys. Res. Lett.*, *45*, 12,350–12,358. doi:
 1080 10.1029/2018GL080763
- 1081 Snow, T., Straneo, F., Holte, J., Grigsby, S., Abdalati, W., & Scambos, T.
 1082 (2021). More than Skin Deep: Sea Surface Temperature as a Means of In-
 1083 ferring Atlantic Water Variability on the Southeast Greenland Continen-
 1084 tal Shelf Near Helheim Glacier. *Journal of Geophysical Research: Oceans*,
 1085 *126*(4), e2020JC016509. Retrieved 2021-04-30, from [https://agupubs
 1086 .onlinelibrary.wiley.com/doi/abs/10.1029/2020JC016509](https://agupubs.onlinelibrary.wiley.com/doi/abs/10.1029/2020JC016509) (_eprint:
 1087 <https://agupubs.onlinelibrary.wiley.com/doi/pdf/10.1029/2020JC016509>) doi:
 1088 <https://doi.org/10.1029/2020JC016509>
- 1089 Snow, T., Zhang, W., Schreiber, E., Siegfried, M., Abdalati, W., & Scam-
 1090 bos, T. (n.d.). Alongshore winds force warm Atlantic Water toward
 1091 Helheim Glacier in southeast Greenland. *Journal of Geophysical Re-
 1092 search: Oceans*, *n/a*(n/a), e2023JC019953. Retrieved 2023-09-14, from
 1093 <https://onlinelibrary.wiley.com/doi/abs/10.1029/2023JC019953>
 1094 (_eprint: <https://onlinelibrary.wiley.com/doi/pdf/10.1029/2023JC019953>)
 1095 doi: 10.1029/2023JC019953
- 1096 Straneo, F., & Cenedese, C. (2015). The dynamics of greenland's glacial fjords and
 1097 their role in climate. *Annu. Rev. Mar. Sci.*, *7*, 89–112. doi: 10.1146/annurev-
 1098 -marine-010213-135133
- 1099 Straneo, F., Curry, R. G., Sutherland, D. A., Hamilton, G. S., Cenedese, C., Våge,
 1100 K., & Stearns, L. A. (2011). Impact of fjord dynamics and glacial runoff
 1101 on the circulation near Helheim Glacier. *Nat. Geosci.*, *4*, 322–327. doi:
 1102 10.1038/ngeo1109
- 1103 Straneo, F., Hamilton, G. S., Sutherland, D. A., Stearns, L. A., Davidson, F., Ham-
 1104 mill, M. O., ... Rosing-Asvid, A. (2010). Rapid circulation of warm subtropi-
 1105 cal waters in a major glacial fjord in east Greenland. *Nat. Geosci.*, *3*, 182–186.
 1106 doi: 10.1038/ngeo764
- 1107 Straneo, F., & Heimbach, P. (2013). North Atlantic warming and the retreat of
 1108 Greenland's outlet glaciers. *Nature*, *504*, 36–43. doi: 10.1038/nature12854

- 1109 Straneo, F., Sutherland, D. A., Stearns, L., Catania, G., Heimbach, P., Moon, T., . . .
 1110 Meire, L. (2019). The case for a sustained Greenland Ice Sheet-Ocean observ-
 1111 ing system (GrIOOS). *Front. Mar. Sci.*, *6*. doi: 10.3389/fmars.2019.00138
- 1112 Stuart-Lee, A. E., Mortensen, J., Kaaden, A.-S. v. d., & Meire, L. (2021). Sea-
 1113 sonal Hydrography of Ameralik: A Southwest Greenland Fjord Impacted by a
 1114 Land-Terminating Glacier. *J. Geophys. Res. Oceans*, *126*, e2021JC017552. doi:
 1115 10.1029/2021JC017552
- 1116 Sundfjord, A., Albrechtsen, J., Kasajima, Y., Skogseth, R., Kohler, J., Nuth, C.,
 1117 . . . Torsvik, T. (2017). Effects of glacier runoff and wind on surface
 1118 layer dynamics and Atlantic Water exchange in Kongsfjorden, Svalbard;
 1119 a model study. *Estuarine, Coastal and Shelf Science*, *187*, 260–272. doi:
 1120 10.1016/j.ecss.2017.01.015
- 1121 Sutherland, D. A., MacCready, P., Banas, N. S., & Smedstad, L. F. (2011, June).
 1122 A Model Study of the Salish Sea Estuarine Circulation. *Journal of Physi-
 1123 cal Oceanography*, *41*(6), 1125–1143. Retrieved 2023-09-06, from [https://
 1124 journals.ametsoc.org/view/journals/phoc/41/6/2011jpo4540.1.xml](https://journals.ametsoc.org/view/journals/phoc/41/6/2011jpo4540.1.xml)
 1125 (Publisher: American Meteorological Society Section: Journal of Physical
 1126 Oceanography) doi: 10.1175/2011JPO4540.1
- 1127 Sutherland, D. A., Straneo, F., Stenson, G. B., Davidson, F. J. M., Hammill, M. O.,
 1128 & Rosing-Asvid, A. (2013). Atlantic water variability on the SE greenland con-
 1129 tinental shelf and its relationship to SST and bathymetry. , *118*(2), 847–855.
 1130 doi: 10.1029/2012JC008354
- 1131 Wood, M., Rignot, E., Fenty, I., An, L., Bjørk, A., van den Broeke, M., . . . Zhang,
 1132 H. (2021). Ocean forcing drives glacier retreat in Greenland. *Sci. Adv.*, *7*,
 1133 eaba7282. doi: 10.1126/sciadv.aba7282
- 1134 Wood, M., Rignot, E., Fenty, I., Menemenlis, D., Millan, R., Morlighem,
 1135 M., . . . Seroussi, H. (2018). Ocean-Induced Melt Triggers Glacier
 1136 Retreat in Northwest Greenland. *Geophysical Research Letters*,
 1137 *45*(16), 8334–8342. Retrieved 2021-09-08, from [https://agupubs
 1138 .onlinelibrary.wiley.com/doi/abs/10.1029/2018GL078024](https://agupubs.onlinelibrary.wiley.com/doi/abs/10.1029/2018GL078024) (.eprint:
 1139 <https://agupubs.onlinelibrary.wiley.com/doi/pdf/10.1029/2018GL078024>) doi:
 1140 10.1029/2018GL078024
- 1141 Xu, Y., Rignot, E., Menemenlis, D., & Koppes, M. (2012). Numerical experiments
 1142 on subaqueous melting of Greenland tidewater glaciers in response to ocean
 1143 warming and enhanced subglacial discharge. *Ann. Glaciol.*, *53*, 229–234. doi:
 1144 10.3189/2012AoG60A139
- 1145 Zhao, K. X., Stewart, A. L., & McWilliams, J. C. (2021, April). Geometric Con-
 1146 straints on Glacial Fjord–Shelf Exchange. *J. Phys. Oceanogr.*, *51*, 1223–1246.
 1147 doi: 10.1175/JPO-D-20-0091.1
- 1148 Zhao, K. X., Stewart, A. L., & McWilliams, J. C. (2022). Linking Overturning, Re-
 1149 circulation, and Melt in Glacial Fjords. *Geophys. Res. Lett.*, *49*. doi: 10.1029/
 1150 2021GL095706
- 1151 Zhao, K. X., Stewart, A. L., McWilliams, J. C., Fenty, I. G., & Rignot, E. J. (2022,
 1152 November). Standing Eddies in Glacial Fjords and their Role in Fjord Cir-
 1153 culation and Melt. *Journal of Physical Oceanography*, -1(aop). Retrieved
 1154 2023-01-13, from [https://journals.ametsoc.org/view/journals/phoc/
 1155 aop/JPO-D-22-0085.1/JPO-D-22-0085.1.xml](https://journals.ametsoc.org/view/journals/phoc/aop/JPO-D-22-0085.1/JPO-D-22-0085.1.xml) (Publisher: American
 1156 Meteorological Society Section: Journal of Physical Oceanography) doi:
 1157 10.1175/JPO-D-22-0085.1

Figure 1.

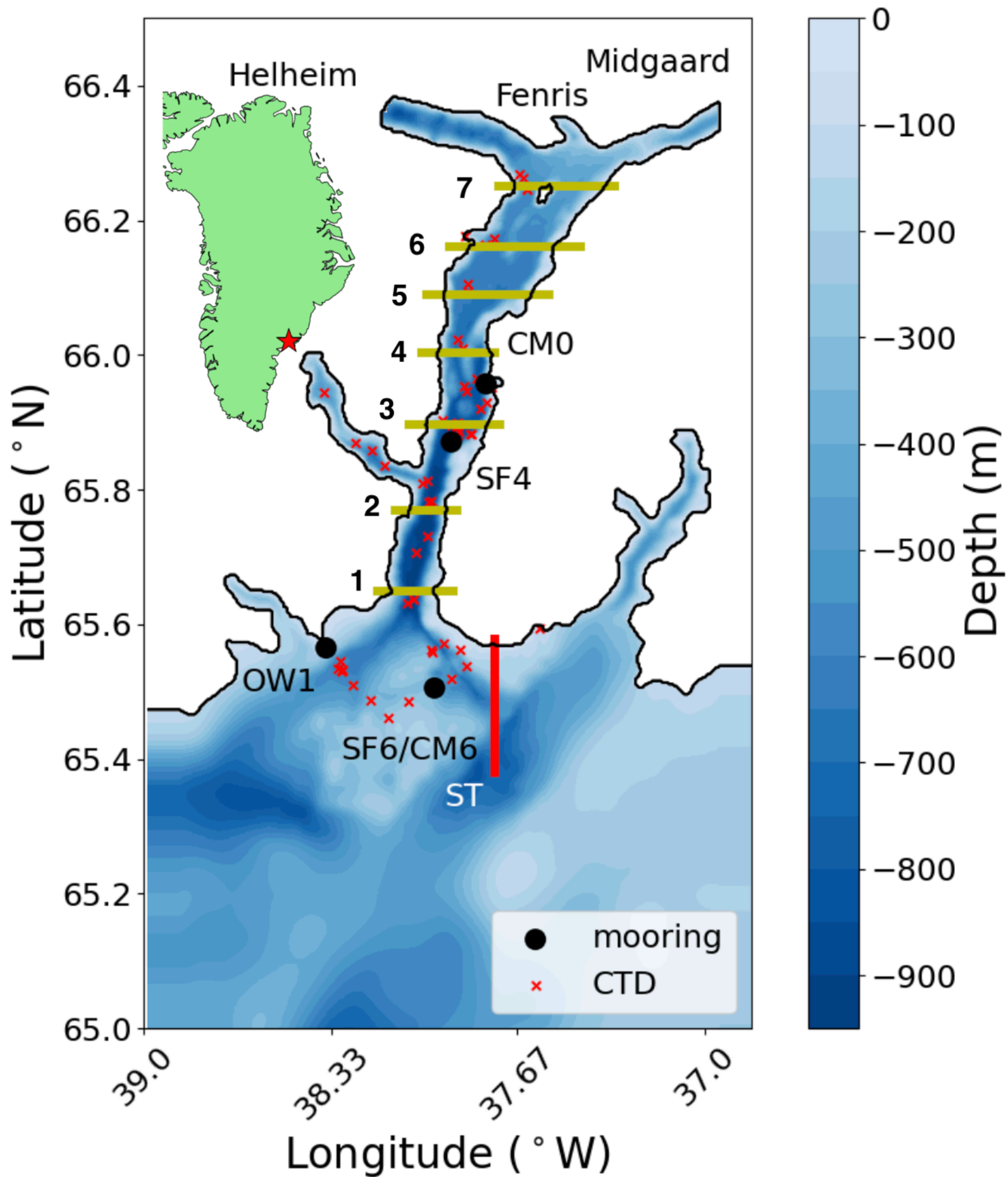


Figure 2.

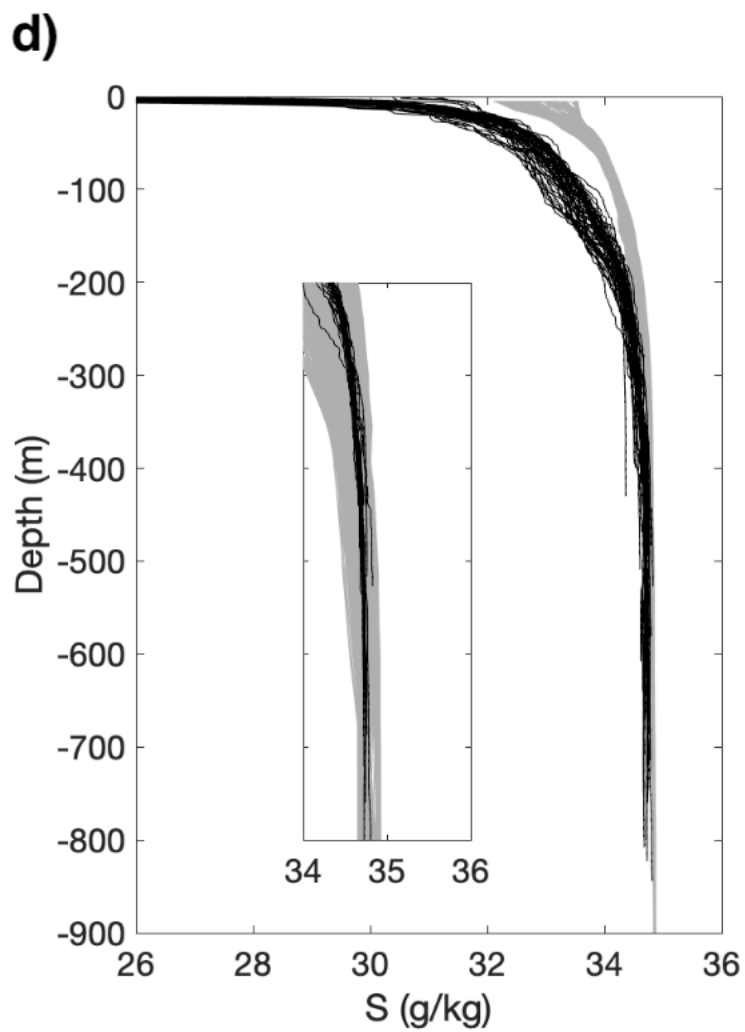
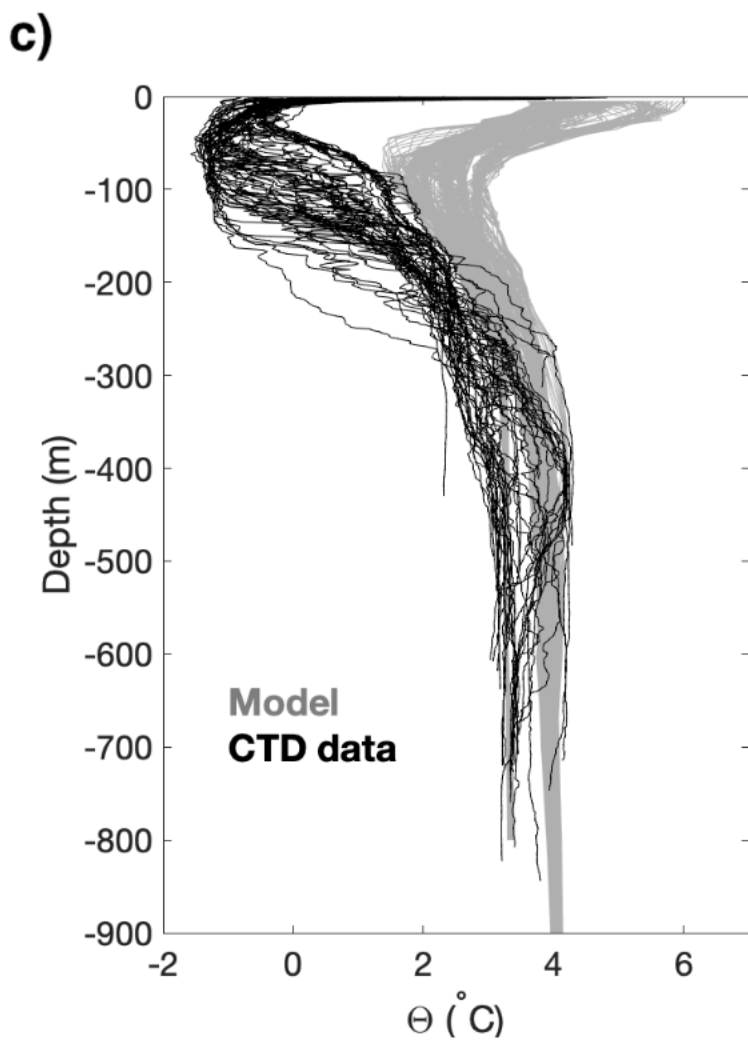
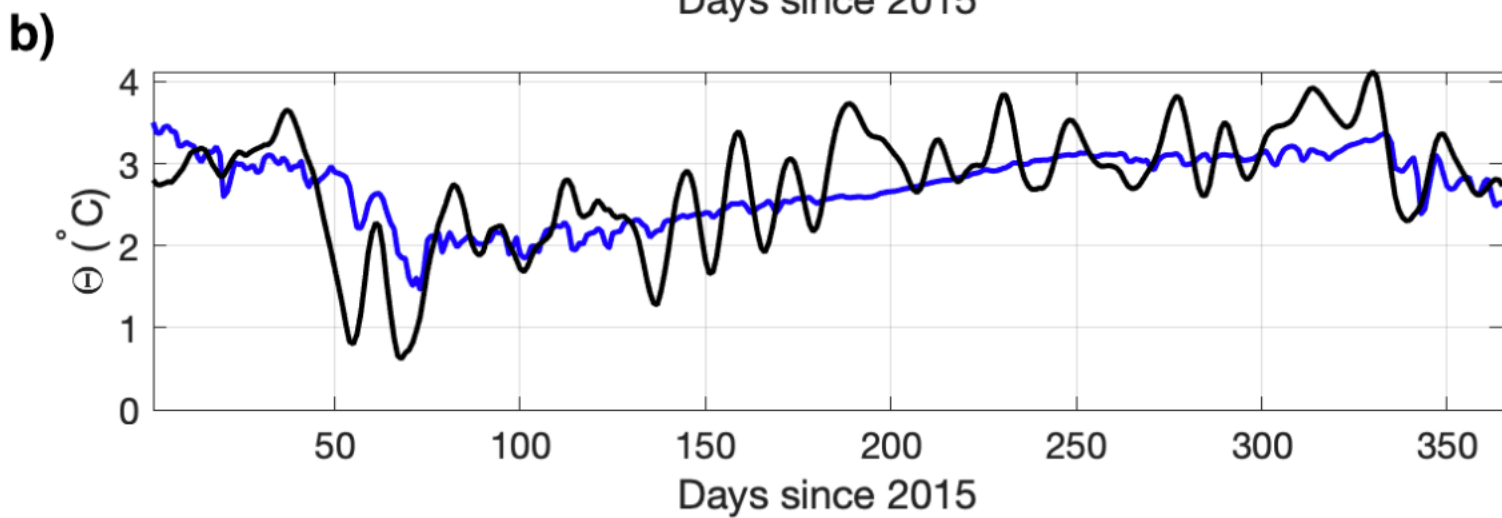
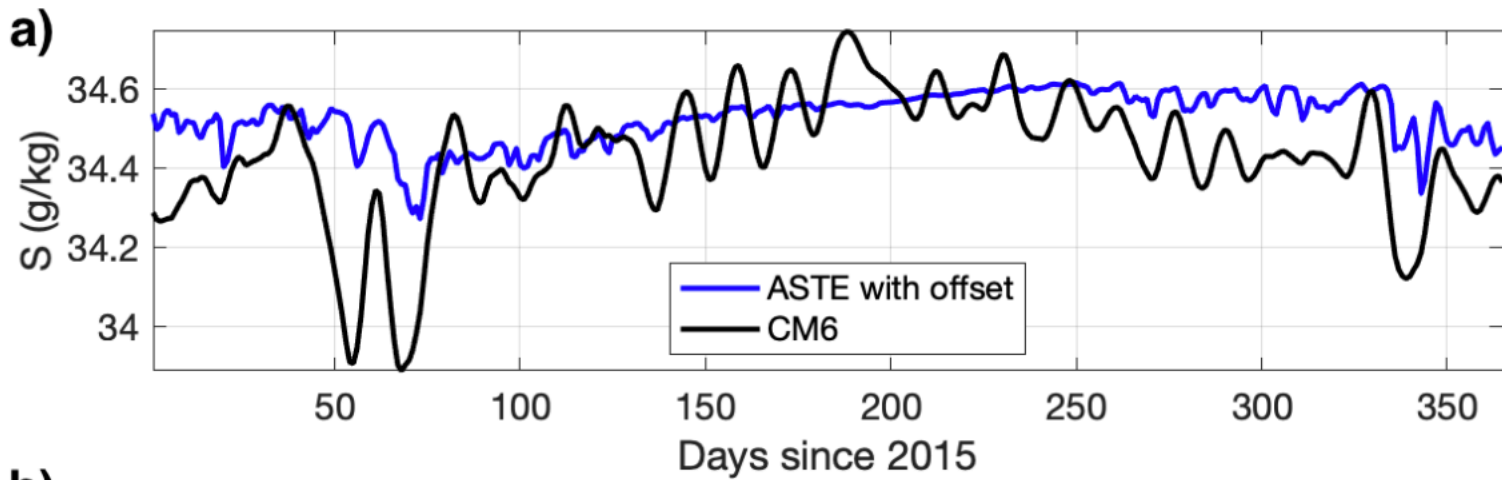


Figure 3.

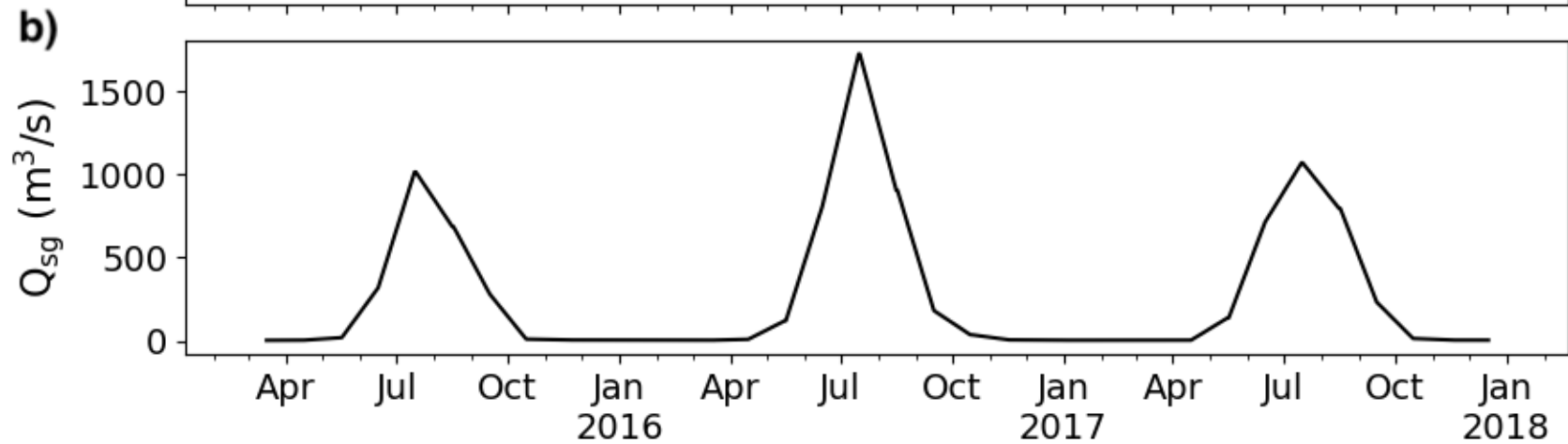
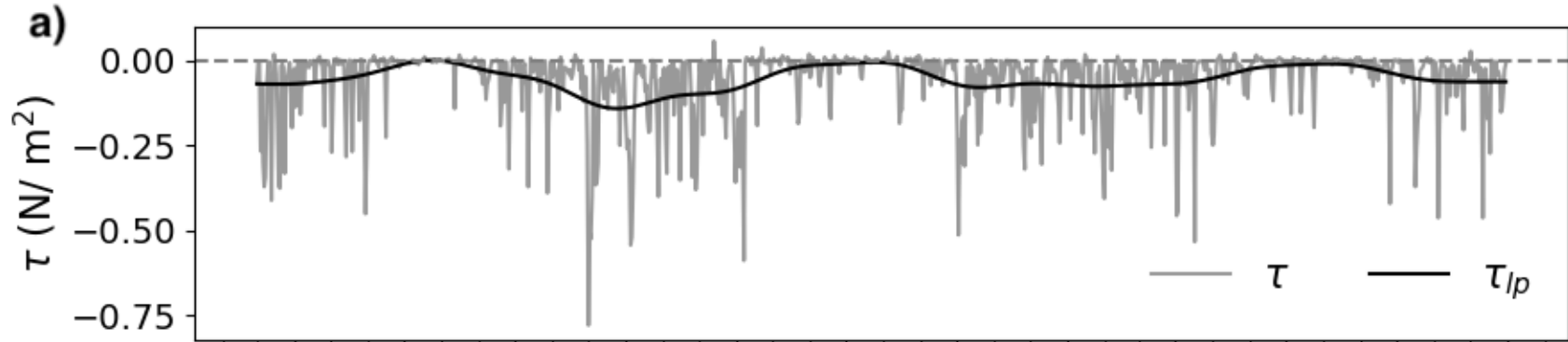


Figure 4.

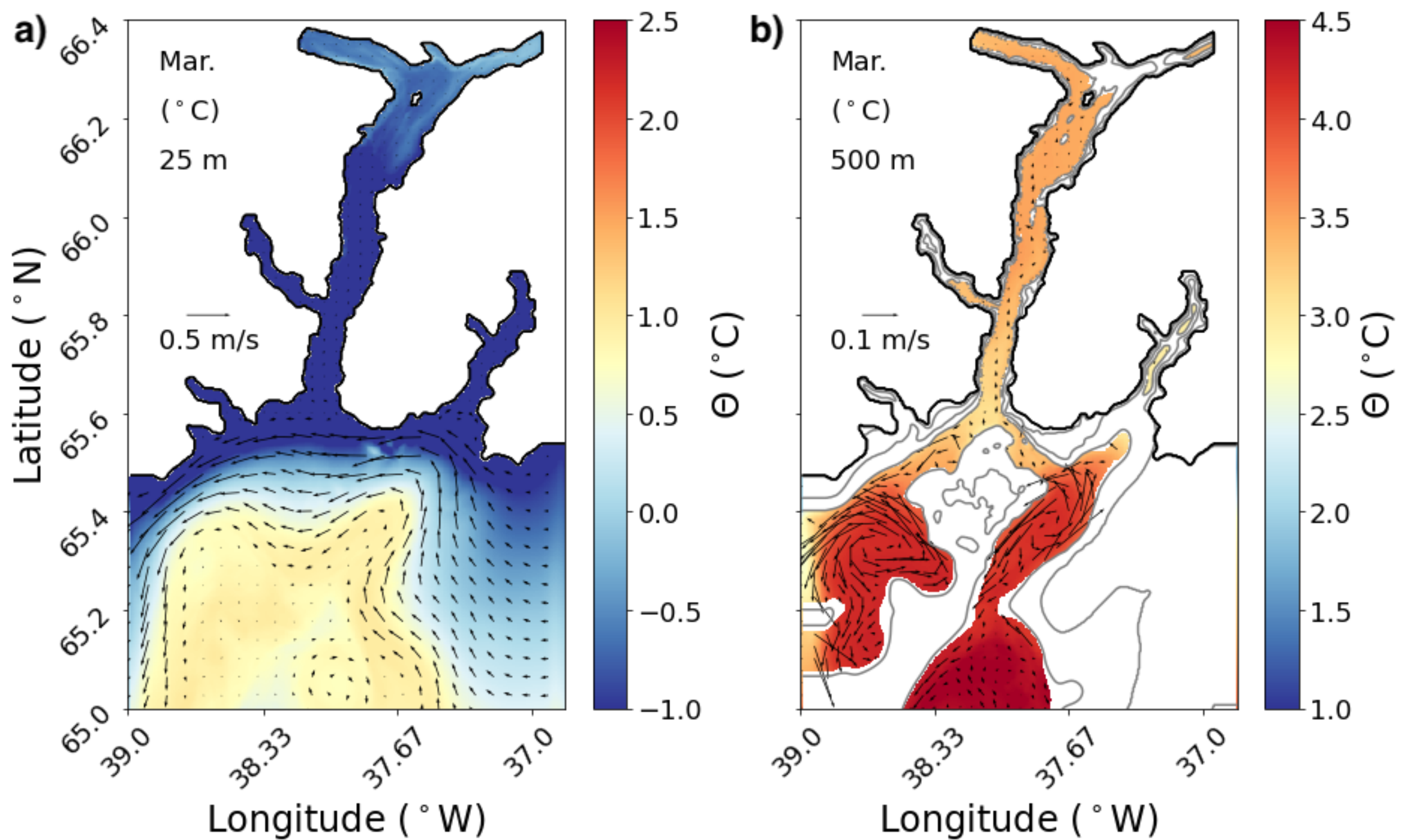


Figure 5.

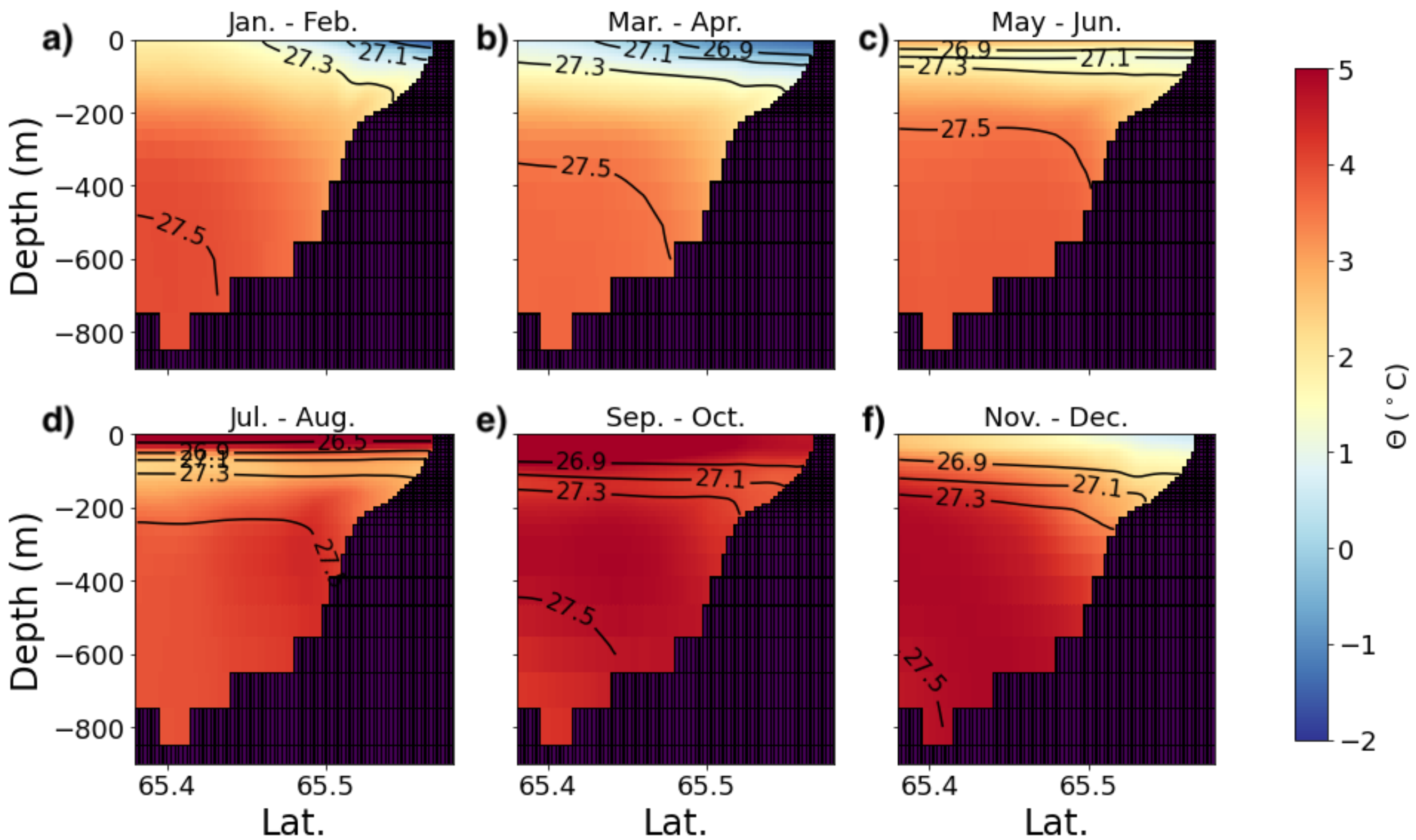


Figure 6.

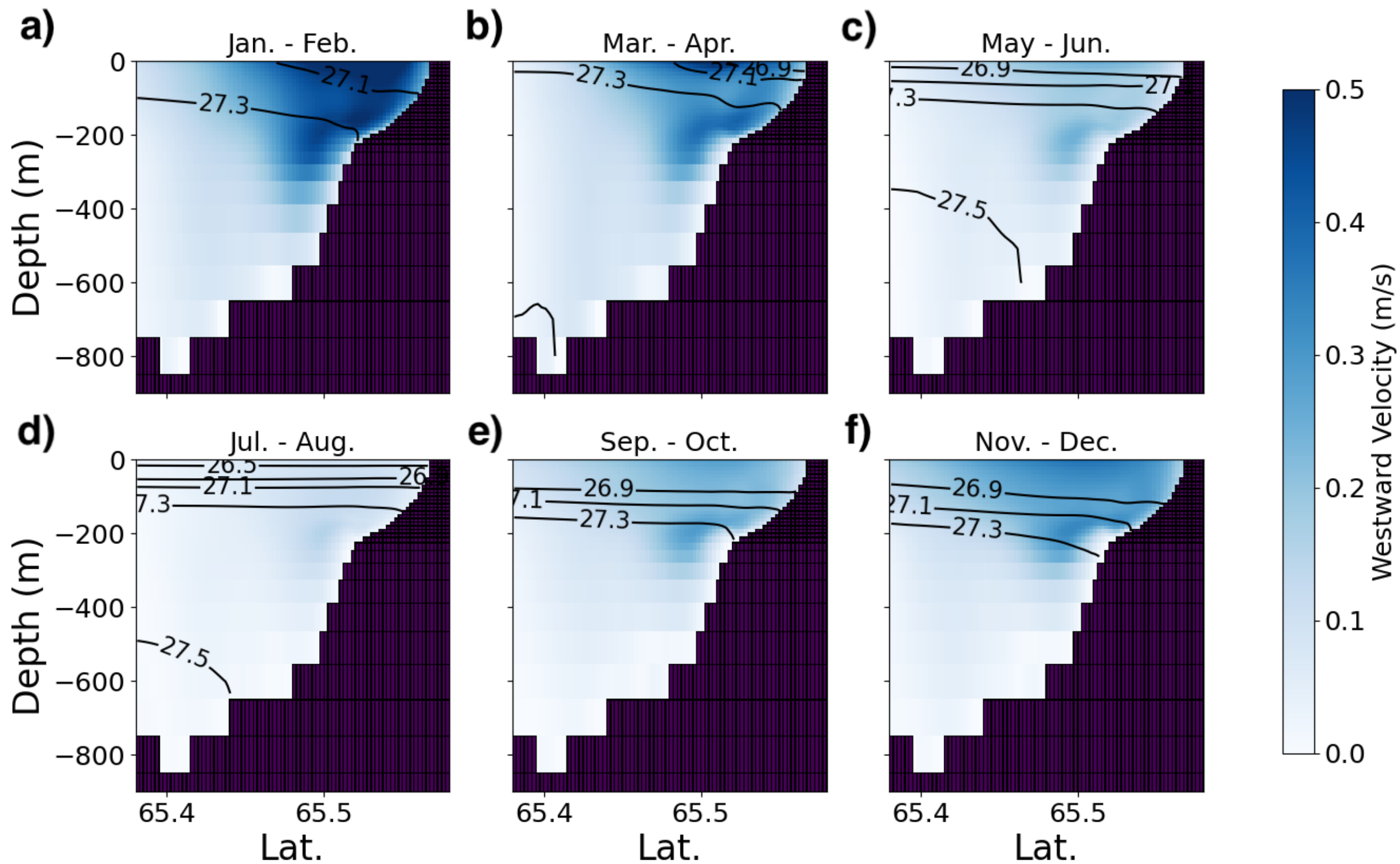


Figure 7.

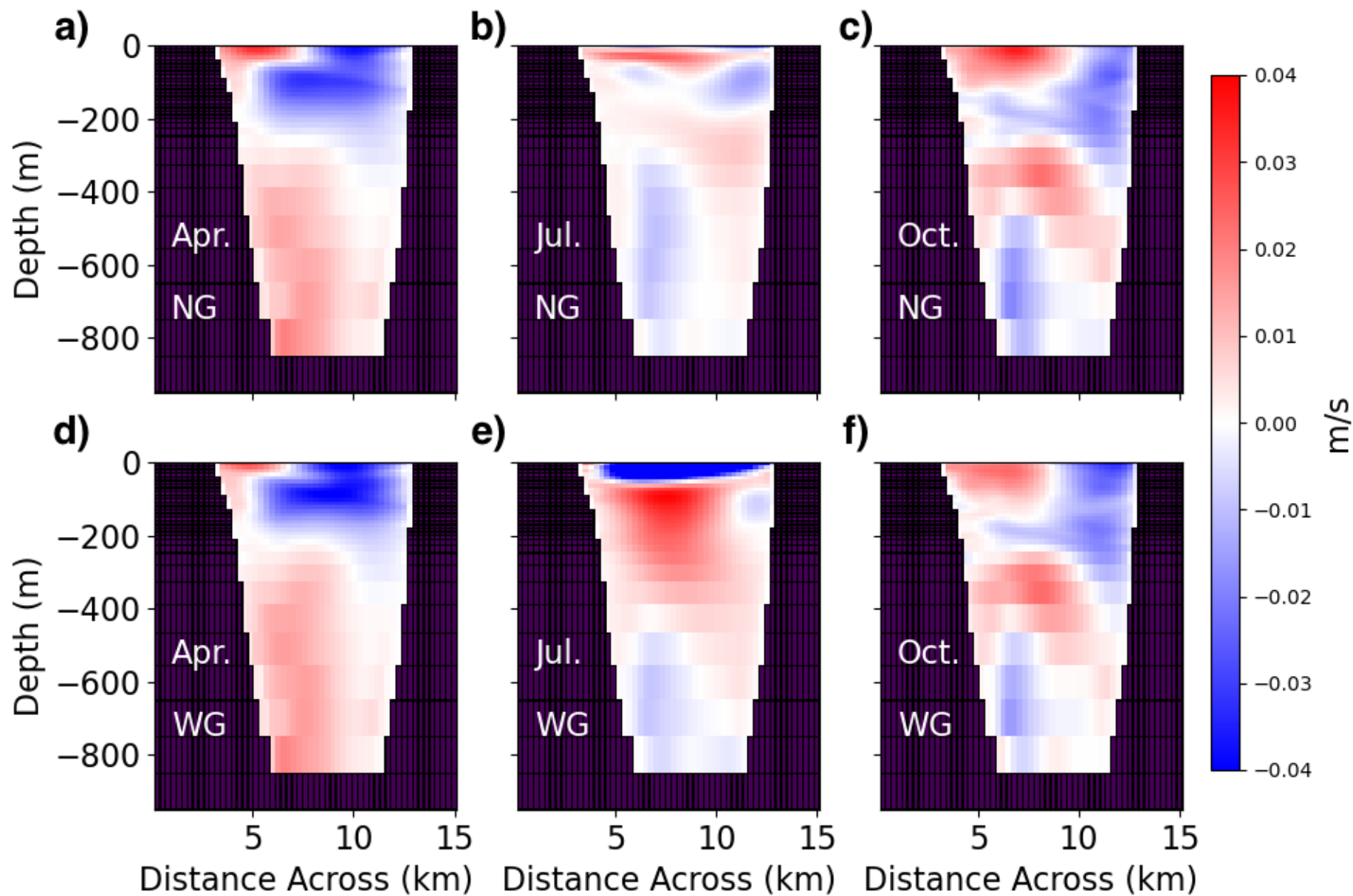


Figure 8.

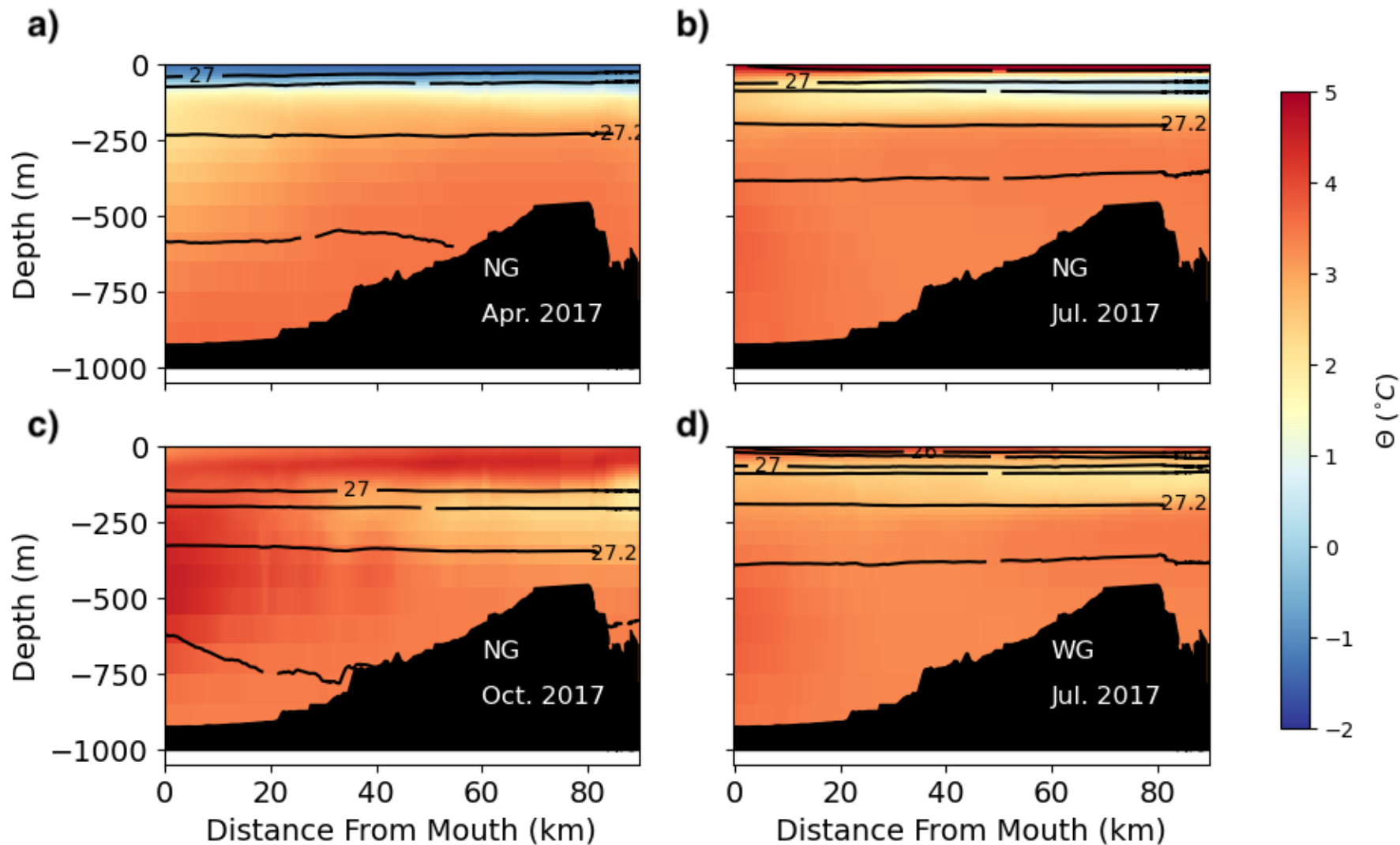


Figure 9.

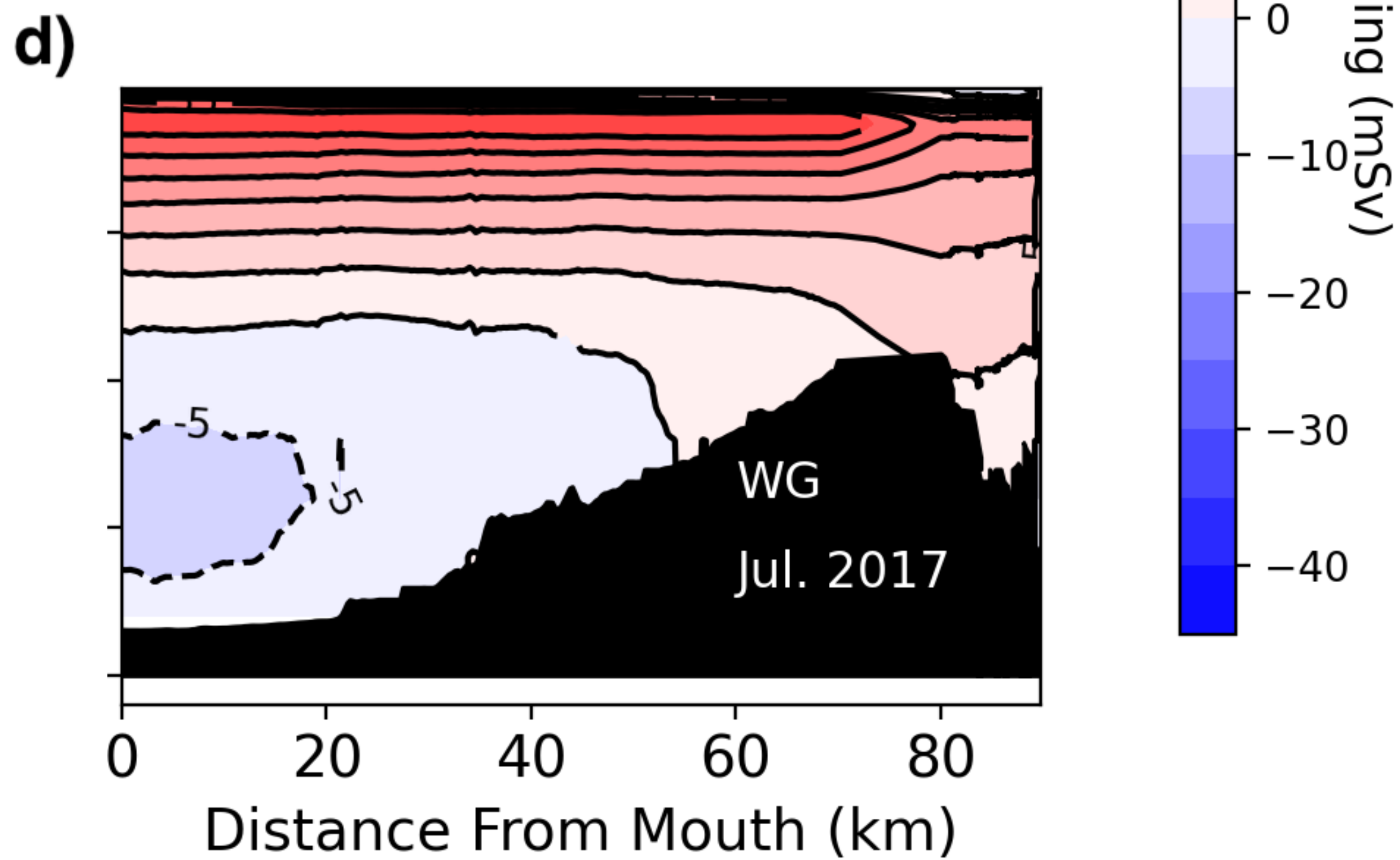
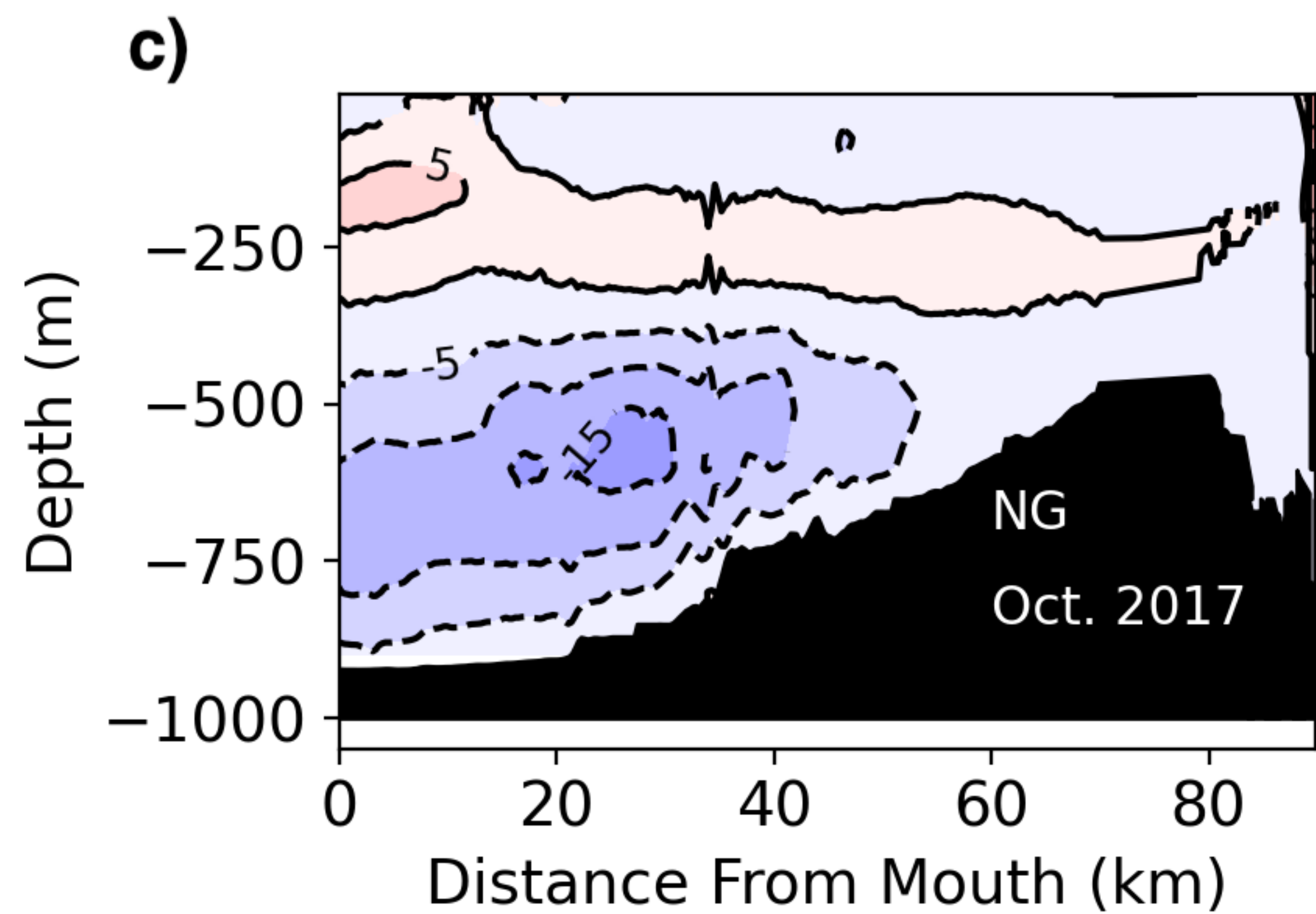
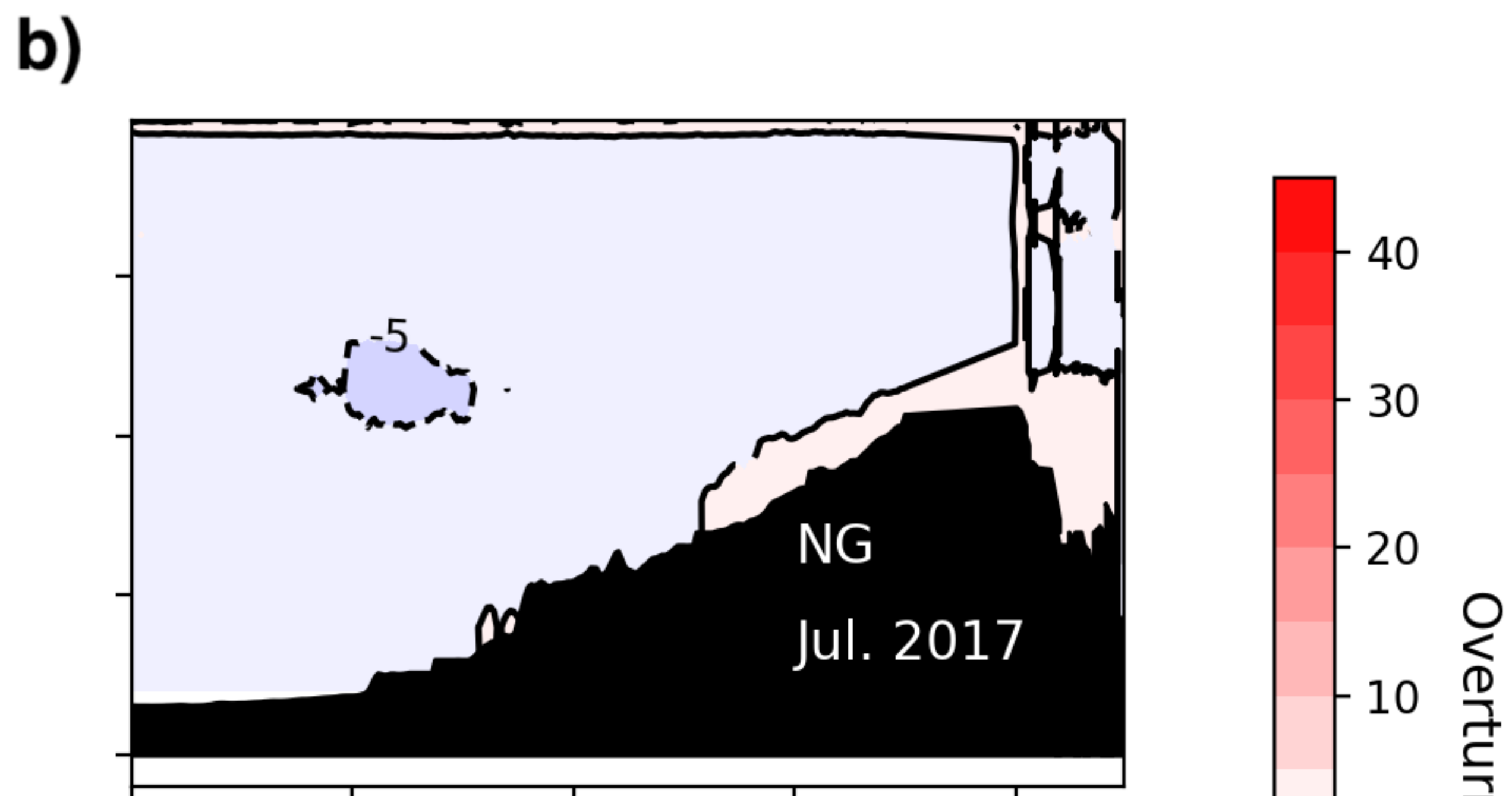
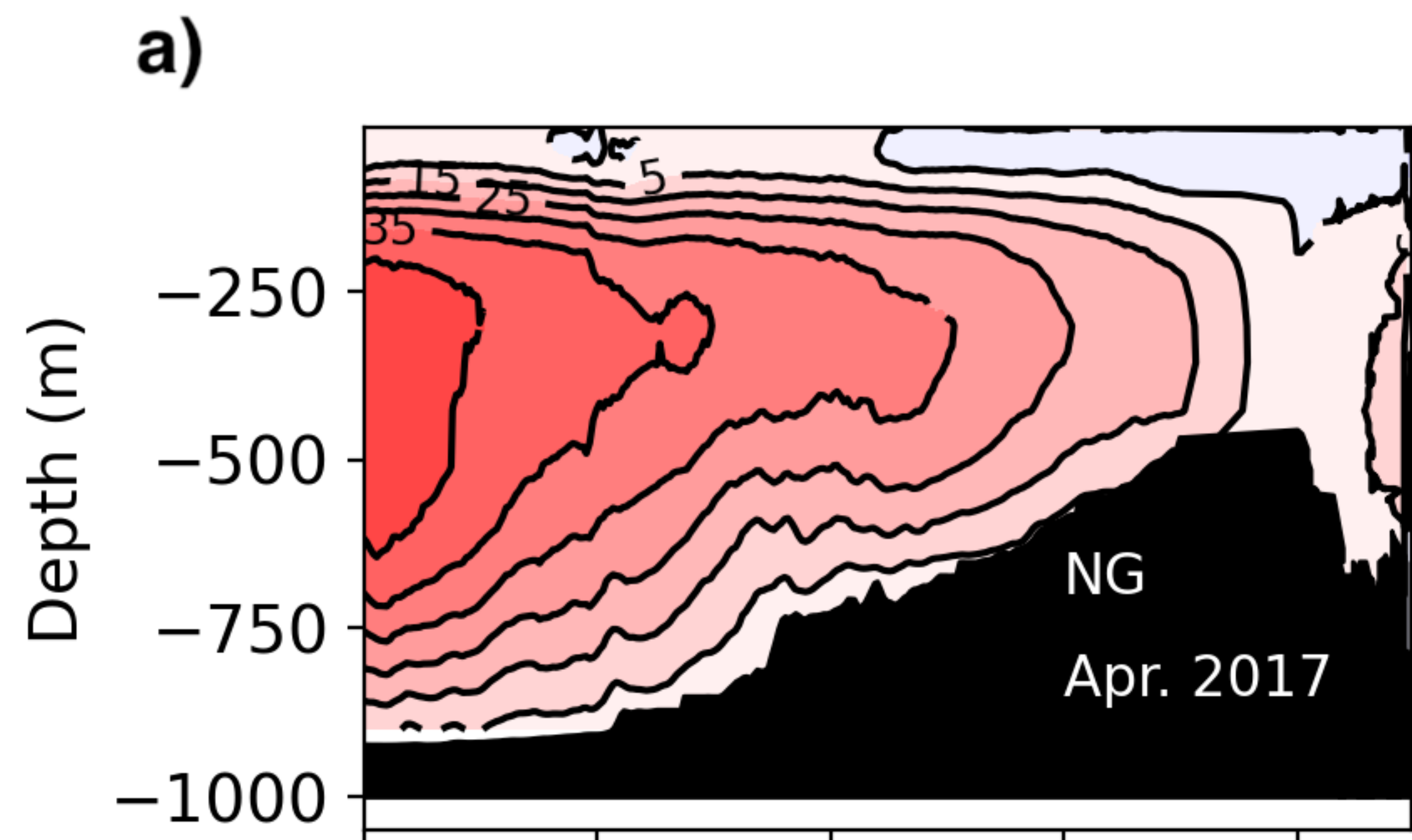


Figure 10.

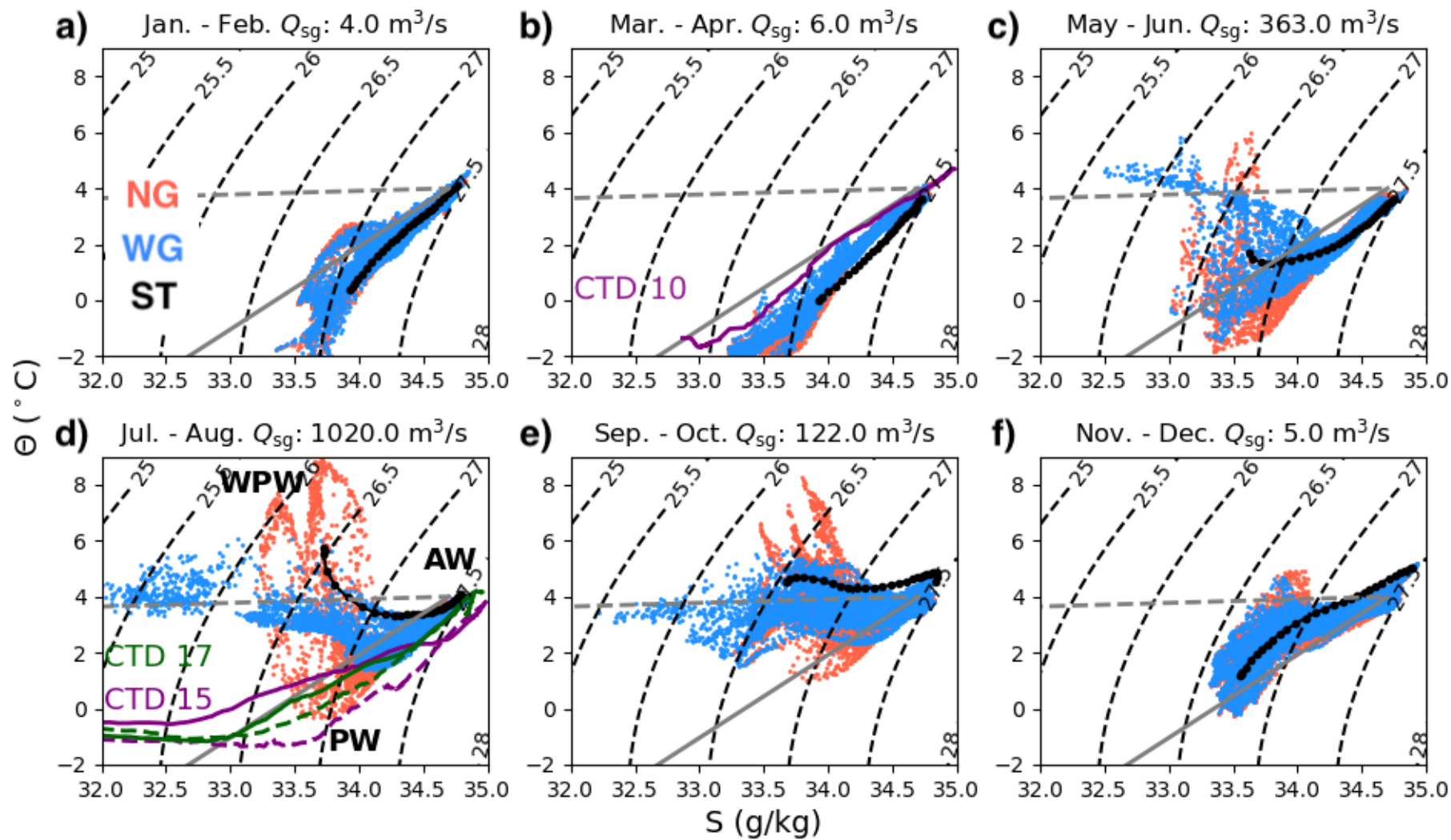


Figure 11.

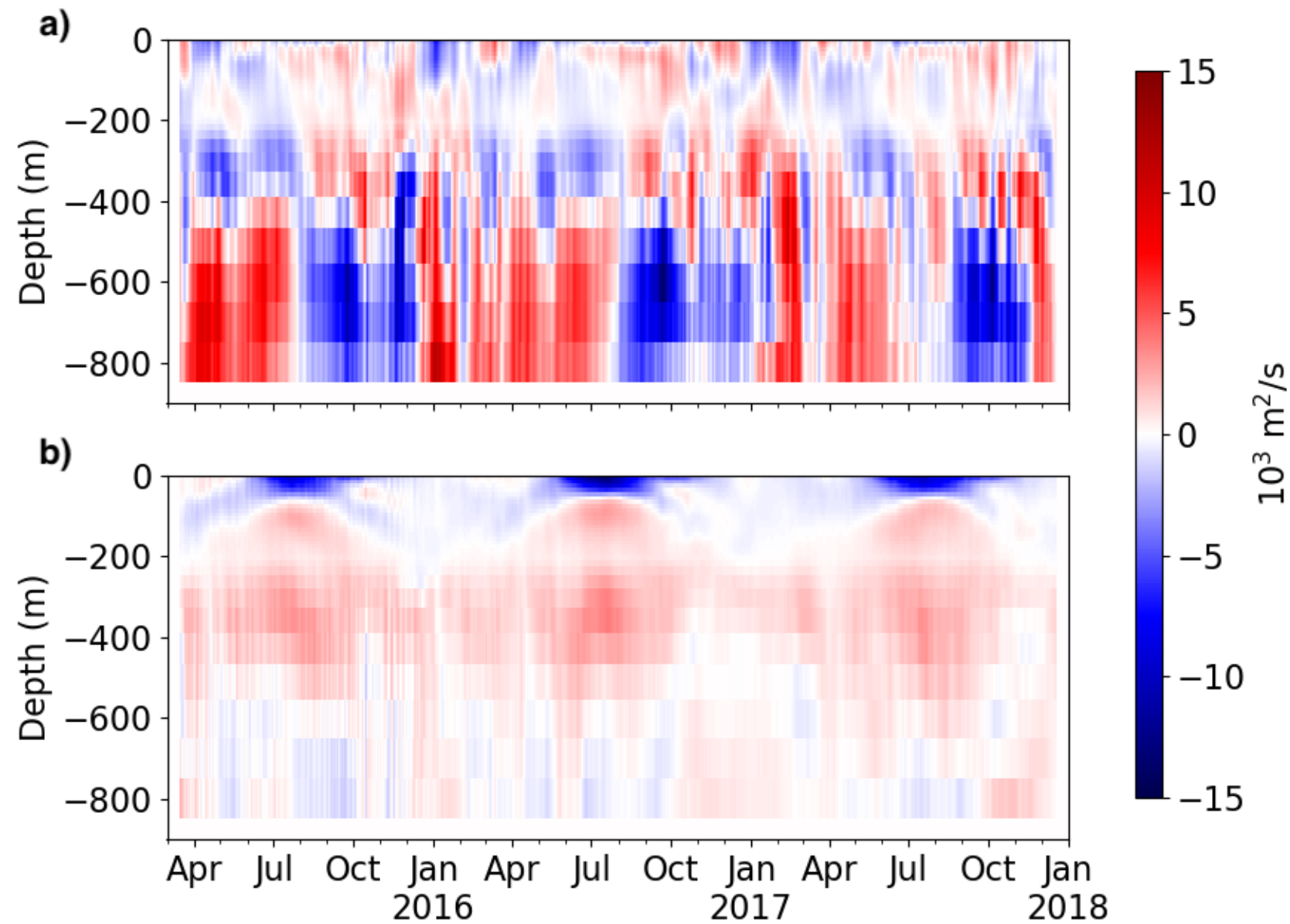


Figure 12.

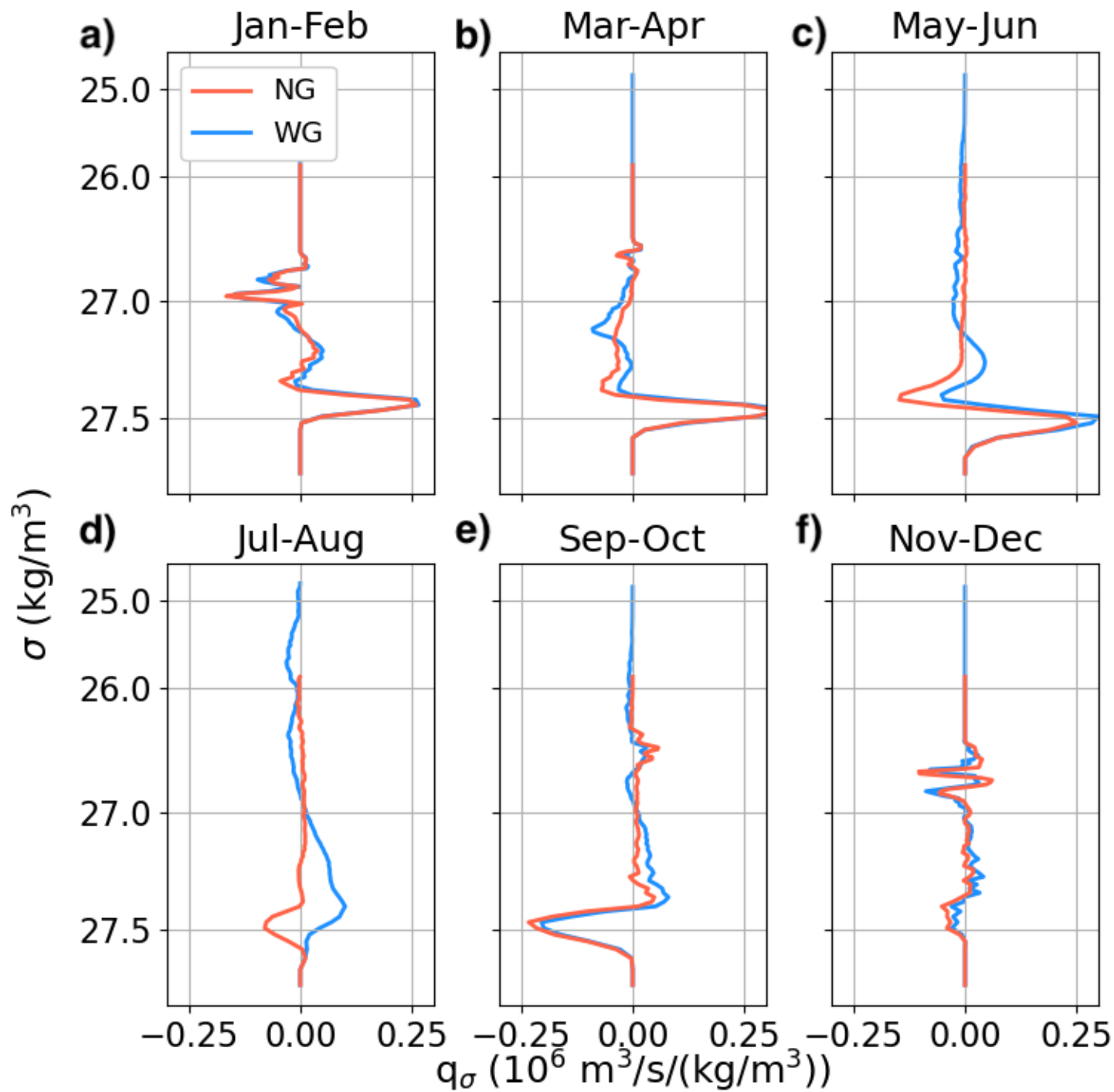


Figure 13.

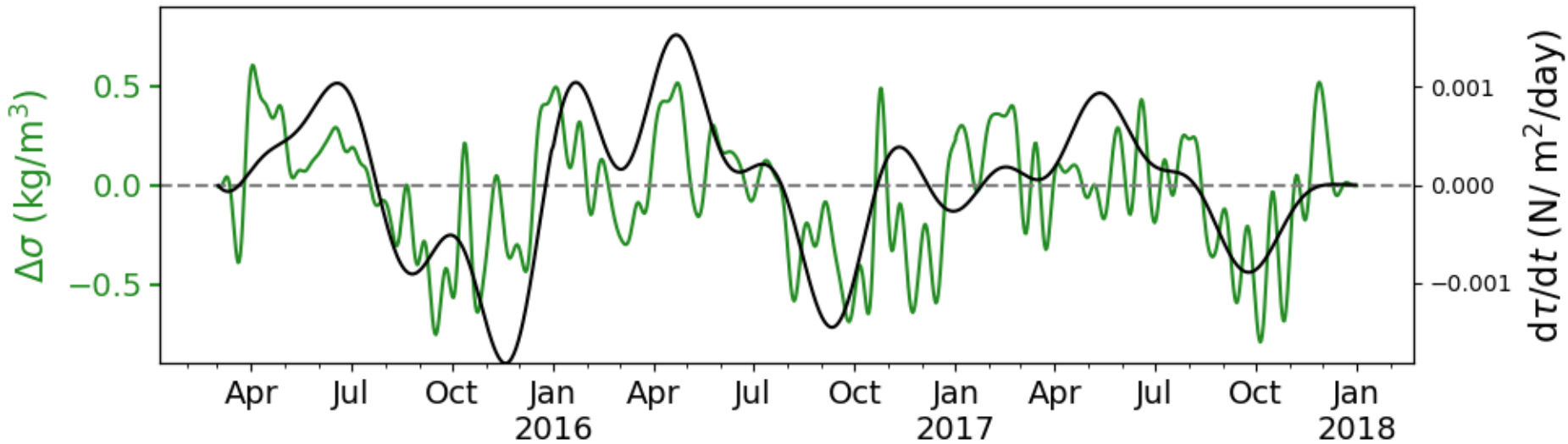


Figure 14.

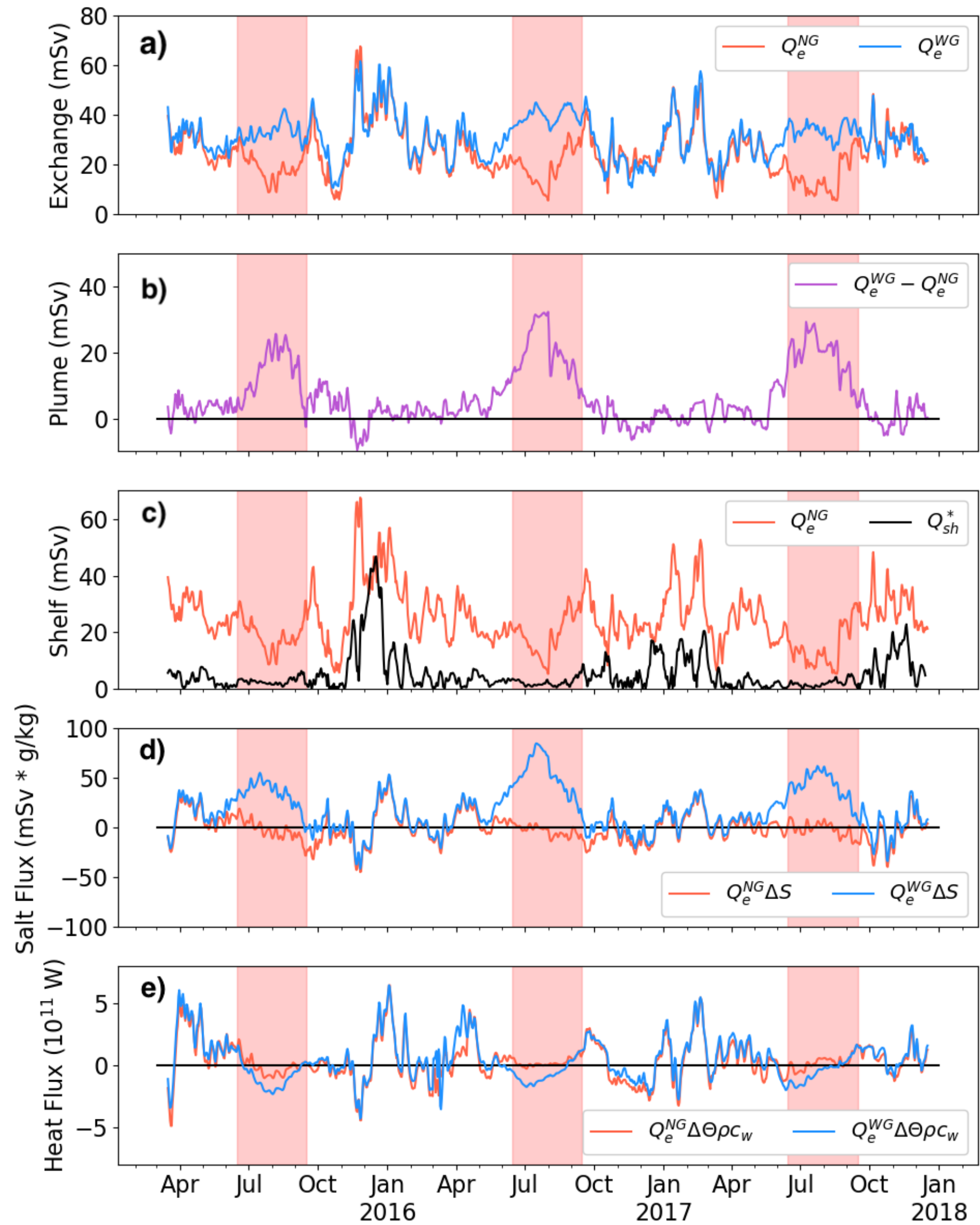
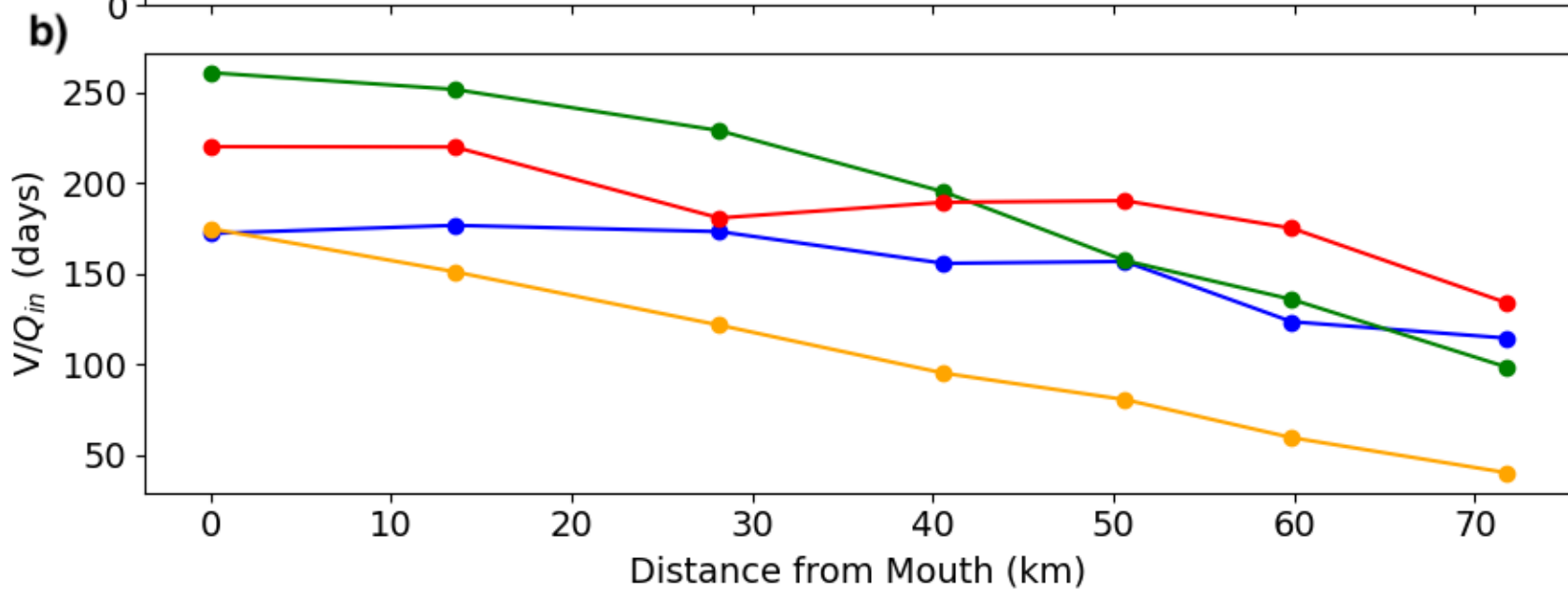
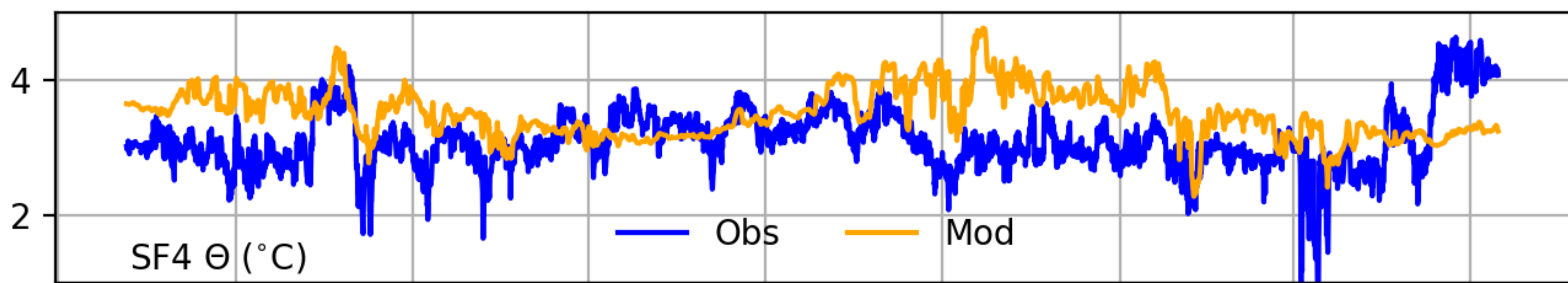
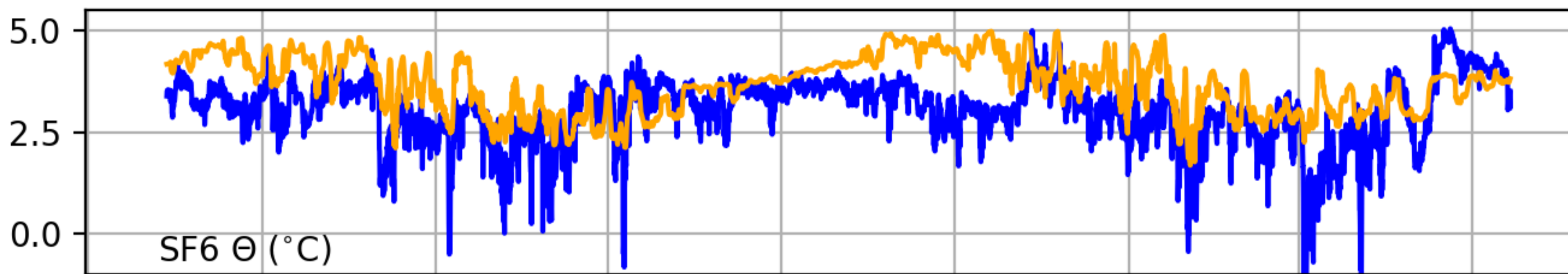
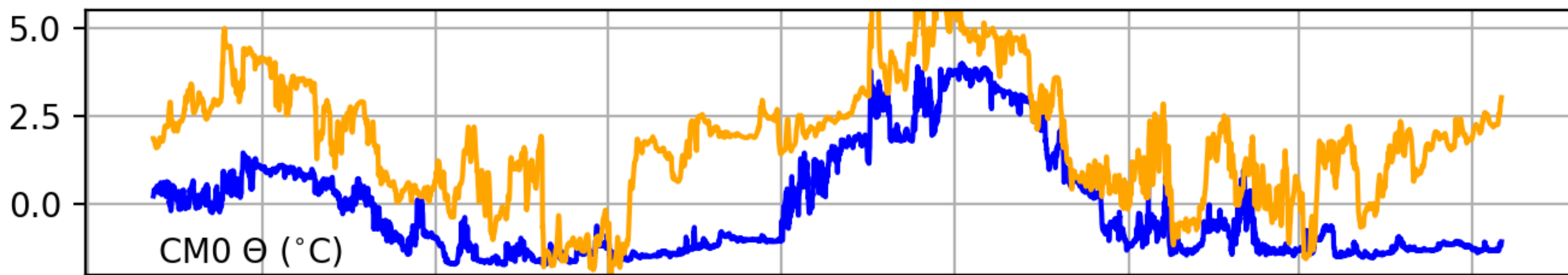
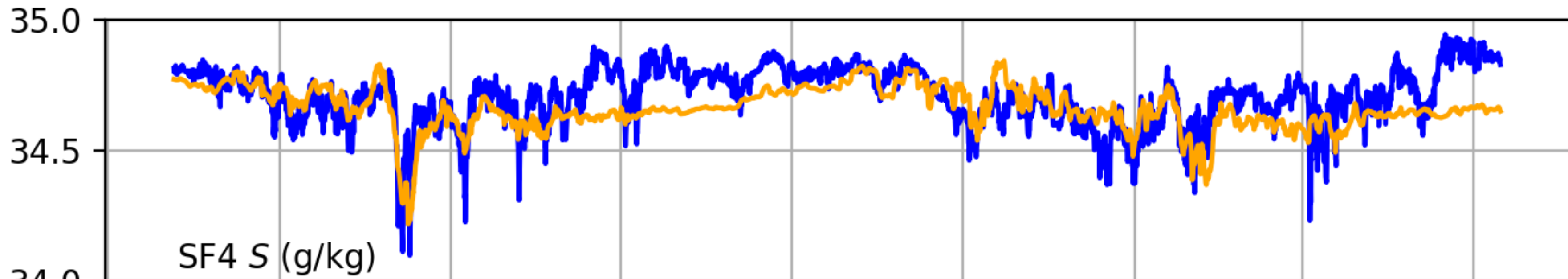
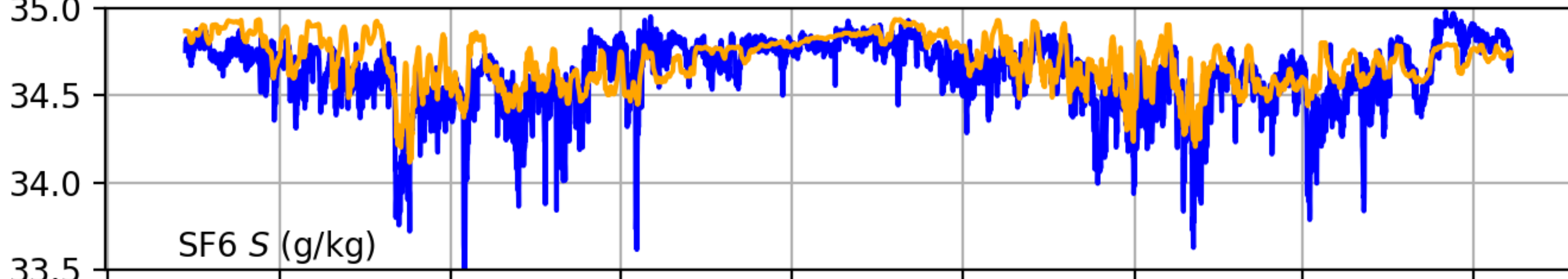
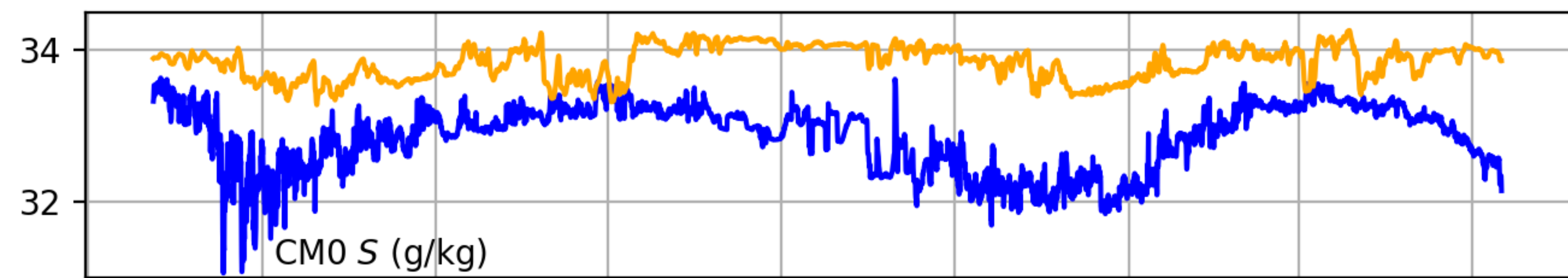


Figure 15.



Appendix Figure 1.

a)**b)****c)****d)****e)****f)**

2015-07 2015-10 2016-01 2016-04 2016-07 2016-10 2017-01 2017-04 2017-07